UNIVERSITÀ DI PARMA

UNIVERSITA' DEGLI STUDI DI PARMA

DOTTORATO DI RICERCA IN FISICA

CICLO XXXIV

Gallium oxide thin films: electrical properties and application to UV-C radiation detection

Coordinatore:
Chiar.mo Prof. **Stefano Carretta**

Tutore:
Chiar.mo Prof. **Roberto Fornari**

Dottorando: **Carmine Borelli**

Anni Accademici 2018/19 – 2020/21

Contents

Most used acronyms

AFM	Atomic Force Microscopy
BFOM	Baliga Figure of Merit
CB	Conduction Band
CVD	Chemical Vapour Deposition
DFT	Density Functional Theory
EQE	External Quantum Efficiency
FET	Field-Effect Transistor
FL	Fermi Level
IQE	Internal Quantum Efficiency
MBE	Molecular-Beam-Epitaxy
MOCVD	Metalorganic Chemical Vapour Deposition
MOSFET	Metal-Oxide Semiconductor Field-Effect Transistor
MOVPE	Metalorganic Vapour Phase Epitaxy
MSM	Metal-Semiconductor-Metal
RBS	Rutherford Back-Scattering
sccm	Standard Cubic Centimetres per Minute
TEM	Transmission Electron Microscopy
TLM	Transfer Length Method
ToF-SIMS	Time of Flight-Secondary Ion Mass Spectroscopy

UV	Ultraviolet
VB	Valence Band
vdP	van der Pauw
VIS	Visible
VPE	Vapour Phase Epitaxy
XPS	X-Ray Photoelectron Spectroscopy
XRD	X-Ray Diffraction
WBG	Wide Bandgap Semiconductor

Introduction

Wide-bandgap semiconductors (WBGs) like SiC, GaN, Ga_2O_3 attract a great interest in the research community for their applications in different fields. Among them, gallium oxide (Ga_2O_3) is characterized by an exceptionally wide bandgap (E_g = 4.5 - 4.9 eV) [1, 2, 3, 4] and high breakdown electric field (E_{br} ~ 8 MV/cm) [5]. These peculiar properties combined with the possibility to modulate its conductivity by extrinsic doping [6, 7], and the availability of high-quality single crystals [2], as well as epilayers [8], make it a well-suited material for several applications in high-power electronics [9] and solar-blind UV-C photodetectors [3, 10]. Ga_2O_3 is known to have five polymorphs, labelled α, β, γ, δ and ε [11]. The monoclinic β-phase is the most thermodynamically stable structure under atmospheric pressure and so far, the most investigated one. Nonetheless, since β-Ga_2O_3 has a monoclinic structure *(i)* it presents anisotropic physical properties and *(ii)* the single crystals are prone to cleavage, which poses non-trivial problems at the time of device manufacturing. Moreover, its low degree of crystallographic symmetry usually results in the formation of large amount of structural defects in heteroepitaxial growths on sapphire substrates which can eventually degrade its performances. For these reasons, there is an increasing interest about other Ga_2O_3 polymorphs, for instance the so-called epsilon-phase, that presents an orthorhombic crystallographic structure of higher symmetry than the β –phase [12].

ε-Ga_2O_3 (i) shares a similarly high bandgap with β-Ga_2O_3, (ii) can be stabilized on cost effective sapphire substrates with different epitaxial growth techniques [13], and (iii) exhibits a significant spectral selectivity in the UV-C spectral region that make it a promising material for UV solar-blind photodetector fabrication [14].

As mentioned above, the ε-polymorph is less investigated than the most investigated β-phase. In particular, the development of efficient electric contacts on ε-phase as well as a doping control in a wide range are little explored. For different applications, a good control on charge carrier concentration and optimization of electrical contacts are fundamental requirements.

For these reasons, this PhD research project has given priority to the following aspects of the ε-polymorph:

- Fabrication of ohmic contacts on ε-Ga_2O_3 thin films.
- Improvement of doping process (via Sn thermal diffusion) of ε-Ga_2O_3 layers.
- Development of UV-C solar-blind photodetectors based on ε-Ga_2O_3.

The epitaxial growth of ε-Ga_2O_3 layers was carried out at IMEM-CNR Institute, while the electrical characterization and doping process were performed within the Semiconductors research team of the Department of Mathematical, Physical and Computer Sciences of Parma University.

The PhD research activity included also a four-month period abroad as a guest PhD student at the Paul Drude Institute of Berlin (PDI). The core of the activity at PDI was focused on the investigation of Ar-plasma treatments on ε-Ga_2O_3 epilayers.

The dissertation is divided into five chapters. In Chapter 1 an overview of the Ga_2O_3 properties will be given and the choice of ε-polymorph motivated. The investigation of crystal and electronic structures of ε- Ga_2O_3 together with the optical properties are reported. Finally, a survey of Ga_2O_3 applications will be discussed, from power devices to UV optoelectronics.

In Chapter 2 the experimental techniques employed during the PhD research activity will be presented. The basic operation principles of the MOCVD growth process used to produce ε-Ga_2O_3 epilayers will be reported. An overview of the sputtering deposition technique used for doping the material as well as to make reliable electrical contacts on ε-Ga_2O_3 will be described. Finally, the characterization methods used to investigate ε-Ga_2O_3 samples will be presented.

The Chapter 3 focuses on the electrical properties of ε-Ga_2O_3 layers. The first part concerns the description of n-type doping process by Sn thermal diffusion for ε-Ga_2O_3 layers. In the second part the realization of reliable Ohmic contacts on ε-Ga_2O_3 thin films and relevant conduction mechanisms are reported. Good Ohmic contacts were obtained by deposition of SnO_x/ITO structure on top of undoped and Sn-doped ε-Ga_2O_3 thin films.

It is well known that the metal/semiconductor junction is a fundamental part of any electronic device, and its physical properties have a strong impact on the performance of the device. Consequently, a fundamental understanding of how ohmic contacts works is a major step towards electronic and power devices.

The Chapter 4 is devoted on the description of UV-C solar blind photodetectors based on ε-Ga_2O_3, which represent the main achievement of the second part of my PhD research work. Remarkable results such as the rejection ratio (R_{UV-VIS}) greater than 10^4 and the ON-OFF switching times of less than one second makes the epsilon phase of gallium oxide an effective material for UV-C detection.

High values of photo-gain were observed, which are ascribed to the excess of collected majority carriers (electrons) Δn, with respect to the minority carriers Δp, possibly related to hole trapping/self-trapping processes.

Chapter 5 deals with the investigation of Ar-plasma treatments on nominally undoped ε-Ga_2O_3 epilayers. A plasma treatment can induce – depending on the material and the treated surface – physical and/or chemical changes which could in turn result in a detectable variation of the layer conductivity.

For this reason, ε-Ga_2O_3 layers have been electrically investigated before and after the plasma exposures. It has been found that the Ar-plasma treatment induces a remarkable change in the conductivity of the layers. The probable physical mechanism behind this type of conduction could be related to a partial amorphization of the Ga_2O_3 layer in the vicinity of the surface. However, the full explanation of the physical mechanism induced by the plasma treatment requires further experimental investigations such as T-dependent electrical measurements, X-Ray Photoelectron Spectroscopy (XPS), and transmission electron microscopy (TEM), already planned and to be performed in the frame of internal and external collaborations.

References

[1] M. Orita, H. Ohta, M. Hirano and H. Hosono, “Deep-ultraviolet transparent conductive ß-Ga2O3 thin films,” *Appl. Phys. Lett.* , vol. 77, p. 4166–4168 , 2000.

[2] Z. Galazka, R. Uecker, K. Irmscher, M. Albrecht, D. Klimm, M. Pietsch, M. Brützam, R. Bertram, S. Ganschow e R. Fornari, « Czochralski growth and characterization of β-Ga2O3 single crystals,» *Crystal Research and Technology,* vol. 45, n. 12, pp. 1229-1236, 2010.

[3] M. Pavesi, F. Fabbri, F. Boschi, G. Piacentini, A. Baraldi, M. Bosi, E. Gombia, A. Parisini and R. Fornari, “ ε-Ga2O3 epilayers as a material for solar-blind UV photodetectors,” *Materials Chemistry and Physics,* vol. 205, pp. 502-507, 2018.

[4] Y. Oshima, E. G. Víllora, Y. Matsushita, S. Yamamoto e K. Shimamura, «Epitaxial growth of phase-pure ε-Ga2O3 by halide vapor phase epitaxy,» *Journal of Applied Physics* , vol. 118, p. 085301, 2016.

[5] M. Higashiwaki, K. Sasaki, A. Kuramata, T. Masui and S. Yamakoshi, “Development of gallium oxide power devices,” *Phys. Status Solidi Appl. Mater.*, vol. 211, p. 21–26, 2014.

[6] E. G. Víllora, K. Shimamura, Y. Yoshikawa, T. Ujiie and K. & Aoki, “Electrical conductivity and carrier concentration control in β-Ga2O3 by Si doping,” *Applied Physics Letters,* vol. 92, no. 20, p. 202120, 2008.

[7] K. Irmscher, Z. Galazka, M. Pietsch, R. Uecker e R. Fornari, «Electrical properties of β-Ga2O3 single crystals grown by the Czochralski method,» *Journal of Applied Physics,* vol. 110, n. 6, p. 063720, 2011.

[8] K. Kaneko, H. Ito, S. D. Lee and S. Fujita, “Oriented growth of beta gallium oxide thin films on yttrium-stabilized zirconia substrates,” *physica status solidi (c),* vol. 10, no. 11, pp. 1596-1599, 2013.

[9] J. L. Hudgins, G. S. Simin, E. Santi and M. A. Khan, “An assessment of wide bandgap semiconductors for power devices,” *IEEE Transactions on Power Electronics,* vol. 18, no. 3, pp. 907-914, 2003.

[10] D. Guo, Z. Wu, P. Li, Y. An, H. Liu, X. Guo, H. .Yan, G. Wang, G. Sun, L. Li e W. Tang, « Fabrication of β-Ga2O3 thin films and solar-blind photodetectors by laser MBE technology,» *Optical Materials Express,* vol. 4, n. 5, pp. 1067-1076, 2014.

[11] S. J. Pearton, J. Yang, P. H. Cary IV, F. Ren, J. Kim, M. J. Tadjer and M. A. Mastro, “A review of Ga2O3 materials, processing, and devices,” *Applied Physics Reviews,* vol. 5, no. 1, p. 011301, 2018.

[12] I. Cora, F. Mezzadri, F. Boschi, M. Bosi, M. Čaplovičová, G. Calestani and R. Fornari, “The real structure of ε-Ga 2 O 3 and its relation to κ-phase,” *CrystEngComm,* vol. 19, no. 11, pp. 1509-1516, 2017.

[13] M. Bosi, P. Mazzolini, L. Seravalli and R. Fornari, “Ga2O3 polymorphs: tailoring the epitaxial growth conditions,” *Journal of Materials Chemistry C,* vol. 8, no. 32, pp. 10975-10992, 2020.

[14] Y. Qin, L. Li, X. Zhao, G. S. Tompa, H. Dong, G. Jian and M. Liu, “Metal–semiconductor–metal ε-Ga2O3 solar-blind Photodetectors with a record-high responsivity rejection ratio and their gain mechanism,” *ACS Photonics,* vol. 7, no. 3, pp. 812-820, 2020.

Chapter 1 – Introduction to Ga_2O_3

In this chapter, an overview of the gallium oxide (Ga_2O_3) properties will be presented, with a particular focus on the ε-polymorph. The investigation of crystal and electronic structures of the ε-Ga_2O_3 together with the optical properties will be reported. Finally, a survey of Ga_2O_3 applications from high-power devices to UV optoelectronics will be provided.

1.1 Introduction

Gallium oxide (Ga_2O_3) is a binary ionic compound, belonging to family of sesquioxides, consisting of three oxygen anions with two gallium cations. Among the semiconductor oxides, Ga_2O_3 has attract much attention thanks to the excellent properties this material presents such as wide bandgap, high breakdown field and good optical transparency. These peculiar properties, combined with the possibility to modulate its conductivity by extrinsic doping, and the availability of good-quality epitaxial layers, make it a well-suited material for several applications in high-power electronics and solar-blind UV photodetectors.

Considering power electronic applications, the bandgap energy (E_g) and the breakdown electric field (E_{br}), have to be large. These outstanding material properties (see Tab.1.1 and Fig.1.1) enable Ga_2O_3 power devices with higher breakdown voltage (V_{br}) and higher switching efficiencies. This is a main advantage of Ga_2O_3 compared to traditional semiconductors such as Si.

An additional advantage for mass production of Ga_2O_3 over SiC and GaN is the bulk material growth technique: while SiC and GaN single crystals are mostly produced by sublimation or solution growth techniques, Ga_2O_3 single crystals can be grown by cost-effective melting methods, which lower the wafer production costs. On the other hand, a clear disadvantage for Ga_2O_3, is its poor thermal conductivity who creates self-heating effects that must be mitigated in order to utilize Ga_2O_3 in high-power electronic devices.

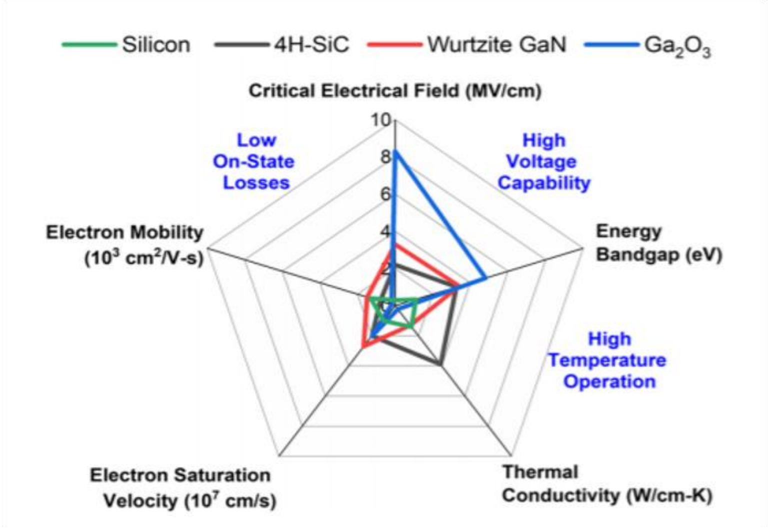

Fig.1.1 Relevant physical and electronic parameters for Si, 4H-SiC, Wurtzite GaN and Ga2O3 [1].

Tab.1.1 Material properties of Si, GaN, SiC and β-Ga_2O_3 [2].

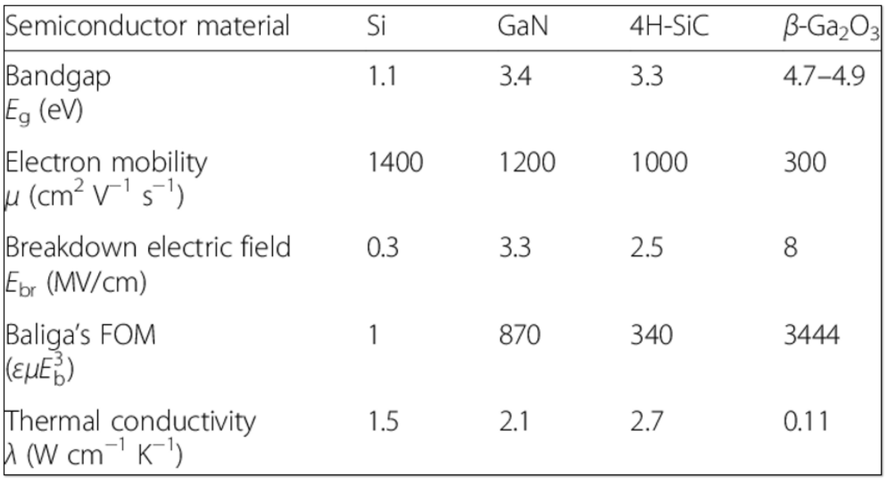

Semiconductor material	Si	GaN	4H-SiC	β-Ga_2O_3
Bandgap E_g (eV)	1.1	3.4	3.3	4.7–4.9
Electron mobility μ (cm^2 V^{-1} s^{-1})	1400	1200	1000	300
Breakdown electric field E_{br} (MV/cm)	0.3	3.3	2.5	8
Baliga's FOM ($\varepsilon \mu E_b^3$)	1	870	340	3444
Thermal conductivity λ (W cm^{-1} K^{-1})	1.5	2.1	2.7	0.11

The history of Ga_2O_3 dates back to the 1900_s, when the gallium element and its compounds were discovered [3]. In 1952 [4], for the first time, different crystal structures of Ga_2O_3 were reported, and in 1965 [5] the energy gap of β-Ga_2O_3 has been obtained by optical measurements of bulk crystals. During the years, despite Ga_2O_3 is intensively studied, it was not possible for this material to compete with SiC and GaN semiconductors due to the poor progress in device technology.

However, over time, the improvement of crystal growth techniques allowed to obtain both bulk [6] and epitaxial layers [7] of Ga_2O_3 of higher quality. A good control on doping concentration [8] together with the fabrication of reliable electrical contacts [9] paved the way to a wider range of applications such as UV photodetectors [10] and power devices [11]. In 2012 the realization of the first field-effect transistors (FETs) based on Ga_2O_3 [12] marked the turning point to encourage Ga_2O_3 research and technology. In the last 10 years, the number of publications on Ga_2O_3 significantly increased, as it is clearly visible in Fig.1.2.

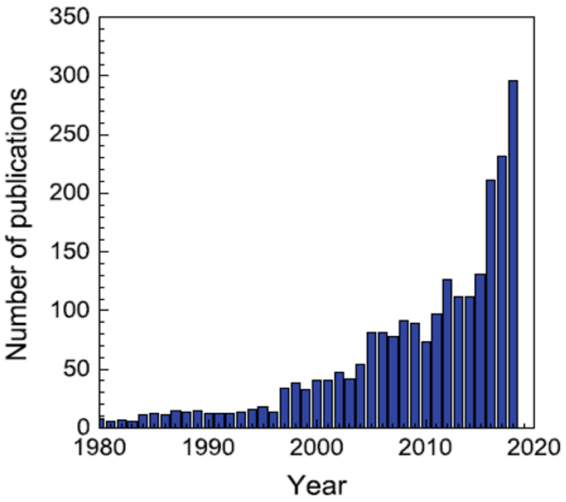

Fig.1.2 Number of publications on Ga_2O_3 since 1975.
(Reproduced from Web of Science - July 4, 2019).

Currently, five polymorphs labelled α, β, γ, δ and ε have been confirmed for gallium oxide [13]. The crystal structures of Ga_2O_3 are differentiated by the stacking sequence of the Ga atoms in octahedral and tetrahedral sites between close-packing array of oxygen layers (Fig.1.3). Owing to the differing array of gallium and oxygen atoms, each Ga_2O_3 polymorphs exhibits different lattice and optical parameters, as shown in Tab.1.2.

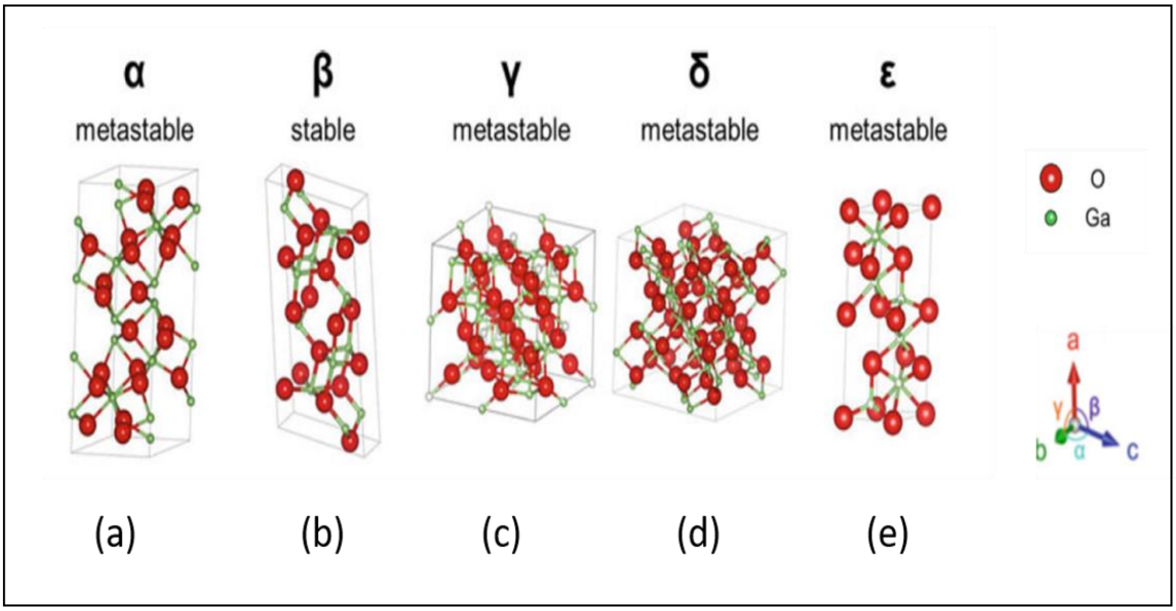

Fig.1.3 Crystal structure of different gallium oxide polymorphs. (a) α-phase rhombohedral structure, (b) β-phase monoclinic structure, (c) γ-phase cubic/spinel structure, (d) δ-phase cubic/ bixbyite structure, (e) ε-phase orthorhombic structure [13].

Tab.1.2 Unit cell parameters and optical constants of Ga_2O_3 polymorphs.

Phase	**Symmetry**	**Space group**	**Lattice constants (Å)**	**Refractive index, n**	**Optical dielectric constant**	**Ref.**
α	rhombohedral	$R\bar{3}c$	a, b = 4.98 - 5.04 c = 13.4 - 13.6	1.74 – 1.95	3.03 – 3.80	[14, 15]
β	monoclinic	$C2/m$	a = 12.12 - 12.34 b = 3.03 - 3.04 c = 5.80 - 5.87	1.68 – 1.89	2.82 – 3.57	[14, 15]
γ	cubic (spinel)	$Fd\bar{3}m$	a = 8.24 - 8.30			[14]
δ	cubic (bixbyite)	$Ia\bar{3}$	a = 9.4 - 10.0			[16, 17]
κ, ε	orthorhombic	$Pna2_1$	a = 5.06 - 5.12 b = 8.69 - 8.79 c = 9.3 - 9.4	1.6-2.0		[18, 17]

The β phase is the thermodynamically stable structure up to the melting point (1800°C), while other phases tend to transform to β at a temperature range between 700°C-900°C. This is confirmed from the calculations of the Helmholtz free energies of the five Ga_2O_3 polymorphs [17] (Fig.1.4). For a wide temperature range the formation energies are in the order: $\beta < \varepsilon < \alpha < \delta < \gamma$. The difference in free energy between ε and β polymorphs decreases at high temperature and disappears at around 1600 K.

For this reason, the main research activities on gallium oxide material are concentrated on monoclinic β-Ga_2O_3, the only polymorph that can be grown from the melt.

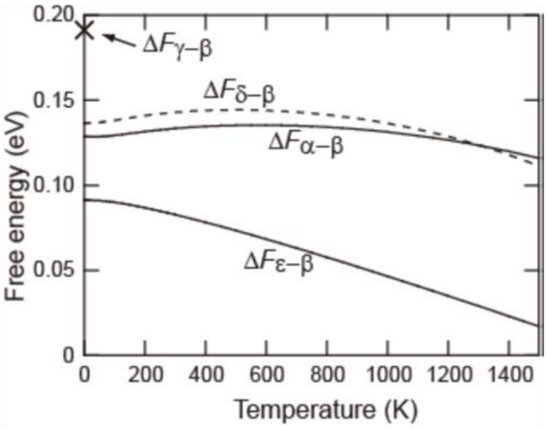

Fig.1.4 Different formation energies as a function of temperature between the β-phase and the metastable polymorphs [17].

Nonetheless, since β-Ga_2O_3 has a monoclinic symmetry (i) it presents strong anisotropic physical properties and (ii) the single crystals are susceptible to cleavage, which poses serious problems at the time of device manufacturing.

For these reasons, in the past few years there is an increasing interest on other Ga_2O_3 polymorphs, for instance the so-called ε-phase, that presents a crystallographic structure of higher symmetry than the β-phase. ε-Ga_2O_3 (i) shares a similarly high bandgap with β-Ga_2O_3 and the possibility to tune its electrical conductivity through extrinsic doping, (ii) better matching to sapphire substrates, and (iii) exhibits peculiar properties (very high intrinsic resistivity) to use it for solar blind photodetection applications.

1.2 The metastable ε-phase

1.2.1 Crystal structure

During the last few years, the ε-Ga_2O_3 crystal structure has been extensively studied by semiconductor researchers, since the real space group of this polymorph needed to be clarified. Initial X-ray study carried out by Mezzadri *et al.* [19] on ε-Ga_2O_3 thin films hinted at a hexagonal structure corresponding to the space group symmetry $P6_{3mc}$.

A detailed TEM study performed by Cora et *al.* [20] showed that the Ga_2O_3 crystal structure is arranged in ordered domains (Fig.1.5). Such domains (5-10 nm in size) are rotated to each other by 120° giving an orthorhombic structure ($Pna2_1$ space group symmetry), called κ-Ga_2O_3. The Ga_2O_3 crystal structure consists of a 4H (ABAC) stacking sequence, where Ga atoms are arranged in tetrahedral and octahedral sites between oxygen planes (Fig.1.6). Two types of layers replicate in the orthorhombic Ga_2O_3 crystal structure: layer containing purely octahedral sites (Ga_1 and Ga_2) and a mixed layer composed by octahedral (Ga_3) and tetrahedral (Ga_4) sites. The non-equivalent Ga sites have an occupancy probability of 2/3, ensuring the Ga_2:O_3 stoichiometry.

TEM investigations performed by Cora et *al.* [20] do not contradict the XRD results carried out by Mezzadri et *al.* [19]. The ambiguity about the real ε-Ga_2O_3 crystal structure is actually solved by considering the resolution of the probing technique. Since the x-ray radiation has a coherence length larger than domains size, a hexagonal structure is observed. Conversely, electrons in a TEM have smaller coherence length, then the true orthorhombic crystal structure is detected.

In conclusion, it is important to underline that ε-Ga_2O_3 is characterized by an orthorhombic structure at the nanoscale, therefore strictly speaking it is more correct to define this phase as κ. The ordered alignment of Ga atoms between oxygen layers leads to formation of 120° domains and pseudo-hexagonal crystallographic symmetry, popularly known as ε-phase.

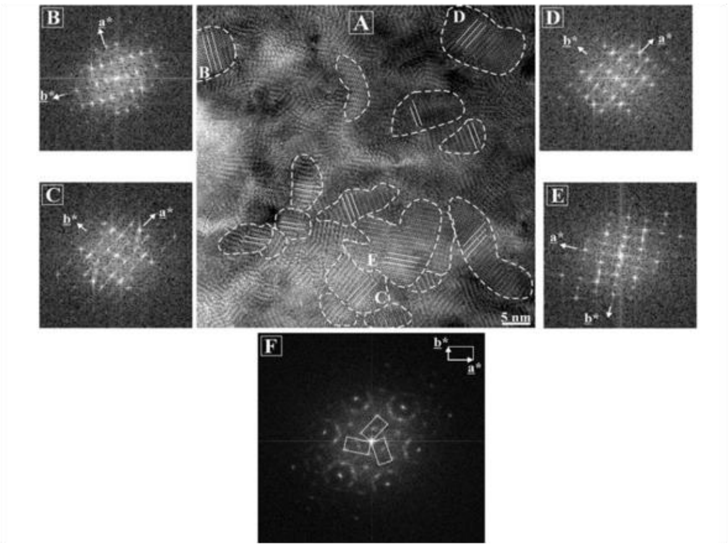

Fig.1.5 (a) Plane-view HRTEM image of the film in [001] projection. (b-e) are the corresponding Fast Fourier Transforms (FFTs). Such domains have orthorhombic structure, rotate to each other by 120 degree. (f) FFT overall image where a pseudo-hexagonal symmetry is shown. All the FFTs are from 5 nm x 5 nm large areas [20].

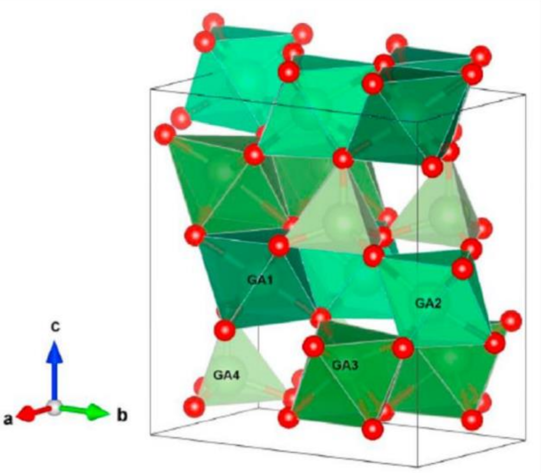

Fig.1.6 Unit cell of ε-Ga_2O_3: gallium and oxygen atoms are represented by green and red balls, respectively. Gallium atoms are arranged in tetrahedral (Ga_4) and octahedral (Ga_1, Ga_2, Ga_3) sites [20].

1.2.2 Electronic structure

Recently, the electronic band structure of ε-Ga_2O_3 has been intensely studied. First investigations were carried out by Kimi et *al.* [21], which proposed different theoretical methods to give information about the band structure of ε-phase. Different density functionals they used: the conventional PBEsol GGA [22] functional and B3LYP hybrid functional [23, 24]. By using the first model the underestimated bandgap value of 2.32 eV was obtained (Fig.1.7a), while B3LYP model allowed to obtain bandgap value of 4.62 eV (Fig.1.7b). The weak valence band maximum and the conduction band minimum occur both at the Γ-point, which evinces a direct bandgap of the material.

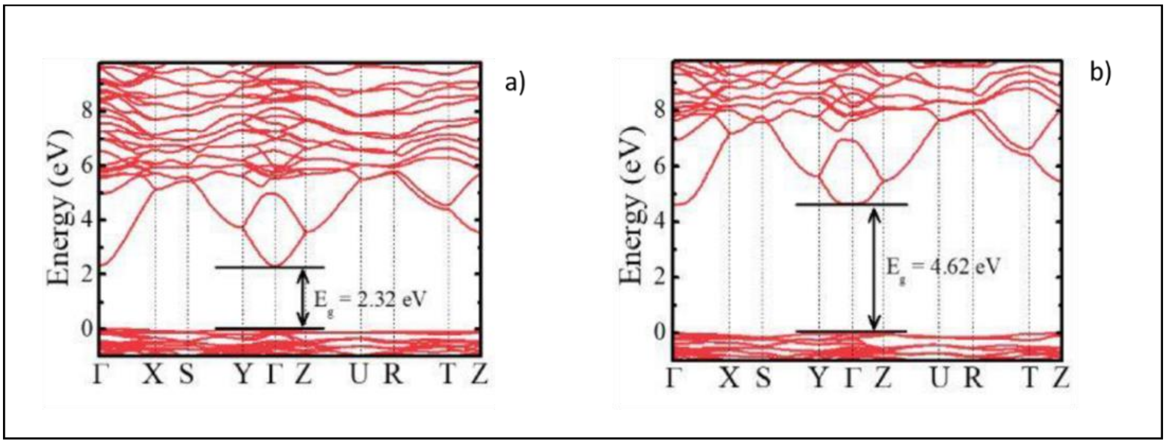

Fig.1.7 Electronic band structure calculated by PBEsol GGa functional (a) and B3LYP hybrid function (b) [21].

Mulazzi ed *al.* [25] also carried out peculiar investigations through GGA, HSE hybrid functionals [26] and ARPES measurements. The bandgap value of 2.32 eV is obtained by GGA, whereas HSE provides 4.26 eV (Fig.1.8). The latter value is not exactly the same reported by Kim et *al*. [21], suggesting that the DFT calculations can be affected by some uncertainties, as also observed in β-Ga_2O_3 [27].

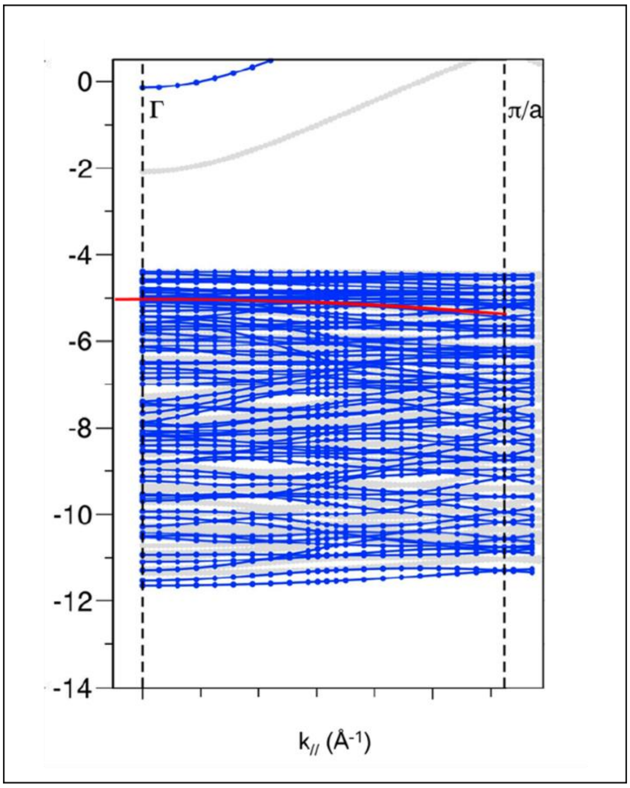

Fig.1.8 Electronic bands obtained with GGA (gray lines) and HSE (blue lines) models [25].

ARPES data (Fig.1.9a) show a wide valence band located at -6 eV from the Fermi level, with its binding energy minimum at the Γ-point. The energy distribution curve (EDC) taken at the Γ-point (Fig.1.9b) has been used to have an estimated value of the energy gap. The linear extrapolation of the EDC from the maximum peak to zero gives E_g = 4.41 eV, which is consistent with the value obtained by optical measurements on nominally undoped ε-Ga_2O_3 layers [28], considering the Fermi level located about 0.2 eV below the conduction band.

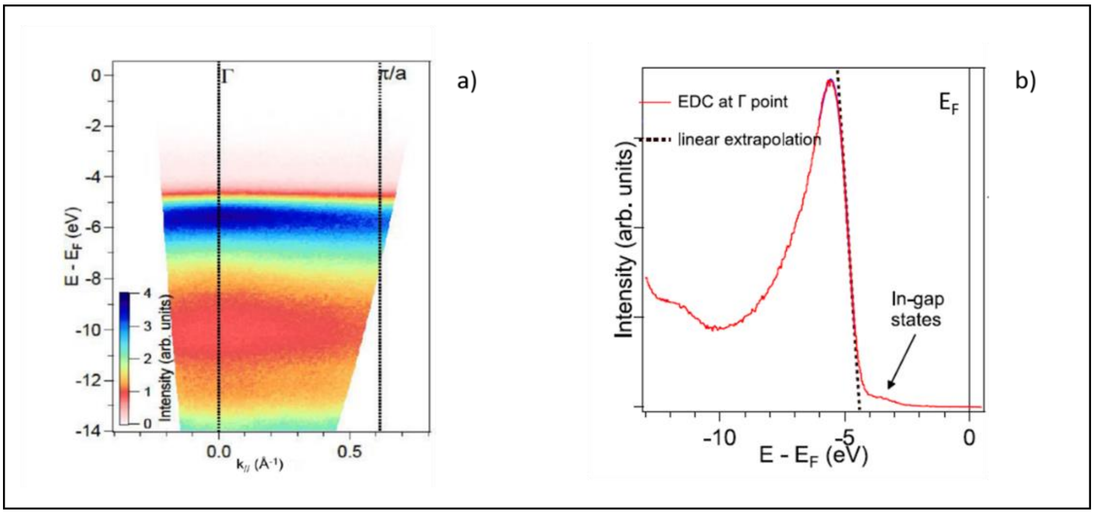

Fig.1.9 ARPES experimental data (a) and EDC profile referred to the Γ point (b) [25].

1.2.3 Optical properties

First investigation on the optical bandgap of the ε-phase was performed by Oshima et *al.* [29] in 2015 via transmittance measurements of a ε-Ga_2O_3 thin layer grown on c-plane AlN/SiC template. The bandgap was measured to be 4.9 eV from the Tauc plot, i.e. ($h\nu\alpha^2$) *vs* ($h\nu$), as shown in the inset of Fig.1.10. In a recent report, Pavesi *et al.* [28] extrapolated the optical bandgap of 4.6 eV by absorbance measurements on ε-Ga_2O_3 films grown by MOCVD.

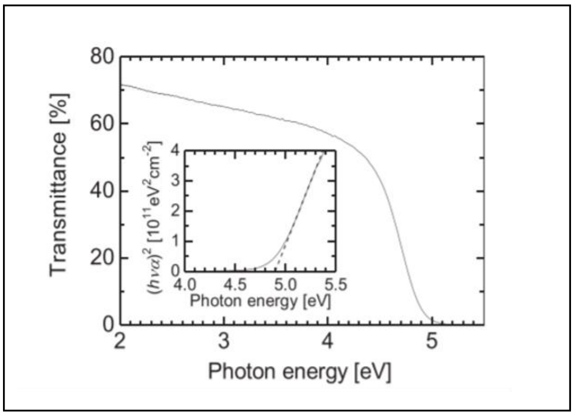

Fig.1.10 Transmittance spectrum of ε-Ga_2O_3. The inset shows the Tauc plot used to extrapolate the bandgap value (E_g = 4.9 eV) [29].

Further analysis concerning the anisotropic properties of ε-Ga_2O_3 were reported by Zhao *et al.* [30] from ellipsometric measurements.

The ordinary and extraordinary refractive indices are shown in Fig.1.11. The real part of the refractive indices decreases monotonically in the visible range. Moreover, the extinction coefficients (i.e. the imaginary parts of the refractive index) drop to zero at wavelength higher than 300 nm, which indicate the selective absorption of the material in the deep UV region. The bandgap values, which are derived from optical constants, are reported in Fig.1.12. The ordinary and extraordinary optical bandgaps are found to be 4.85±0.02 eV and 4.76±0.02 eV, respectively. The ordinary component well agrees with the bandgap value (4.9 eV) indicated by Oshima *et al.* [29], while the extraordinary component is smaller of about 0.09 eV than the ordinary one. Since Ga_2O_3 is a polar semiconductor, the bandgap variation can be due to the optical transitions, allowed by dipole, from valence sub-bands to conduction band minimum.

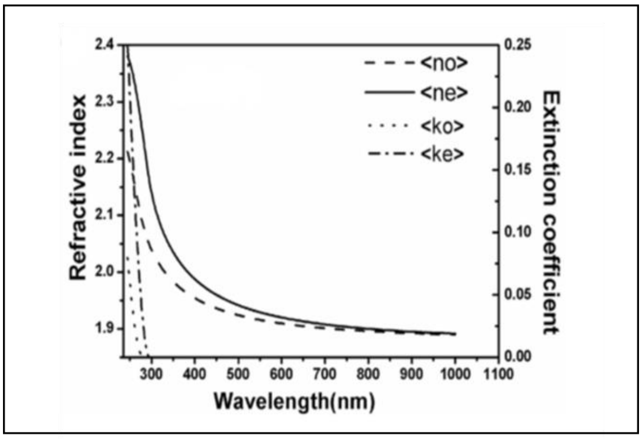

Fig.1.11 The ordinary (n_o) and extraordinary (n_e) refractive index together with the extinction coefficients (k_o,k_e) of ε-Ga_2O_3 layers [30].

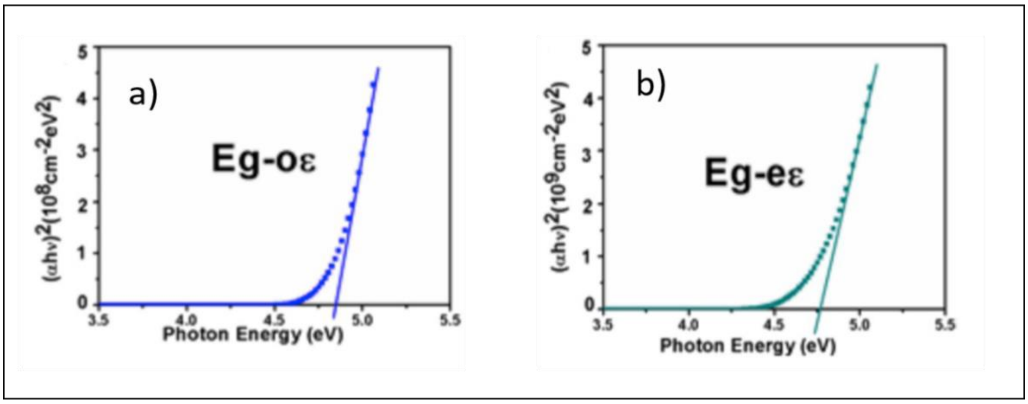

Fig.1.12 The ordinary (a) and extraordinary (b) optical bandgap of ε-Ga_2O_3. E_g values are denoted by vertical lines [30].

1.3 Survey of Ga_2O_3 applications

In this section an overview of the Ga_2O_3 applications will be reported.

Among Ga_2O_3 polymorphs, the β-phase is the most applied for high-power electronics (Schottky diodes, field effect transistors), UV optoelectronics (solar-blind photodetectors) and sensing systems (gas sensors). Unique properties of that polymorph combined with the possibility to grow it both as a single crystal directly from the melt [6] and epitaxial layers [7] are advantageous for a device fabrication. Vertical Schottky diodes based on β-Ga_2O_3 were obtained by Yang *et al.* [31] by depositing back Ohmic contacts of Ti (20nm)/Au (80 nm) and Schottky contacts Ni(20nm)/Au(80 nm) deposited at the top of the structures consisting of a Si-doped Ga_2O_3 epilayer grown on Sn-doped β-Ga_2O_3 substrate. These devices show promising results as an $R_{ON} = 6.7$ mΩ/cm², a BFOM (V_{br}^2/ R_{ON}) of 154.07 MW/cm² and an ideality factor close to unity. Green *et al.* [32] reported a β-Ga_2O_3 MOSFET by depositing a Sn-doped β-Ga_2O_3 thin film via MOVPE on a Mg-doped β-Ga_2O_3 substrate. It displays an electric field strength greater than 3.8 MV/cm, which is about one-half of the theoretical limit. Nevertheless, that is considered the highest measured electric field strength in a planar transition overcoming the theoretical values for bulk GaN (3 MV/cm) and SiC (3.18 MV/cm).

Recently, solar-blind photodetectors based on Ga_2O_3 are of large interest for applications in UV-C detection. The paper published by Tippins *et al.* [33] is considered the first study on

Ga_2O_3 - based photodetector. In this work, the spectral photoresponse of β-Ga_2O_3 single crystals in the UV-visible region is presented for the first time. These devices exhibit a strong spectral selectivity in the UV-C region, paving the way to employ this material as UV-C photodetector.
During the years, many Ga_2O_3 based photodetectors have been made, using different geometries, such as planar Metal-Semiconductor-Metal (MSM) structures and vertical Schottky photodiodes. Liu *et al.* [34] reported a planar ultraviolet photodetector consisting of β-Ga_2O_3 thin film, with a homo-self-templated buffer layer, grown by MBE on c-oriented sapphire substrate. Au(100nm)/Ti(50 nm) bilayers were used for the fabrication of the electrical contacts. This photodetector showed a current ratio (ratio photocurrent signal at λ=254 nm / dark current) of the order of 10^4 and a large responsivity of 259 A/W at 20 V.

Yu *et.al* [35] fabricated MSM photodetectors by depositing β-Ga_2O_3 thin films via PLD technique on Al_2O_3 (0001) substrates. The responsivity of 0.9 A/W at λ=250 nm radiation and the current ratio of about 10^5 were obtained.

Concerning other Ga_2O_3 polymorphs, Guo *et al* [36] used high quality α-Ga_2O_3 epilayers grown by laser molecular beam epitaxy (LMBE) on Al_2O_3 (300) substrates to fabricate simple MSM photodetectors. Such devices exhibited good UV detection performance with responsivity of 15.1 mA/W at 20V and EQE of 7.39%.

The first work concerning UV photodetectors based on γ-Ga_2O_3 was performed by Teng *et al* [37]. A response time to UV radiation less than 0.1 s and the UV-to-dark current ratio greater than 10^2 were obtained. Pavesi *et al* [28] fabricated simple photo-resistors by depositing high-resistive ε-Ga_2O_3 layers grown by MOCVD on c-oriented sapphire substrates. Such devices showed a UV-to-VIS photocurrent ratio greater than 10^3 and relatively fast response time ($t_{on/off}$ ~ 2 s) to UV radiation.

All these results suggest that gallium oxide has high potential for UV-C detector applications.

Attractive applications involve flame detectors based on Ga_2O_3. Oshima *et al*. [38] developed a Schottky vertical flame detector using a conductive single crystal β-Ga_2O_3 substrate grown by FZ method. Indium electrode is used as ohmic contact on the back side of the substrate and a PEDOT-PSS transparent electrode as Schottky contact. Significant 250-to-300 nm rejection ratio greater than 10^4 and ON-OFF photo-response transients shorter than 10 ms candidate β-Ga_2O_3 as an excellent material for flame sensing applications.

References

[1] S. J. Pearton, F. Ren, M. Tadjer and J. Kim, “Perspective: Ga2O3 for ultra-high power rectifiers and MOSFETS,” *Journal of Applied Physics,* vol. 124, no. 22, p. 220901, 2018.

[2] M. Higashiwaki, K. Sasaki, H. Murakami, Y. Kumagai, A. Koukitu, A. Kuramata and S. Yamakoshi, “Recent progress in Ga2O3 power devices,” *Semiconductor Science and Technology,* vol. 31, no. 3, p. 034001, 2016.

[3] L. De Boisbaudran, “On the chemical and spectroscopic characters of a new metal (gallium),” *The London, Edinburgh, and Dublin Philosophical Magazine and Journal of Science,* vol. 50, no. 332, pp. 414-416, 1875.

[4] R. Roy, V. G. Hill and E. F. Osborn, “Polymorphism of Ga2O3 and the system Ga2O3—H2O,” *Journal of the American Chemical Society,* vol. 74, no. 3, pp. 719-722, 1952.

[5] H. H. Tippins, “ Optical absorption and photoconductivity in the band edge of β-Ga2O3,” *Physical Review,* vol. 140, no. A316, 1965.

[6] Z. Galazka, R. Uecker, K. Irmscher, M. Albrecht, D. Klimm, M. Pietsch and R. Fornari, “Czochralski growth and characterization of β-Ga2O3 single crystals,” *Crystal Research and Technology,* vol. 45, no. 12, pp. 1229-1236, 2010.

[7] T. Oshima, N. Arai, N. Suzuki, S. Ohira and S. Fujita, “Surface morphology of homoepitaxial β-Ga2O3 thin films grown by molecular beam epitaxy,” *Thin Solid Films,* vol. 516, no. 17, pp. 5768-5771, 2008.

[8] K. Irmscher, Z. Galazka, M. Pietsch, R. Uecker and R. Fornari, “Electrical properties of β-Ga2O3 single crystals grown by the Czochralski method,” *Journal of Applied Physics,* vol. 110, no. 6, p. 063720, 2011.

[9] Y. W. Huan, S. M. Sun, C. J. Gu, W. J. Liu, S. J. Ding, H. Y. Yu and D. W. Zhang, “Recent Advances in β-Ga2O3–Metal Contacts,” *Nanoscale research letters,* vol. 13, no. 1, pp. 1-10, 2018.

[10] D. Guo, Z. Wu, P. Li, Y. An, H. Liu, X. Guo and W. Tang, “Fabrication of β-Ga 2 O 3 thin films and solar-blind photodetectors by laser MBE technology,” *Optical Materials Express,* vol. 4, no. 5, pp. 1067-1076, 2014.

[11] M. Higashiwaki, K. Sasaki, A. Kuramata, T. Masui and S. Yamakoshi, “Development of gallium oxide power devices,” *physica status solidi (a),* vol. 211, no. 1, pp. 21-26, 2014.

[12] M. Higashiwaki, K. Sasaki, A. Kuramata, T. Masui and S. Yamakoshi, “Gallium oxide (Ga2O3) metal-semiconductor field-effect transistors on single-crystal β-Ga2O3 (010) substrates,” *Applied Physics Letters,* vol. 100, no. 1, p. 013504, 2012.

[13] M. Higashiwaki and S. Fujita, Gallium Oxide: Materials Properties, Crystal Growth, and Devices, vol. 293, 2020.

[14] S. Stepanov, V. Nikolaev, V. Bougrov and A. Romanov, "Gallium oxide: properties and applications - a review," *Rev. Adv. Mater. Sci,* vol. 44, pp. 63-86, 2016.

[15] H. He, R. Orlando, M. A. Blanco, R. Pandey, E. Amzallag, I. Baraille and M. Rérat, " First-principles study of the structural, electronic, and optical properties of Ga2O3 in its monoclinic and hexagonal phases," *Physical Review B,* vol. 74, no. 19, p. 195, 2006.

[16] R. Roy, V. G. Hill and E. F. Osborn, "Polymorphism of Ga2O3 and the system Ga2O3—H2O," *ournal of the American Chemical Society,* vol. 74, no. 3, pp. 719-722, 1952.

[17] S. Yoshioka, H. Hayashi, A. Kuwabara, F. Oba, K. Matsunaga and I. Tanaka, "Structures and energetics of Ga2O3 polymorphs," *Journal of Physics: Condensed Matter,* vol. 19, no. 34, p. 346211, 2007.

[18] H. Y. Playford, A. C. Hannon, E. R. Barney and R. I. Walton, "Structures of uncharacterised polymorphs of gallium oxide from total neutron diffraction," *Chemistry–A European Journal,* vol. 19, no. 8, pp. 2803-2813, 2013.

[19] F. Mezzadri, G. Calestani, F. Boschi, D. Delmonte, M. Bosi and R. Fornari, " Crystal structure and ferroelectric properties of ε-Ga2O3 films grown on (0001)-sapphire," *Inorganic chemistry,* vol. 55, no. 22, pp. 12079-12084, 2016.

[20] I. Cora, F. Mezzadri, F. Boschi, M. Bosi, M. Čaplovičová, G. Calestani and R. Fornari, "The real structure of ε-Ga 2 O 3 and its relation to κ-phase," *CrystEngComm,* vol. 19, no. 11, pp. 1509-1516, 2017.

[21] J. Kim, D. Tahara, Y. Miura and B. G. Kim, "First-principle calculations of electronic structures and polar properties of (κ, ε)-Ga2O3," *Applied Physics Express,,* vol. 11, no. 6, p. 061101, 2018.

[22] J. P. Perdew, A. Ruzsinszky, G. I. Csonka, O. A. Vydrov, G. E. Scuseria, L. A. Constantin and K. Burke, "Restoring the density-gradient expansion for exchange in solids and surfaces," *Physical review letters,* vol. 100, no. 13, p. 136406, 2008.

[23] G. Kresse and J. Furthmüller, "Efficient iterative schemes for ab initio total-energy calculations using a plane-wave basis set," *Physical review B,* vol. 54, no. 16, p. 11169, 1996.

[24] G. Kresse and D. Joubert, "From ultrasoft pseudopotentials to the projector augmented-wave method," *Physical review b,* vol. 59, no. 3, p. 1758, 1999.

[25] M. Mulazzi, F. Reichmann, A. Becker, W. M. Klesse, P. Alippi, V. Fiorentini and R. Fornari, "The electronic structure of ε-Ga2O3," *APL Materials,* vol. 7, no. 2, p. 022522, 2019.

[26] J. Heyd, G. E. Scuseria and M. Ernzerhof, "Hybrid functionals based on a screened Coulomb potential," *The Journal of chemical physics,* vol. 118, no. 18, pp. 8207-8215, 2003.

[27] J. Heyd, G. E. Scuseria e M. Ernzerhof, «Hybrid functionals based on a screened Coulomb potential,» *The Journal of chemical physics*, vol. 118, n. 18, pp. 8207-8215, 2003.

[28] M. Pavesi, F. Fabbri, F. Boschi, G. Piacentini, A. Baraldi, M. Bosi, E. Gombia, A. Parisini and R. Fornari, “ ε-Ga2O3 epilayers as a material for solar-blind UV photodetectors,” *Materials Chemistry and Physics,* vol. 205, pp. 502-507, 2018.

[29] Y. Oshima, E. G. Víllora, Y. Matsushita, S. Yamamoto and K. Shimamura, “Epitaxial growth of phase-pure ε-Ga2O3 by halide vapor phase epitaxy,” *Journal of Applied Physics,* vol. 118, no. 8, p. 085301, 2015.

[30] M. Zhao, R. Tong, X. Chen, T. Ma, J. Dai, J. Lian and J. Ye, “Ellipsometric determination of anisotropic optical constants of single phase Ga2O3 thin films in its orthorhombic and monoclinic phases,” *Optical Materials,* vol. 102, p. 109807, 2020.

[31] J. Yang, S. Ahn, F. Ren, S. J. Pearton, S. Jang, J. Kim and A. Kuramata, “High reverse breakdown voltage Schottky rectifiers without edge termination on Ga2O3,” *Applied Physics Letters,* vol. 110, no. 19, p. 192101, 2017.

[32] A. J. Green, K. D. Chabak, E. R. Heller, R. C. Fitch, M. Baldini, A. Fiedler and G. H. Jessen, “3.8-MV/cm Breakdown Strength of MOVPE-Grown Sn-Doped beta Ga2O3 MOSFETs,” *IEEE Electron Device Letters,* vol. 37, no. 7, pp. 902-905, 2016.

[33] H. H. Tippins, “Optical absorption and photoconductivity in the band edge of β−Ga2O3,” *Physical Review,* vol. 140, no. 1A, p. A316, 1965.

[34] X. Z. Liu, P. Guo, T. Sheng, L. X. Qian, W. L. Zhang and Y. R. Li, “β-Ga2O3 thin films on sapphire pre-seeded by homo-self-templated buffer layer for solar-blind UV photodetector,” *Optical Materials,* vol. 51, pp. 203-207, 2016.

[35] F. P. Yu, S. L. Ou and D. S. Wuu, “Pulsed laser deposition of gallium oxide films for high performance solar-blind photodetectors,” *Optical Materials Express,* vol. 5, no. 5, pp. 1240-1249., 2015.

[36] D. Y. Guo, X. L. Zhao, Y. S. Zhi, W. Cui, Y. Q. Huang, Y. H. An, P. Li, Z. Wu and W. H. Tang, “Epitaxial growth and solar-blind photoelectric properties of corundum-structured α-Ga2O3 thin films,” *Materials Letters,* vol. 164, pp. 364-367, 2016.

[37] Y. Teng, L. X. Song, A. Ponchel, Z. K. Yang and J. Xia, “Self-Assembled Metastable γ-Ga2O3 Nanoflowers with Hexagonal Nanopetals for Solar-Blind Photodetection,” *Advanced Materials,* vol. 26, no. 36, pp. 6238-6243, 2014.

[38] T. Oshima, T. Okuno, N. Arai, N. Suzuki, H. Hino and S. Fujita, “Flame detection by a β-Ga2O3-based sensor,” *Japanese Journal of Applied Physics,* vol. 48, no. 1R, p. 011605, 2009.

Chapter 2 – Experimental methods

The second chapter is devoted to the description of the experimental techniques employed for the PhD research activity. Firstly, the basic operation principles of the MOCVD growth process used to produce ε*-*Ga_2O_3 *epilayers will be reported. An overview of the sputtering deposition technique used for doping the material as well as to make electrical contacts on* ε*-*Ga_2O_3 *epilayers will be given. Finally, the experimental techniques used for electrically characterize the* ε*-*Ga_2O_3 *samples will be presented.*

2.1 Deposition techniques

2.1.1 MOCVD growth method

The crystallographic quality of each material plays a key role on the performance of any electronic devices, such as detectors, p-n diodes, and transistors. To obtain a high crystallographic quality the epitaxial technique is used, that is the growth of a thin film on a monocrystalline substrate. Epitaxy can be generally classified into two categories: *i)* homoepitaxy in the case of identical structure and chemical composition between the epilayers and the substrate; *ii)* heteroepitaxy when the chemical composition or the crystallographic structure of epilayer and substrate are different.

Several techniques are currently available for depositing epilayers. They can be classified into three main group: *(i)* vapour phase epitaxy (VPE), *(ii)* liquid phase epitaxy (LPE) and *(iii)* molecular beam epitaxy (MBE). Among them, one of the most popular method for growing high quality crystalline structures is metal organic vapour phase epitaxy (MOCVD), that is a subgroup of the VPE technique.

In MOCVD growth process gaseous precursors are injected into the growth chamber via a carrier gas, generally H_2 or inert gas like Ar, N_2 or He, and react with the substrate surface to form a crystalline thin film. By a careful control of the growth parameters (temperature, partial pressure of the precursors gas) it is possible to obtain high quality thin films.

Some advantages make the MOCVD growth method the most employed VPE technique, which are briefly summarized:

- Accurate stoichiometry of deposited materials can be obtained by control of the gas phase composition.
- A wide choice of precursors is available, which permits to deposit many different materials.
- Relatively high growth rates can be obtained, which allow to obtain thick layers.

Currently, MOCVD growth method is used by various groups to achieve ε-Ga_2O_3 epilayers [1, 2, 3, 4]. Among them, single phase ε-Ga_2O_3 layers have been successfully deposited by MOCVD on c-oriented Al_2O_3 substrates by Boschi et *al* [4] in 2016. Layers of ε-Ga_2O_3 were grown at different temperatures but the most significant result was obtained at a temperature of 650 °C. In this case films shown a good morphology as confirmed by SEM analysis, and XRD profiles exhibited the presence of the ε-phase only [4].

Following the results of Boschi et *al*. [4], similar growth conditions were used to produce the ε-Ga_2O_3 samples employed for the present PhD research work.

ε-Ga_2O_3 epilayers are grown by a home-made MOCVD reactor placed at IMEM-CNR Institute. The reactor is formed by *(i)* a graphite susceptor with a circular socket to contain a 2 inches substrate, *(ii)* a quartz cap on the top to prevent particulates to fall onto the substrate during the deposition and *(iii)* a porous graphite insulator placed around the susceptor to inhibit heat dissipation (Fig.2.1).

The susceptor and the substrate on the top are heated by two resistor plugs. The growth temperature is set by a PID (proportional-integral-derivative) controller which communicates with a thermocouple located in the centre of the susceptor.

Trimethylgallium (TMGa) and ultrapure water are used as precursors, with H_2 or He as carrier gases. Both precursors are stored in stainless steel vessels “bubblers” and maintained at a temperature of 1-5 °C and 30 °C, respectively.

The total pressure of the reactor is controlled by a rotary pump, while the partial pressures of the precursors are established by means of mass flow controllers (MFCs).

The system is composed by two separate gas lines used to transfer the precursors into the growth chamber and a vent line which allows a controlled flow of the gas species before they are injected into the chamber. The reaction by-products and residual process gas are sent to a cracking furnace at about 800 °C, which allows the decomposition of unreacted species before releasing the exhaust gases into the atmosphere. Main growth parameters of nominally undoped ε-Ga_2O_3 samples are shown in Tab.2.1.

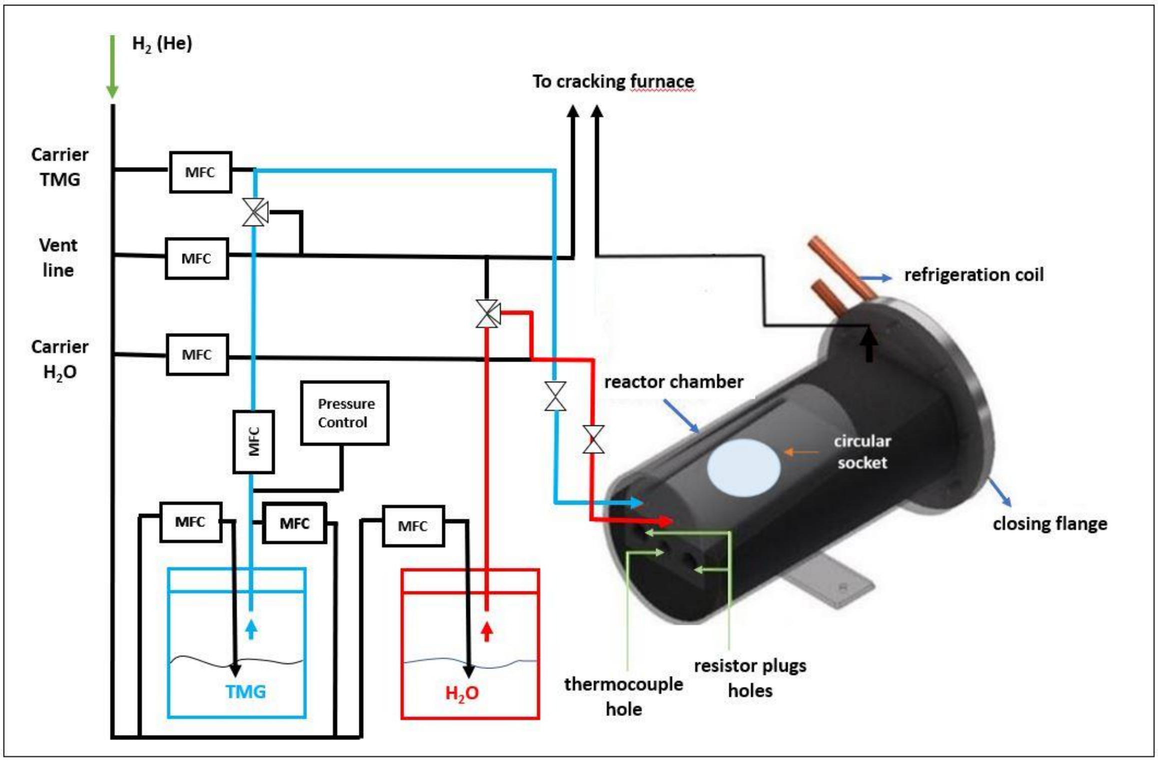

Fig.2.1 Schematic diagram of the MOCVD reactor used for ε-Ga_2O_3 thin films deposition.

Tab.2.1 Collection of the most representative undoped Ga_2O_3 samples and related growth parameters.

SAMPLE #	**T (°C)**	**P (mbar)**	**P_H_2O**	**P_TMGa**	**H_2O/ TMGa**	**Carrier gas**	**Time (min)**
224	650	100	6.33E-02	4.83E-05	1300	He	60
251	650	100	6.63E-02	1.13E-04	320	He	30
324	600	100	1,7E-02	1.17E-04	145	He	40
398	610	60	3,31E-02	9,49E-05	348	H_2	60
421	610	60	3,31E-02	9,49E-05	348	H_2	22
422	610	60	3,31E-02	9,49E-05	348	H_2	22
425	610	60	3,31E-02	9,49E-05	348	H_2	320
435	610	60	1,7E-02	6,71E-05	252	H_2	60
436	610	60	1,7E-02	4,86E-05	348	H_2	60
449	610	60	5,18E-03	4,9E-05	104	H_2	62
465	610	60	2,84E-02	9,49E-05	299	H_2	22
468	650	70	2,84E-02	9,49E-05	299	He	22
469	650	100	1.35E-01	6.59E-04	205	He	15
470	650	100	4,60E-02	9,20E-05	499	He	15
474	650	100	1.35E-01	6.59E-04	205	He	15
478	650	100	1.35E-01	6.59E-04	205	He	15
479	650	100	1.35E-01	6.59E-04	205	He	15
481	650	100	6.88E-02	3.35E-04	205	He	15
482	610	100	1.35E-01	6.59E-04	205	He	15
483	650	100	1.35E-01	6.59E-04	205	He	15
484	650	100	1.35E-01	6.59E-04	205	He	15
489	650	100	7.69E-02	3.73E-04	205	He	120
490	650	100	1.35E-01	6.59E-04	205	He	90
491	650	100	1.35E-01	6.59E-04	205	He	15
497	650	100	1.35E-01	6.59E-04	205	He	15
509	610	60	1.70E-02	4.86E-05	348	H_2	100
519	650	100	1.35E-01	6.59E-04	205	He	15
535	610	60	1.70E-02	4.86E-05	348	H_2	110
550	650	100	1.35E-01	6.59E-04	205	He	15
554	650	100	1.35E-01	6.59E-04	205	He	15
555	650	100	1.35E-01	6.59E-04	205	He	15
591	650	100	1.35E-01	6.59E-04	205	He	30
592	650	100	1.35E-01	6.59E-04	205	He	60
593	650	100	1.35E-01	6.59E-04	205	He	10
594	650	100	1.35E-01	6.59E-04	205	He	5

2.1.2 Sputtering technique

The sputtering deposition technique was used to produce n-type doping of ε-Ga_2O_3, as well as to make reliable ohmic contacts on ε-Ga_2O_3.

Sputtering is a common physical vapour deposition (PVD) technique used for deposition of a wide variety of materials (metals, semiconductors, and insulators) in the form of thin films.

Basically, this technique involves the collisions of energetic ions with a target surface, which in principle lead to ejection of target atoms.

In a sputtering chamber the target (cathode) and the substrate (anode) are mounted on two parallel holders and connected to the power supply. In vacuum conditions (pressure range between 10^{-2} Pa - 10^{-4} Pa), by applying an appropriate voltage between the electrodes, in presence of inert Argon gas the glow discharge is produced. A schematic of a sputtering system is shown in Fig.2.2.

The material (target) to be deposited is bombarded by Argon ions (Ar^+), which are generated by the collisions among electrons and Ar atoms into the chamber.

During the ion bombardment, secondary electrons are also emitted from the target surface, which play a key role in maintaining of a continuous glow discharge.

The extraction of atoms from the target surface is allowed thanks to the energy and momentum exchange between the ions Ar^+ and the source atoms. Therefore, the sputtered atoms can reach the substrate and condensate on it as a thin layer.

Different materials such as oxides, nitride, and carbides can be deposited from an elemental or alloy target by introducing into the sputtering chamber a reactive gas (O_2) together with the Ar gas, which play a key role in the stoichiometry of the deposited compound. This process is called “reactive sputtering deposition”.

The sputtering system can work in direct current (dc) or in radio frequency (rf) regime, depending on the type of the power supply employed (direct or alternating current, respectively). The dc sputtering is only applicable to the deposition of conductive materials, since if the target is made of insulating material, a positive charge is accumulated on the target surface, inhibiting the glow discharge. Such limitation can be overcome using the rf sputtering method by capacitively coupling the power supply to the cathode (target).

To summarize, the major peculiarities of the sputtering technique are the following:

- Deposition of wide range of materials (metal, insulators, alloys and compounds).
- Deposition of large area thin films with uniform thickness, which allows a high scalability at an industrial level.
- Reproducibility of the deposition process.
- On the other hand, the deposition rate is quite low (< 0,02 µm s^{-1}).

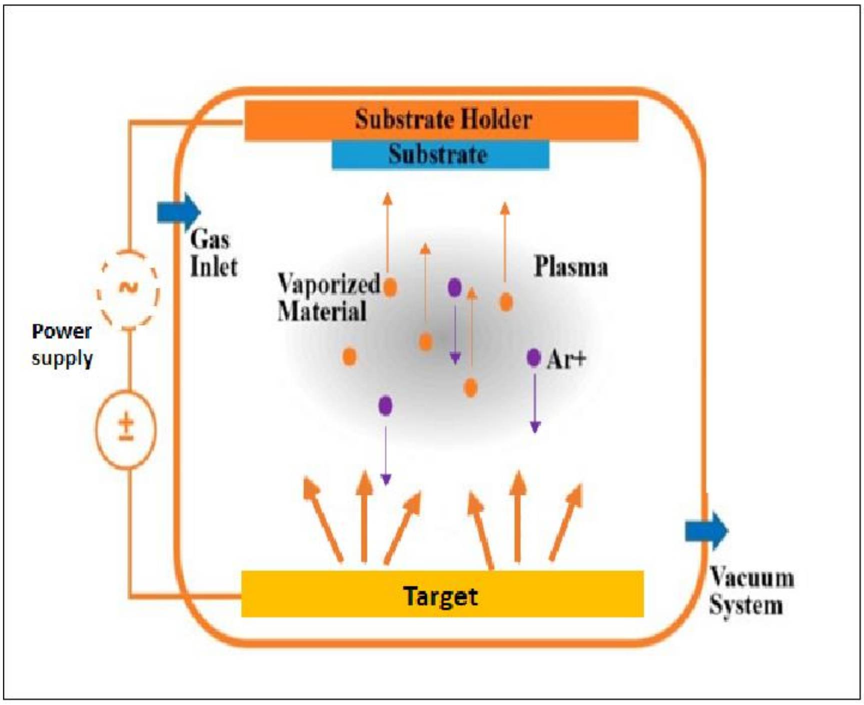

Fig.2.2 Schematic illustration of sputtering process [5].

2.2 Characterization techniques

2.2.1 van der Pauw method

The van der Pauw (vdP) method is a common technique for measuring resistivity and Hall effect in a semiconductor material. Being a four-probe investigation technique, the resistivity measurement is not affected by any contact resistance effects.

This method is applicable to samples of arbitrary shape and does not require a precise geometry like in the case of Hall bar. However, some conditions must be satisfied:

- Four ohmic contacts should be placed close as possible at the edges of the sample.
- A homogeneous sample of uniform thickness is required.
- The area of each contact must be much smaller than the sample area (at least one order of magnitude smaller).

In vdP configuration, the resistivity measurements are carried out by injecting current into two adjacent contacts and reading the generated voltage between two other contacts. The resistivity is obtained from a total of eight voltage measurement combinations (four pairs and current reversed), as shown in Fig.2.3.

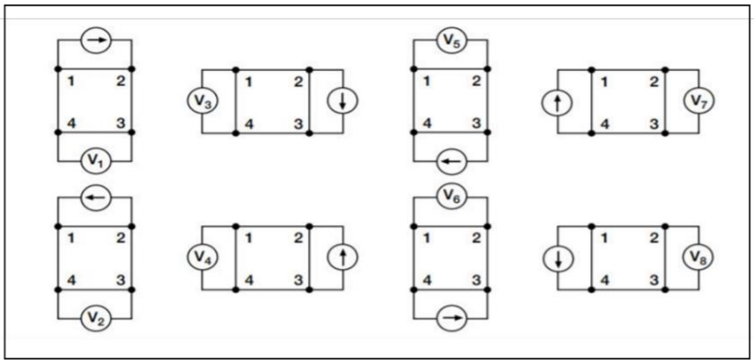

Fig.2.3 Schematic of van der Pauw configurations used to determine the sample resistivity.

From the voltage measurements, two resistivity values ρ_A and ρ_B can be defined as follows:

$$\rho_A = \frac{\pi d}{ln2}\left(\frac{V_1 - V_2 + V_3 - V_4}{4I}\right) f_a \qquad (2.\ 1)$$

$$\rho_B = \frac{\pi d}{ln2}\left(\frac{V_5 - V_6 + V_7 - V_8}{4I}\right) f_b \qquad (2.\ 2)$$

where d is the thickness of the sample, V_i the measured voltages, I the current signal, f_a and f_b are defined the vdP geometrical factors, which are related to the sample symmetry (i.e., $f_a = f_b = 1$ for perfect square sample or symmetrically positioned contacts).

Moreover, it is possible to define the resistance ratios R_A and R_B as follows:

$$R_A = \frac{V_1 - V_2}{V_3 - V_4} \qquad (2.\ 3)$$

$$R_B = \frac{V_5 - V_6}{V_7 - V_8} \qquad (2.\ 4)$$

Generally, the vdP geometrical factor f and the resistance ratio R satisfy the following relation:

$$\frac{R-1}{R+1} = \frac{1}{ln2} arc\ cosh\left(\frac{e^{ln2/f}}{2}\right) f \qquad (2.\ 5)$$

Consequently, knowing the f value is possible to estimate ρ_A and ρ_B using eqs. (2.1, 2.2).

Finally, the resistivity average ρ_{AVG} can be calculated taking into account the values ρ_A and ρ_B:

$$\rho_{AVG} = \frac{\rho_A + \rho_B}{2} \tag{2. 6}$$

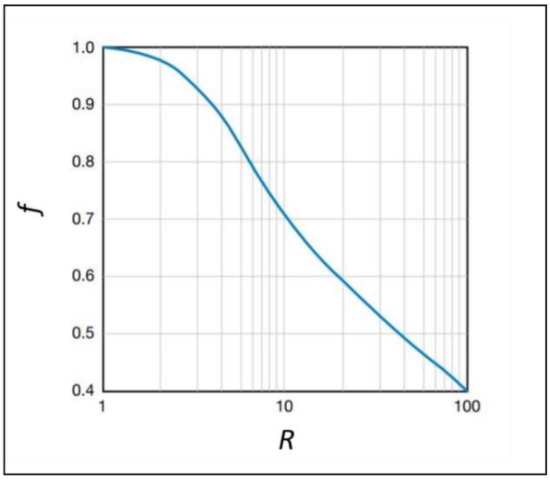

Fig.2.4 Plot of the geometric factor *f* as a function of the resistance ratio (see Eq. 2.5). The higher the resistance ratio the larger the deviation of geometrical factor from the unity, which means a lowering of the sample symmetry [6].

Information about the type of doping, the carrier concentration and the mobility of the sample can be achieved by Hall effect measurements. In this case, by applying a magnetic field B perpendicular to the direction of the current flow I, the so-called Hall voltage V_H is created. (Fig.2.5).

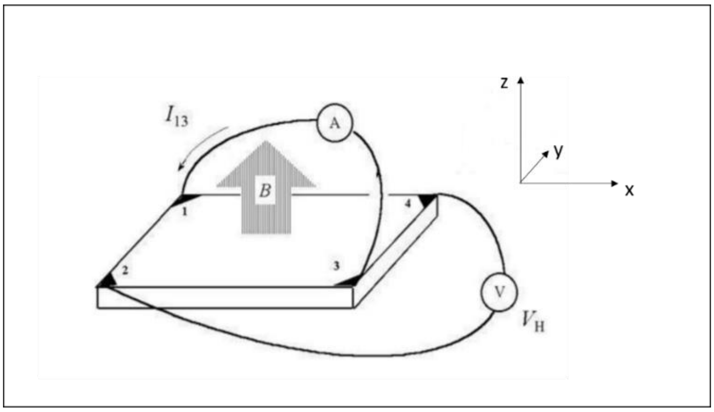

Fig.2.5 Schematic of a van der Pauw configuration used to determine the Hall voltage V_H.

Knowing the value of I, B, and V_H one can determine the Hall coefficient R_H as follows:

$$R_H = \frac{dV_H}{IB} \tag{2. 7}$$

It is important to point out that the sign of the Hall coefficient reveals the doping type of the material ($R_H > 0$ for p-type and $R_H < 0$ for n-type).

By reversing the directions of the current and the magnetic field (positive and negative z-direction), eight V_H values are recorded, that allow to achieve two Hall coefficients R_{HC} R_{HD} , with average value:

$$R_{Havg} = \frac{R_{HC} + R_{HD}}{2} \tag{2. 8}$$

Consequently, the carrier concentration is given by:

$$n = \frac{1}{e\left|R_{H\,avg}\right|} \tag{2. 9}$$

while the Hall mobility is obtained from the expression:

$$\mu = \frac{\left|R_{H\,avg}\right|}{\rho_{avg}} \tag{2. 10}$$

2.2.2 Transfer Length Method (TLM)

The Transfer Length Method is a useful technique used to determine the specific contact resistance ρ_c associated to the metal/semiconductor contact. The method involves an array of contacts of length W, width Z, spaced by increasing distances L_i. (Fig.2.6)

Probes are applied to pairs of contacts and the resistance between them is measured by applying a voltage across the contacts and measuring the resulting current. Linear and symmetric I-V characteristics for all the contact pairs are strictly required for this method.

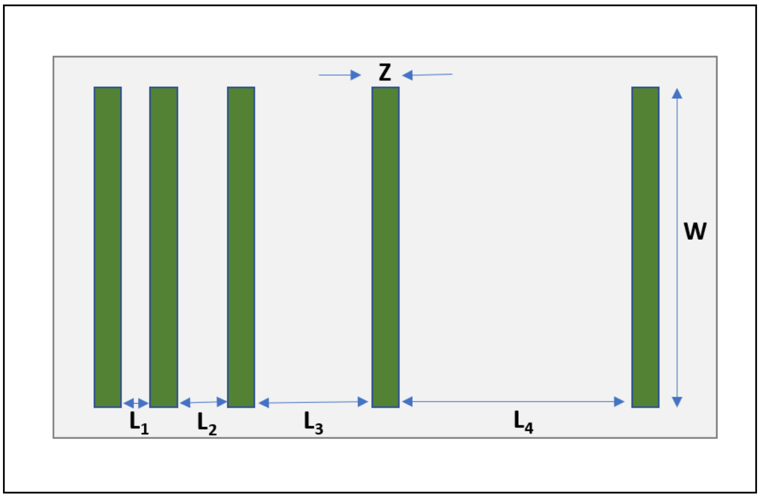

Fig.2.6 Schematic representation of TLM structure. Electrical contacts (green in the figure) are spaced by increasing distance L_i.

The resistance between one contact pair is the sum of two contact resistances and the resistance of the semiconductor i.e., $R_T = R_{sem} + 2R_c$.

The contact resistance R_c is related to the specific contact resistance ρ_c , which is independent of the contact geometry, by the following expression:

$$R_c = \frac{\rho_c}{W L_T} \tag{2. 11}$$

where L_T is the so-called transfer length defined as the average distance that the electrons travel in the semiconductor before they flow up into the contact.
It is defined as:

$$L_T = \frac{R_C W}{R_{sh}} \tag{2. 12}$$

By plotting resistance values, obtained from the slopes of each I-V characteristic, as a function of the contact spacing L, is possible to determine the sheet resistance R_{sh} and the contact resistance R_c. In particular, from the slope of the curve is possible to extract R_{sh} and the intercept of the curve gives $R_T = 2R_c$ (Fig.2.7), as two contacts are involved in a single measurement. Successively, the transfer length L_T is determined by Eq. (2.12), which leads to the specific contact resistance ρ_c=$R_c W L_T$.

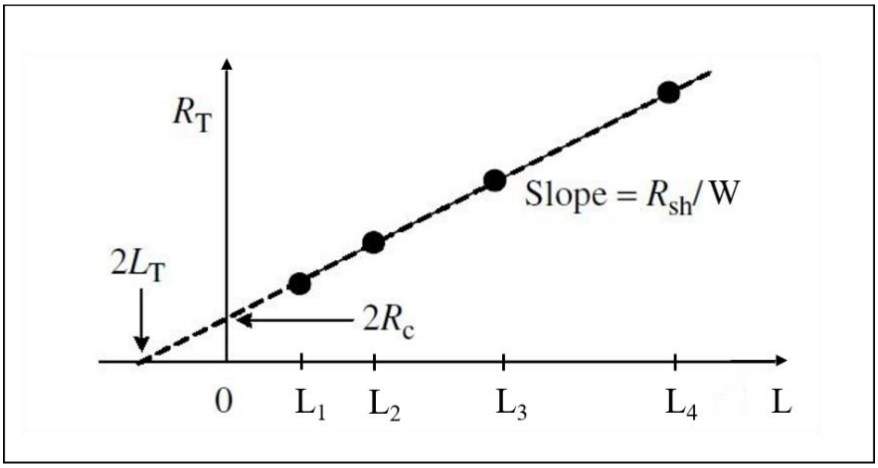

Fig.2.7 R-L profile used to extract the sheet resistance R_{sh} and the contact resistance R_c. The plot gives also an information of the transfer length L_T, by extrapolating back to the L-axis [6].

2.2.3 Photo-conductivity measurements

Photoconductivity is an electro-optical phenomenon in which the electrical conductivity of a semiconductor increases due to the absorption of electromagnetic radiation.

The conductivity σ_0 of an intrinsic semiconductor is expressed as:

$$\sigma_0 = e(n_0\mu_n + p_0\mu_p) \tag{2. 13}$$

where, e is the electronic charge, n_0 and p_0 are the concentrations of free electrons and holes at equilibrium, respectively, and μ_n and μ_p the electron and hole mobilities.

Let us consider a homogenous semiconductor (n_0 and p_0 are uniformly distributed throughout the material) contacted by metallic electrodes at the edges of the sample (Fig.2.8). Under uniform illumination, photons with energy greater than the bandgap energy of the semiconductor ($E_{ph} > E_G$), generate equal excess of photocarriers (electrons and holes) $\Delta n = \Delta p$, which are collected at the electrodes by applying a voltage V.

The density of photogenerated carriers can be defined as:

$$\Delta n = \Delta p = \frac{\eta_{ext}\phi\tau}{A_c d} \tag{2. 14}$$

where, η_{ext} is the external quantum efficiency, ϕ is the photon flux (number of photons per unit time), τ the carrier lifetime, A_c the effective illuminated area and d the thickness of the sample.

The change in conductivity is given by:

$$\Delta\sigma = e(\mu_n\Delta n + \mu_p\Delta p) = \frac{J_{ph}}{E} \tag{2. 15}$$

where, J_{ph} is the photocurrent density and $E = \frac{V}{L}$ is the applied electric field.

Eq.(2.15) is the classic expression of the conductivity in an ideal photoconductor where the photogenerated carriers are assumed uniformly distributed throughout the material and carrier trapping phenomena are not considered. These assumptions are generally not valid in a high-resistivity compensated semiconductor, as in the case of ε-Ga_2O_3. A careful analysis of photoconduction mechanisms, taking into account the transport properties of ε-Ga_2O_3 is reported in the Chapter 4, section 4.2.1.

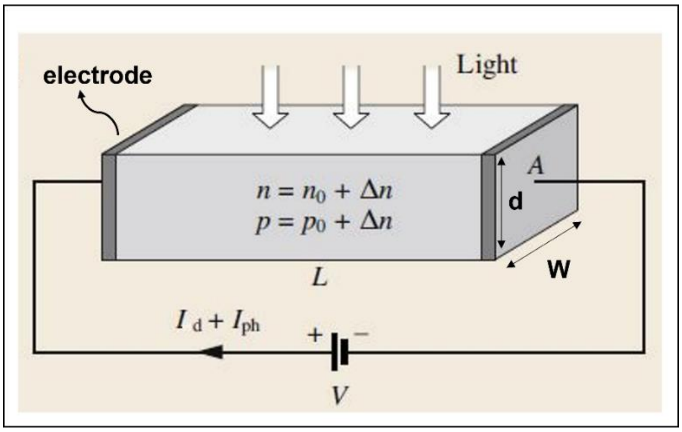

Fig.2.8 The basic experimental arrangement of a photoconductor device. V is the applied voltage, L the sample length, A = W·d is the cross-sectional area with d the sample thickness and W the contact width. I_d is the dark current and I_{ph} the photocurrent generated by the illumination.

Electrical measurements of UV photodetectors based on ε-Ga_2O_3 were carried out in dark and under illumination condition by using a Keithley Source-Meter Mod.2400, applying a voltage across each contact pair and measuring the resulting current. The spectral photoresponse measurement was performed by an Oriel optical system consisting in a 250W Quartz Tungsten Halogen Lamp (QTH) and a monochromator 130/74000 working in the spectral range 200-1000 nm (Fig.2.9a). The spectral lamp emission was measured with a calibrated photodiode sensor (Newport Optical Power Meter 818 UV). Photoresponse under sunlight condition were performed by using a solar simulator Oriel Mod. 81160-1000, designed to provide light with spectral composition approximating natural sunlight, in AM 1.5 conditions (Fig.2.10).

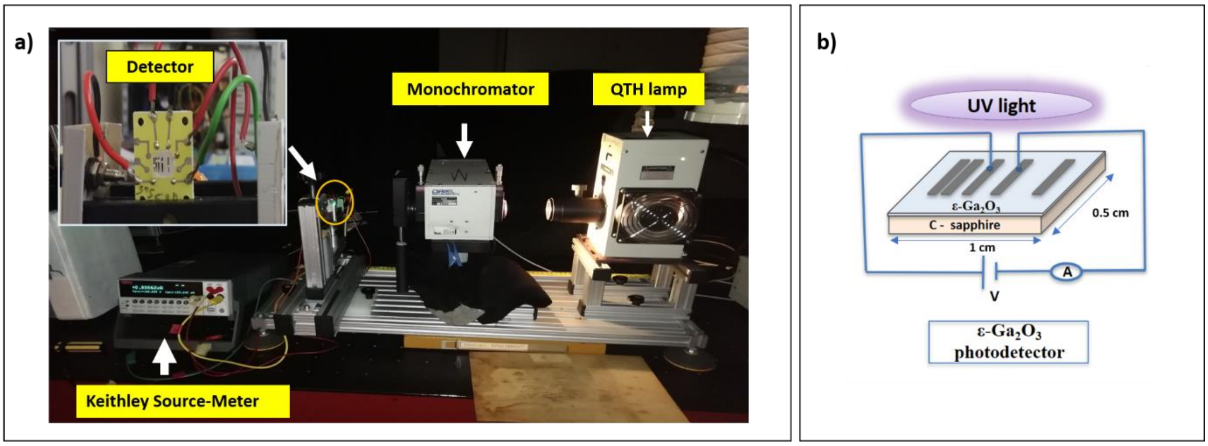

Fig.2.9 (a) Picture of the Oriel optical system used to characterize test devices. In the inner panel magnification of the detector is showed. (b) Schematic illustration of a typical test structure.

Fig.2.10 Photograph of the Oriel solar simulator used to test the effective solar blindness of photodetector.

2.2.4 Mercury probe system

Mercury probe system was used to determine the 3d carrier density of ε-Ga_2O_3 thin films by Capacitance-Voltage (C-V) measurements, making use of temporary metallic contacts provided by liquid Hg forced to adhere to film surface.

Under vacuum condition, mercury is brought into contact with the Ga_2O_3 layer forming two electrical contacts of different areas, as shown in Fig.2.11.

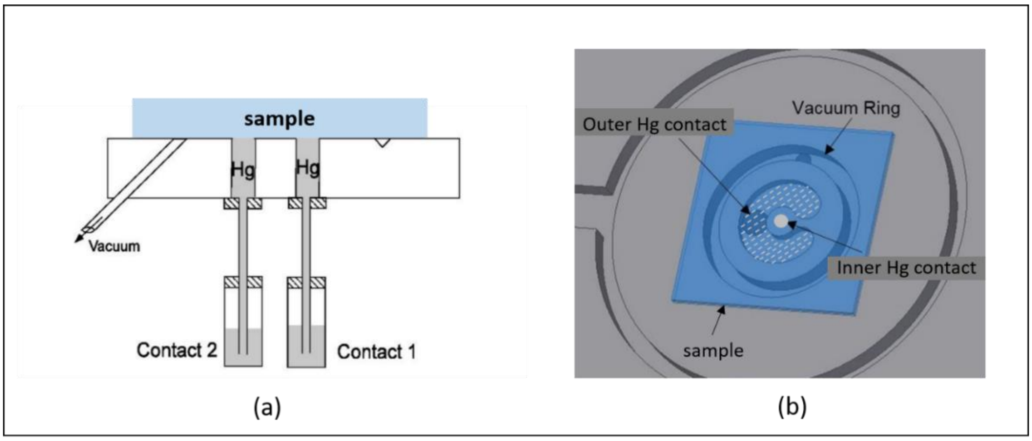

Fig.2.11 Schematic diagram (a) and contact configuration (b) of the Mercury probe setup.

The outer contact with larger area has a capacitance C_o whereas the inner contact presents a smaller area with a capacitance C_i. Since $C_o >> C_i$, the total capacitance can be approximated to C_i. Therefore, the inner contact acts as a Schottky gate electrode, while the outer contact operates as an ohmic contact.

When a reverse bias V_R is applied to the inner contact with respect to the outer contact, a variation of the depletion region width W is obtained. Such a quantity is related to the 3d carrier concentration *n* as follows:

$$W = \sqrt{\frac{2\varepsilon_0\varepsilon(V_R + V_{bi})}{en}} = \frac{\varepsilon_0\varepsilon A}{C} \tag{2. 16}$$

where ε_0 is the vacuum permittivity, ε is the relative dielectric constant, V_{bi} is the built-in potential, e is the elementary charge, C is the Schottky barrier's capacitance and A is the area of the inner contact (7.3 × 10^{-8} m^2).
Eq (2.13) may be re-written as:

$$\frac{1}{C^2} = \frac{2}{A^2 e\varepsilon_0\varepsilon n}(V_R + V_{bi}) \tag{2. 17}$$

Then, the carrier concentration n can be calculated from the slope m of the curve $(\frac{1}{C^2}$ vs $V_R)$, expressed as:

$$m = \frac{2}{A^2 e\varepsilon_0\varepsilon n} \tag{2. 18}$$

It should be pointed out that the net doping concentration measured with this experimental technique is limited by the amount of the depleted charge in the Schottky barrier, typically confined to a few nanometers of the layer. Additional information about the 3d carrier density can be collected via Seebeck coefficient measurements

2.2.5 Seebeck coefficient measurements

The Seebeck effect is a phenomenon in which a thermal gradient applied to a semiconductor generates a thermoelectric potential into the material. Such a potential is defined as:

$$V_{TH} = -S\,(\Delta T) \tag{2. 19}$$

where S is the Seebeck coefficient and ΔT the temperature gradient applied to the semiconductor. The Seebeck coefficient is a relevant thermoelectric parameter, which provides significant information about a semiconductor material such as the 3d carrier concentration n, the carrier effective mass m*, and the type of the majority carriers (S < 0 for electrons, S > 0 for holes). A schematic illustration of the Seebeck experimental setup is shown in Fig.2.12. The sample to be investigated is placed on top of two Peltier elements, which produce a temperature gradient $\Delta \mathrm{T} = T_1 - T_2$ across the sample. The temperature gradient is recorded by two thermocouples placed in contact with the electrodes. The thermoelectric potential V_{TH} of the order of a few mV/K and the temperature gradient ΔT of about 10-15 K are measured by using high-impedance voltmeters.

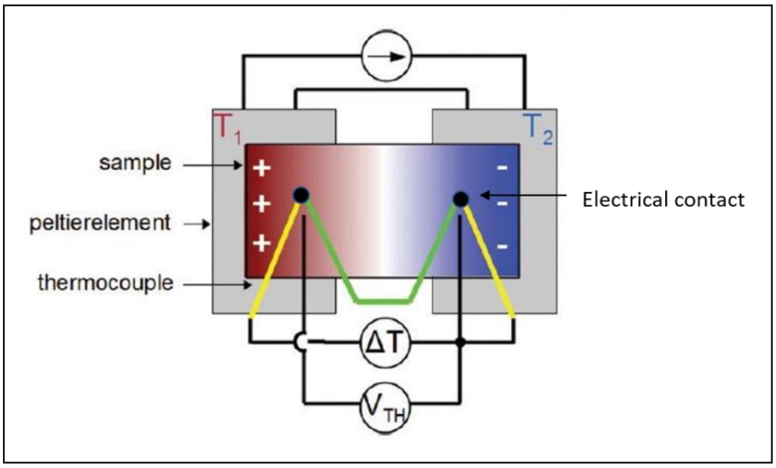

Fig.2.12 Schematic illustration of the experimental setup for Seebeck coefficient measurements [7].

References

[1] H. Sun, K. H. Li, C. T. Castanedo, S. Okur, G. S. Tompa, T. Salagaj, S. Lopatin, A. Genovese and X. Li, “HCl flow-induced phase change of α-, β-, and ε-Ga2O3 films grown by MOCVD,” *Crystal Growth & Design,* vol. 18, no. 4, pp. 2370-2376, 2018.

[2] Y. Yao, S. Okur, L. A. Lyle, G. S. Tompa, T. Salagaj, N. Sbrockey, R. Davis e L. M. Porter, «Growth and characterization of α-, β-, and ϵ-phases of Ga2O3 using MOCVD and HVPE techniques,» *Materials Research Letters,* vol. 6, n. 5, pp. 268-275, 2018.

[3] Y. Zhuo, Z. Chen, W. Tu, X. Ma, Y. Pei and G. Wang, “Control of the crystal phase composition of gallium oxide thin film prepared by metal-organic chemical vapor deposition,” *Applied Surface Science,* vol. 420, pp. 802-807, 2017.

[4] F. Boschi, M. Bosi, T. Berzina, E. Buffagni, C. Ferrari and R. Fornari, “Hetero-epitaxy of ε-Ga2O3 layers by MOCVD and ALD,” *Journal of Crystal Growth,* vol. 443, pp. 25-30, 2016.

[5] A. Baptista, F. Silva, J. Porteiro, J. Míguez and G. Pinto, “Sputtering physical vapour deposition (PVD) coatings: A critical review on process improvement and market trend demands,” *Coatings,* vol. 8, no. 11, p. 402, 2018.

[6] D. K. Schroder, Material and device - Semiconductor material and device. Third edition, Physics Today 44, 2006.

[7] N. Preissler, O. Bierwagen, A. T. Ramu and J. S. Speck, “Electrical transport, electrothermal transport, and effective electron mass in single-crystalline In2O3 films,” *Physical Review B,* vol. 88, no. 8, p. 085305, 2013.

Chapter 3 - Doping process and contacts for ε-Ga_2O_3 epilayers

3.1 Introduction

The control of the doping concentration has been the subject of extensive studies in the field of wide band gap materials. Gallium oxide, owing to the very wide energy gap, exhibits a very high intrinsic resistivity, therefore, doping is essential in order to modulate its electrical properties from insulator to conductive.

In literature, extensive investigations concerning the n-type doping of β-Ga_2O_3 are reported. It has been well established that elements belonging to the fourth group (Si, Ge, Sn) are active n-type dopants in β-polymorph, acting as substitutional dopants for Ga sites, where Si and Ge can replace the Ga atoms in the tetrahedral sites, and Sn prefers the octahedral Ga sites [1]. As reported in recent works [2, 3], they can be associated to shallow donor states. Si and Sn doping in β-Ga_2O_3 is performed during the growth by different methods [4, 5], providing net doping concentrations up to 10^{19} cm^{-3}. Such a doping limit being due to self-compensation phenomena. Concerning p-type conductivity in β-Ga_2O_3, although it has been theoretically predicted [6], ambiguous results of this type of conduction are provided up to date, making the achievement of hole conduction very questionable. Among them, calculations carried out by Varley *et al* [7] demonstrate that holes are self-trapped in the valence band, prohibiting a real p-type conductivity. A very low mobility detected also in ε-polymorph is in agreement with the calculations carried out by Mulazzi et *al.* [8] and Kim *et.al* [9] that showed a very flat valence band, and predicted a significantly high hole effective mass.

3.1.1 n-type doping of ε- Ga_2O_3 epilayers

In literature, up to now, few results are available concerning the n-type doping of ε-Ga_2O_3.

In recent works [10, 11], it was demonstrated that n-type ε-Ga_2O_3 epilayers, doped with Si and Sn, could be obtained through two different methods: by adding SiH_4 during the epitaxial growth, and by diffusing Sn in nominally undoped ε-Ga_2O_3 thin films.

The achievement of n-type doping of ε-Ga_2O_3 films by Sn thermal diffusion and the investigation of corresponding electronic transport mechanisms using van der Pauw method were main topics carried out during this PhD research activity.

The Sn-doping process is mainly divided in two steps: first a thin film of SnO_x (50 nm thick) is deposited on nominally undoped ε-Ga_2O_3 epilayer from a Sn metallic target, and then, the stacked layers are annealed at 600°C for 4 hours in vacuum to allow Sn diffusion into the Ga_2O_3 film. The residual SnO_x compound is finally removed from the film surface by etching in a solution (HF: HNO_3=50:50). The deposition was made by using a radio frequency (r.f.) reactive magnetron sputtering. In reactive sputtering, starting with a Sn metallic target and making the deposition in oxygen atmosphere, it is possible to obtain a Sn-based oxide layer.

Pure Sn deposition is not used because of formation of Sn drops on the ε-Ga_2O_3 surface at temperatures higher than the melting point of Sn (231.9 °C). By depositing a tin-rich oxide film $SnO_{(2-X)}$ with x<<1 it was possible to obtain the diffusion of Sn atoms from the $SnO_{(2-x)}$ to ε-Ga_2O_3 resulting in an effective n-type doping.

The correct $SnO_{(2-x)}$ stoichiometry was obtained by a careful control of various parameters into the sputtering chamber such as the process gas pressure (Ar), the reactive gas pressure (O_2), the sputtering power, and the SnO deposition rate.

In Fig.3.1 the deposition rate of the Sn-based oxide film is plotted as a function of the O_2 partial pressure ($P(O_2)$). As it is clearly visible in the picture, the deposition rate strongly depends on the $P(O_2)$, which plays a key role for the resulting SnO film. In particular, in a magnetron sputtering, the glow discharge tends to expand on the target surface for increasing oxygen pressure, but the current, which is related to the number of Ar ions striking the target surface, remains the same. In other words, the current density decreases with increasing oxygen pressure, resulting in a decrease of the sputter rate and deposition rate. Moreover, oxygen ions are characterized to have a much lower sputtering efficiency (Yield) than Argon ions and therefore a lower deposition rate is obtained.

Two different regions can be distinguished: the quasi-metallic SnO+Sn deposition regime at $P(O_2) < 2.5$ Pa, characterized by a high deposition rate (10 Å/s), and the stoichiometric SnO_2 deposition regime at $P(O_2) > 5$ Pa with very low deposition rate (0.4 Å/s). Both these regions are not appropriate to obtain the tin- rich $SnO_{(2-x)}$ film able to diffuse into the ε-Ga_2O_3 layer. The correct $SnO_{(2-x)}$ deposition condition was found to be between the two regions, where the $P(O_2)$ is in the range of $(3\div4)10^{-2}$ Pa.

This phenomenon could be explained taking into account the different Sn diffusion mechanism into the Ga_2O_3 layer. When $SnO_{(2-x)}$ oxide film is formed, the excess of Sn atoms in the $SnO_{(2-x)}$ is free to diffuse into the Ga_2O_3 layer, maintaining a stable composition of the Ga_2O_3 epitaxial layer surface and of the sputtered capping layer (Fig.3.1c). Conversely, in case of quasi-metallic SnO+Sn film, oxygen atoms migrate from the Ga_2O_3 layer to the capping layer upon thermal treatment, forming SnO_2 inclusions in the upper layer. It should be point out that SnO is a themodynamically unstable phase and tends to transform in SnO_2 in the presence of oxygen. As a matter of fact, such a transformation is justified taking into account the difference in the enthalpies of formation between SnO_2 (ΔH_{0f} = -577 $kJmol^{-1}$) and SnO (ΔH_{0f} = -281 $kJmol^{-1}$). At the same time, the Ga atoms made free at the Ga_2O_3 interface, in turn, induce the formation of a mixed ternary layer $SnGaO_x$ (Fig.3.1 b). The latter seems to act as a buffer layer, preventing the whole Sn diffusion into the Ga_2O_3.

The effective Sn-diffusion inside the ε-Ga_2O_3 has been confirmed by different characterization techniques, as it will be shown in the next paragraph.

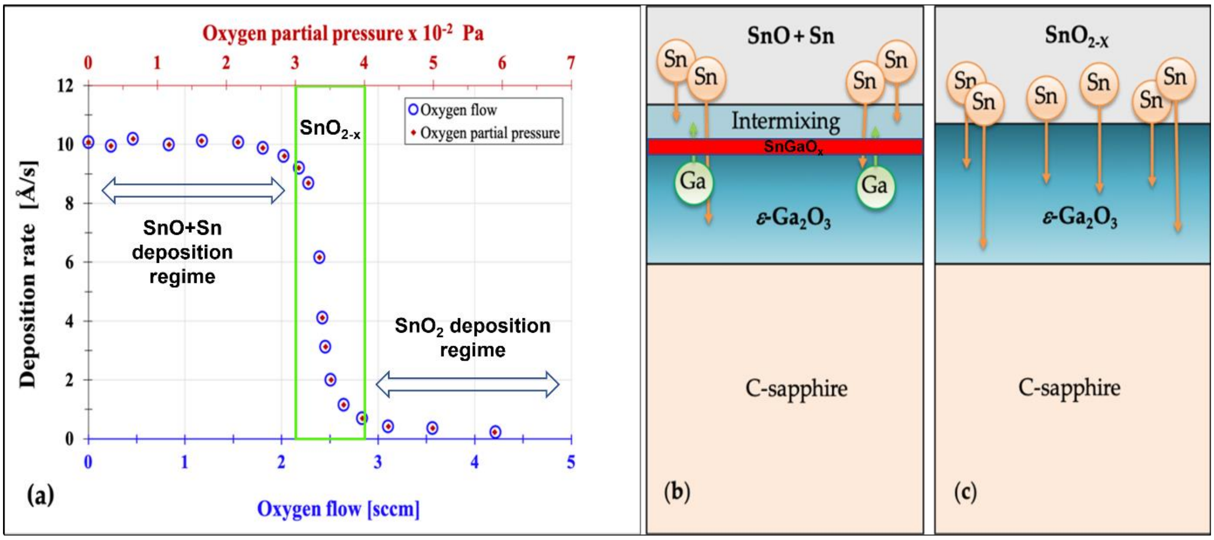

Fig.3.1 (a) Plot of the SnO deposition rate as a function of the oxygen partial pressure (or Oxygen flow). Solid green rectangle denotes the appropriate working window of P(O_2). (b) and (c) drawing of the ε-Ga_2O_3 epilayer covered by SnO+Sn and $SnO_{(2-X)}$ film, respectively. In (b) the formation of a mixed layer ($SnGaO_x$) at the interface, which inhibits the further diffusion of Sn atoms into ε -Ga_2O_3, is highlighted [11].

3.1.2 ToF-SIMS, Raman and RBS investigations

ToF-SIMS, Raman and RBS analysis were carried out in cooperation with internal and external research groups in order to confirm the effective incorporation of Sn inside the ε-Ga_2O_3. Such measurements are not a direct part of the present PhD research activity, however, a brief outline is given to have a more complete picture of the Sn doping process in ε-Ga_2O_3.

Time of Flight-Secondary Ion Mass Spectroscopy (ToF-SIMS) is a sensitive analytical technique that provides detailed information about the composition of thin films and surfaces by using a focused ion beam source to sputter the sample surface and analyzing the emission of secondary ions. ToF-SIMS measurements have been performed at IMM-CNR Agrate Unit, Milan. ToF-SIMS profiles were acquired by using an ION-TOF IV instrument (ION-TOF GmbH) equipped with two ion sources: Cs^+ ions and Ga^+ ions with energy of 2 keV and 25 keV, respectively. Secondary ions were collected in negative bias and normalized to the signal of Al sapphire substrate. Further details on the experimental setup are described in ref. [12].

The Fig.3.2 shows ToF-SIMS profiles of Sn-doped ε- Ga_2O_3 layer, where the ^{116}Sn and ^{120}Sn isotopes are detected, confirming a clear incorporation of Sn in the ε-Ga_2O_3 film.

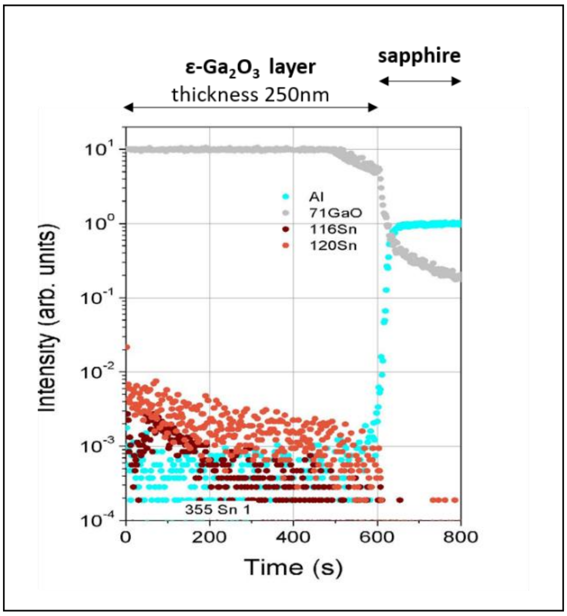

Fig.3.2 ToF-SIMS profiles of ^{116}Sn and ^{120}Sn isotopes (brown and orange circles, respectively) along with Ga-O (grey circles) and Al (blue circles) species [11].

It is important to point out that ToF-SIMS is a useful technique to have information about the incorporation of doping impurities inside ε- Ga_2O_3 the layer, however, it is not able to provide a quantitative analysis about the chemical composition of the introduced impurities. For this reason, further investigations were carried out by Raman and Rutherford backscattering (RBS) spectroscopy techniques to learn the related chemical composition of the Sn-doped ε- Ga_2O_3 film.

Raman spectra were acquired with a HORIBA-Jobin Yvon LabRam confocal microspectrometer by using the 473.1 nm line emission of a doubled Nd:YAG diode laser supplied with an integrated Olympus BX40 microscope. The LabSpec 5 built-in software was used for data analysis.

Raman investigation was performed on Sn-doped ε-Ga_2O_3 layers in different oxygen partial pressures. In the first case, using $P(O_2) < 3.5\cdot10^{-2}$ Pa, Raman spectrum (Fig.3.3a) shows the peak of SnO at 210 cm^{-1}, together with contribution of Al_2O_3 substrate, reasonably associated to the formation of the Sn+SnO film. On the contrary, when $P(O_2) = 3.5 \cdot 10^{-2}$ Pa is used, the presence of SnO_2 peaks in the Raman spectrum are evident (Fig.3.3b), which are associated to the $SnO_{(2-x)}$ film. Sn-excess or O-deficiency in spectra (Fig.3.3a) and (Fig.3.3b), respectively, is below the detection threshold of the instrumentation.

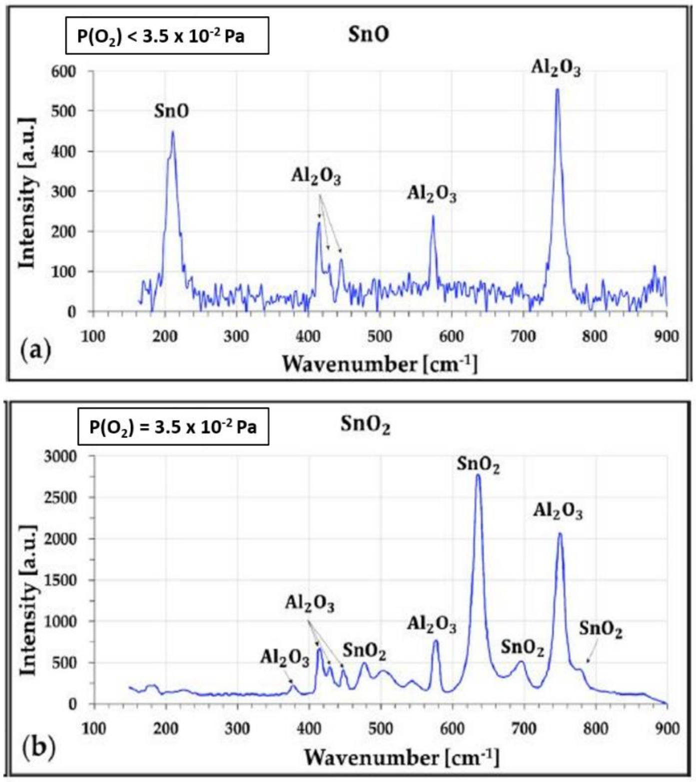

Fig.3.3 Raman spectra of Sn-based oxide films deposited in different oxygen partial pressures. (a) SnO+Sn doping film is obtained using $P(O_2) < 3.5 \cdot 10^{-2}$ Pa. (b) When $P(O_2) = 3.5 \cdot 10^{-2}$ Pa the deposition of a $SnO_{(2-x)}$ film is achieved [11].

Unluckily, Raman measurements are not able to provide detailed information about the SnO layer composition, i.e., the amount of Sn-excess or O_2 deficiency into the Sn-based oxide film. More detailed investigations concerning the chemical composition of Sn-based oxide film on Ga_2O_3 layer were performed by RBS technique, which provide a reliable interpretation of Sn diffusion process in the ε-Ga_2O_3 layer. RBS measurements were carried out in cooperation with the Institute for Technical Physics and Material Science of Budapest.

RBS spectra were acquired by using a 2 MeV $4He^+$ ion beam and an ORTEC detector assembled in Cornell geometry at a scattering angle of $\Theta = 165^0$ to record the backstattered He^+ ions.

The measured RBS spectra were assessed with the SIMNRA simulation code [13], as shown in Figs.3.4. The first simulation was performed on the (Sn+SnO) film (Fig.3.4a), considering the smooth SnO_x layer (44 nm thick) and the formation of intermixing layer $SnGaO_x$ at the interface. The second analysis (Fig.3.4b) was carried out on the tin rich $SnO_{(2-x)}$ layer, assuming the formation of a smooth SnO_2 layer (thickness of about 65 nm), without any presence of $SnGaO_x$ layer at the SnO/Ga_2O_3 interface. As it is clearly visible in the graphs, the simulation data show a good agreement with the experimental points.

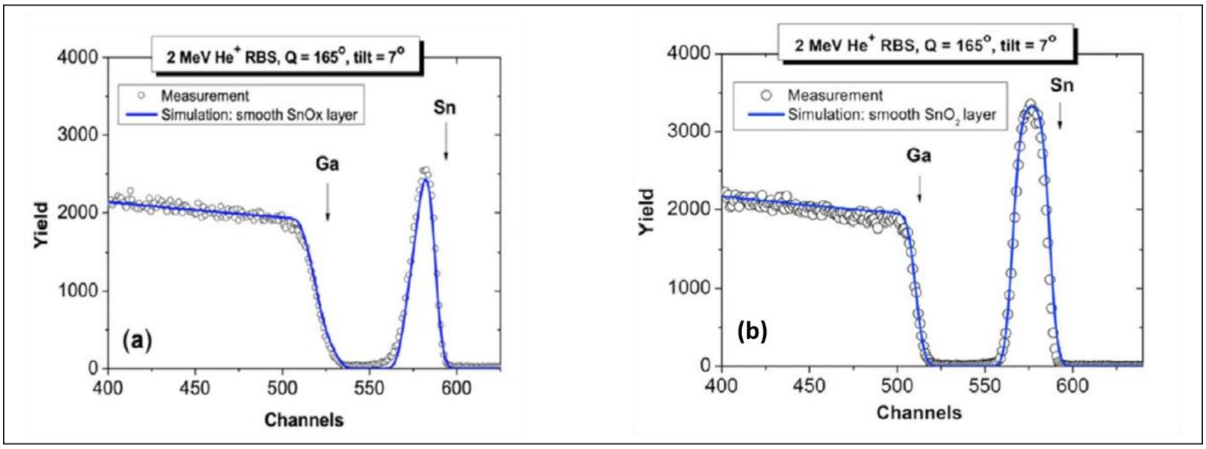

Fig.3.4 RBS measurements taken at a 7° tilt angle of the sample. The spectrum edges of the Ga and Sn components are indicated by the arrows. The blue line corresponds to the fitting by SIMNRA simulations considering: (a) a smooth SnO_x oxide layer and the intermixing Sn-Ga-O layer at the SnO/Ga_2O_3 interface, (b) no intermixing and uniform $SnO_{(2-x)}$ as capping layer [11].

3.1.3 Electrical characterization

In this section electrical characterization of Sn-doped ε-Ga_2O_3 samples will be presented. Resistivity measurements at different temperatures (from 293 K to 15 K), in vacuum and dark conditions, have been performed by using four contacts in van der Pauw configuration. The main processing parameters and the resistivity values and room temperature (RT) of the tested samples are shown in Tab.3.1. The resistivity curve as a function of T (see Fig.3.5) shows a trend consistent with Mott law (Eq 3.1). This means that the main contribution to electrical conductivity comes from electron hopping between localized states around the Fermi level rather than from free electrons in the extended states [14]. The Mott law can be expressed as follows:

$$\rho(T) = \rho_0 \exp\left[\left(\frac{T_0}{T}\right)^{1/4}\right] \tag{3. 1}$$

where ρ_0 takes the meaning of the infinite temperature resistivity (assumed temperature independent in the Mott law), and T_0 is defined as:

$$T_0 = \frac{C}{\xi^3 g(\mu) K_B} \tag{3. 2}$$

with K_B the Boltzmann constant, $g(\mu)$ the density of the energy states around the Fermi level (assumed constant in the case of non-interacting electron gas). ξ is the localization radius, reasonably taken of the order of the nanometers. The constant C is a dimensionless parameter that depends on the network of hopping sites assumed in the model ($C = 18.1$ for 3D non-interacting carriers) [14, 15].

Linear trends are found in the "Mott plot" (see Fig.3.5) defined as the plot of $(ln\rho$ vs $T^{-1/4})$ and expressed by:

$$ln\rho(T) = ln\rho_0 + \left(\frac{T_0}{T}\right)^{1/4} \tag{3. 3}$$

where $(T_0)^{1/4}$ represents the slope of the curves.

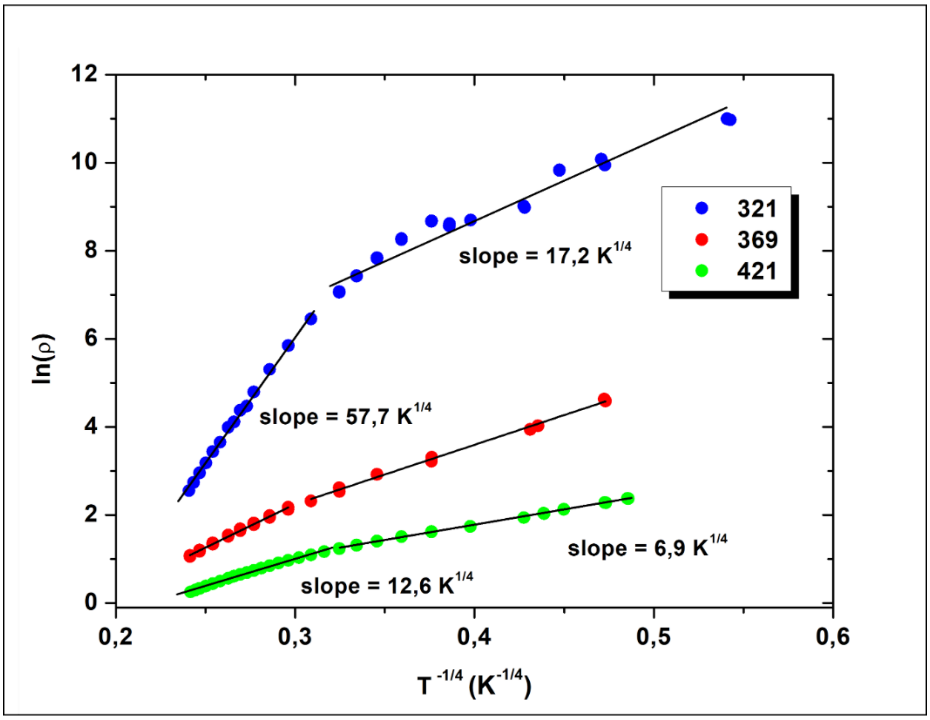

Fig.3.5 Natural logarithm of the resistivity data (in Ωcm) vs. $T^{-1/4}$ (Mott plot) of the investigated samples. In the figure the slopes of the linear traits are indicated, obtained from a linear fit of the ln(ρ) data vs. $T^{-1/4}$.

Tab.3.1 Main processing parameters and electrical data at RT of some Sn-doped investigated samples.

Sample	MOVPE growth T (°C)	Ga_2O_3 thickness (nm)	Post-sputtering annealing time (min)	RT resistivity (Ωcm)	RT carrier concentration (cm^{-3})	RT Hall mobility (cm^2/Vs)
#421Sn2	610	270	240	1.3	2.4 x 10^{18}	1.4
#369-E6	610	280	240	2.8	not. meas.	not. meas
#321-D6	600	310	120	12.8	2 x 10^{17}	2.4

The Mott theory is based on the assumption that electrons are in localized states into the bandgap, with energies in proximity of the Fermi level (Fig.3.6).

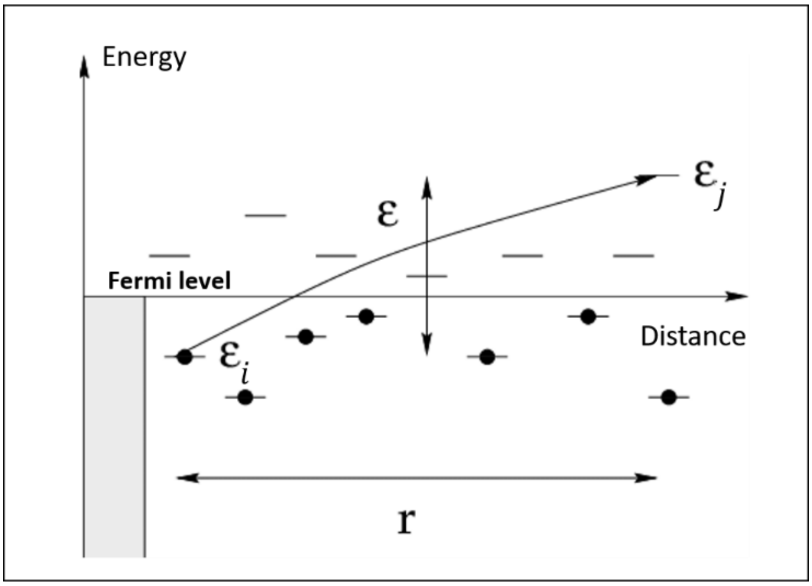

Fig.3.6 Schematic of the hopping process between localized states around the Fermi level.

The “hopping” probability for an electron to jump from an occupied site *i* to an empty one *j* can be defined as:

$$\upsilon_{ij} = \exp\,(-2\alpha R_{ij} - \frac{\omega_{ij}}{KT}) \qquad (3.\ 4)$$

where R_{ij} indicates the distance among the two sites, ω_{ij} represents the energy separation between the two states, and $\frac{1}{\alpha}$ is the localization length.

The maximum value of ν_{ij} is obtained when the argument of exponential is minimum, which corresponds to the highest conduction contribution. When the second term in the argument of the exponential is negligible with respect the first one, the highest hopping probability is obtained by minimizing the hopping length, and the conduction mechanism takes a thermally activated character (linear trend in Arrhenius plot), known as nearest neighbour hopping. However, at temperature low enough or also at any temperature in disordered materials, both the terms contribute effectively to the hopping probability, and must be considered in maximizing υ_{ij}. In this case, the so-called Variable-Range-Hopping (VRH) transport mechanism occurs in the semiconductor layer.

The number of sites N_{ij} involved in the hopping process, separated by a distance R_{ij} and energy ω_{ij}, can be expressed by:

$$N_{ij} = g(\mu)\omega_{ij} = \frac{1}{\frac{4}{3}\pi R_{ij}^3} \qquad (3.\ 5)$$

Replacing the (3.5) in (3.4), reducing at minimum the exponential argument, the optimal length R_{opt} can be obtained:

$$R_{opt} = \frac{3}{8\alpha}(\frac{T_0}{T})^{\frac{1}{4}} \qquad (3.\ 6)$$

thus, the optimal energy ω_{opt} is achieved by replacing the relation R_{opt} into the N_{ij}

$$\omega_{opt} = 0.25 K_B T (T/T_0)^{1/4} = 0.25\, K_B T^{3/4} \times slope \tag{3. 7}$$

In the VRH regime the R_{opt} represents the temperature-dependent average distance among the sites that takes place to the hopping transport, while ω_{opt} denotes the activation energy of carriers involved in the hopping process.

The characteristic plots of the investigated ε-Ga_2O_3 samples shown in Fig.3.5 exhibit two different slopes, which are probably related to two different hopping mechanisms, each one dominating in a typical temperature range. Such a trend was observed in all investigated samples.

The samples data were investigated in the corresponding conduction regimes by using the Eq. (3.1). The most resistive sample (#321-D6) presented slopes of 17.2 ± 0.4 $K^{1/4}$ in the low temperature (LT) regime and 57.7 ± 0.2 $K^{1/4}$ in high temperature (HT) regime. For the most conductive sample (#421 Sn2) slopes have values of 6.9 ± 0.2 $K^{1/4}$ and 12.6 ± 0.1 $K^{1/4}$ in LT and HT temperature regime, respectively. It is important to underline that the most conductive sample is characterized by lower slopes, then a higher density of the states at the Fermi energy, $g(\mu)$. This is consistent with a higher doping level, supporting the assertion that the hopping sites are identified as the donor impurities or their complexes.

From the slopes of the linear segments in the plots of Fig.3.5 the density of sites (N_μ) involved in the hopping process, can be derived at fixed temperatures:

$$N_\mu = \omega_{opt}\ g(\mu) \tag{3. 8}$$

A value N_μ = (3.5 - 6.2) × 10^{18} cm^{-3} was obtained for the sample #421 Sn2 in LT and HT temperature regimes, respectively.

Assuming the carrier hop between donors (or their complexes), the density of sites N_μ is expected to be of the same order of magnitude of the donor density. Then it could be well related to the RT carrier concentration n (comparable to the net donor density) detected by Hall measurements. The Hall density of the sample #421 Sn2 reported in Tab.3.1 results to be slightly lower than the density of localized sites so evaluated, which is quite reasonable since the hopping process occurs if the concentration of free sites is higher than the carrier density (owing to compensation).

3.2 Main concepts on metal/semiconductor contact

Metal/semiconductor contact is considered the essential part of any electronic device, and its physical properties have a significant influence on the total device features. Metal/semiconductor structures are commonly divided into two categories: the ohmic and the Schottky (rectifying) contacts. An ohmic contact provides linear and symmetric current-voltage (I-V) characteristic and a negligible contact resistance compared to that of the semiconductor is also desired. On the contrary, Schottky contact has a not-linear and asymmetric (I-V) profile, due to the presence of a potential barrier (Schottky barrier) at the metal/semiconductor interface. The most important parameter related to the metal/semiconductor contact, which determined the electrical behavior of the contact (i.e., Schottky or Ohmic), is the Schottky barrier height ($q\phi_B$). According to the Schottky-Mott theory [16], for a n-type doped semiconductor it is defined as:

$$q\phi_B = q(\phi_m - \chi_s) \tag{3. 9}$$

where $q\phi_m$ is the metal work function and $q\chi_s$ is the semiconductor electron affinity.
Basically, if the metal work function ($q\phi_m$) is greater than the semiconductor work function ($q\phi_s$) a Schottky contact is formed (Fig.3.7).

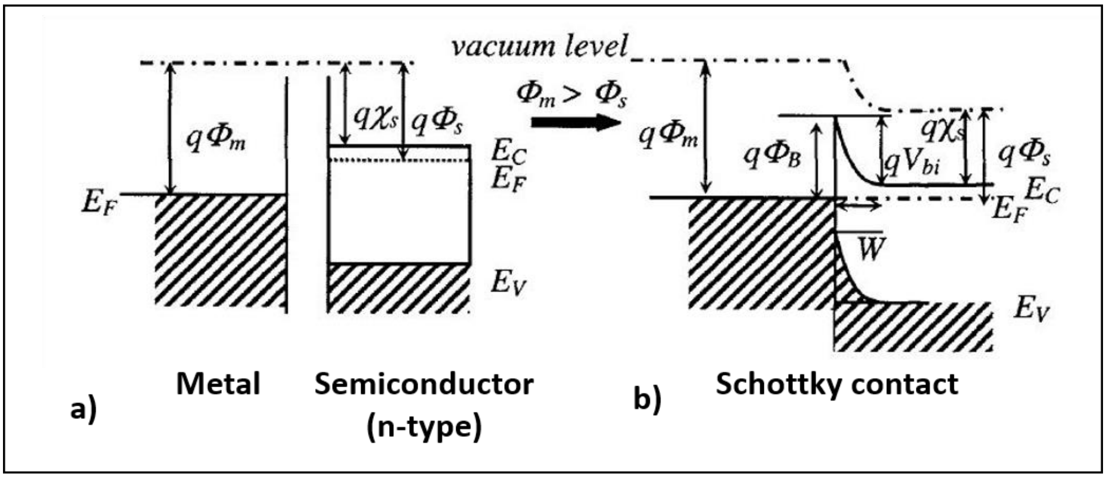

Fig.3.7 Energy band diagram of a metal and n-type semiconductor before (a) and after (b) they are put in contact. ($\phi_m > \phi_s$). E_F is the Fermi level, E_V and E_C are the valence and conduction band of the semiconductor, respectively. W is the depletion width inside the semiconductor [17].

The typical transport mechanism for mildly doped semiconductors (n < 10^{17}cm^{-3}) is ruled by the Schottky or thermionic emission (TE). In this case, by applying an electric field, the electrons have sufficient thermal energy to overcome the Schottky barrier from the semiconductor to the metal.

The formation of an ohmic contact takes place if the metal work function ($q\phi_m$) is lower than or equal to the work function of the semiconductor ($q\chi_s$), see Fig.3.8. Under this condition, the electrons can freely move in both directions without encountering any contact barrier. Nevertheless, it is not easy to find metals that satisfy the condition $q\phi_m < q\chi_s$, especially for wide bandgap semiconductors like Ga_2O_3. The typical strategy to overcome the problem is to produce a highly-doped (n > 10^{19} cm^{-3}) thin layer within the material to be measured, which in turn induces a reduction of the depletion width W. In this situation, electrons may cross the thin barrier by tunnelling (Fig.3.8c). Such electronic transport is ruled by the field emission (FE) mechanism.

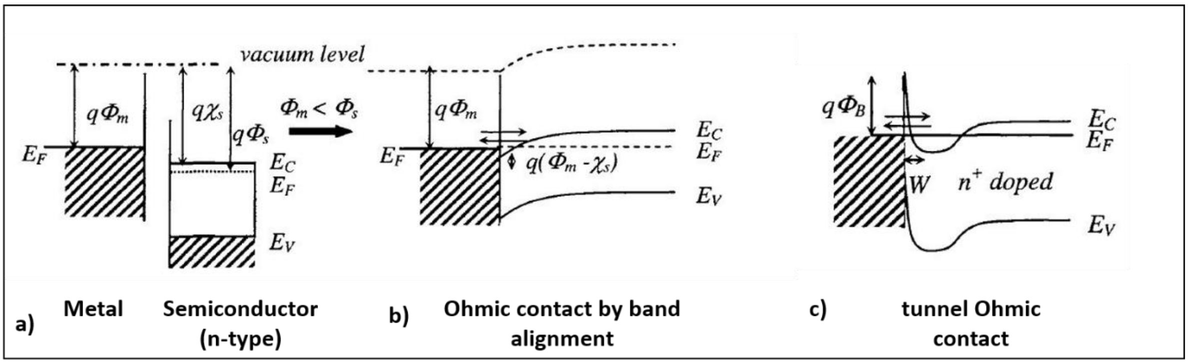

Fig.3.8 Energy band diagram of a metal and n-type semiconductor ($\phi_m < \phi_s$) before (a) and after (b) they are put in contact. Metal-semiconductor (n-type) contact in the case of heavy doping (c) [17].

An intermediate transport mechanism across the contact barrier, which occurs for doping levels in the range of 10^{17} - 10^{19} cm^{-3}, is the thermionic field emission (TFE). In this case, carriers do not have sufficient thermal energy to overcome the barrier, but their energy (sum of thermal and field contributions) is sufficient to overcome the barrier by tunnelling.

A schematic comparison between the thermionic emission, thermionic-field emission and field emission is shown in Fig.3.9 considering a negative bias applied to the metal with respect to the semiconductor.

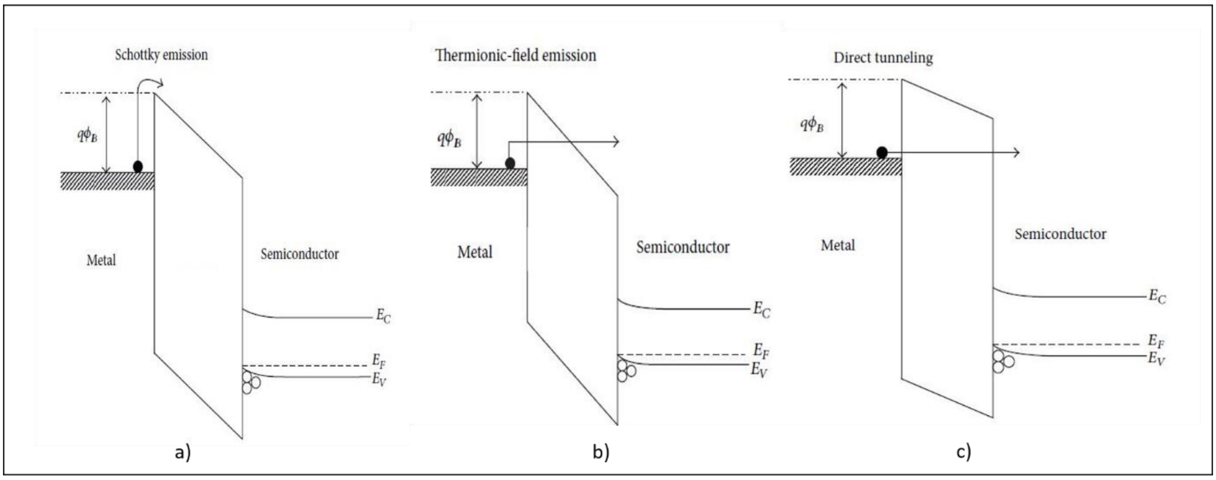

Fig.3.9 Schematic illustration of the energy band diagram referred to thermionic emission (a), thermionic-field emission (b) and field emission (c) [18].

3.2.1 Ohmic contacts for undoped ε-Ga_2O_3 layers

The fabrication of good Ohmic contacts represents a real challenge in wide bandgap semiconductors technology. A useful parameter used to define the quality of Ohmic contact is the specific contact resistance (ρ_c), which is independent of the contact geometry, and measured in Ωcm^2. Basically, Ohmic contacts with low specific contact resistance are required to avoid overheating effects and power losses in any electronic devices, which decrease the overall device efficiency.

Different structures have been intensively investigated to achieve ohmic contacts on β-Ga_2O_3 [19]. Most of the contact structures shown to date use a Ti interfacial layer with additional Au or Al capping layers to avoid oxidation of the underlying metal. Moreover, in many studies post-metallization rapid thermal treatments at high temperature (400 °C – 500 °C) in controlled environments or local doping process via ion implantation have been attempted to improve the contact quality [20].

Conversely, in literature little information is available about the development of ohmic contacts on ε-Ga_2O_3 thin films and the following results can be considered as the first thorough investigation of ohmic contacts on this polymorph [21].

Several materials were deposited by sputtering in order to obtain good ohmic contacts on nominally undoped ε-Ga_2O_3 thin layers. In the first investigation, ZnO/ITO/Au structure was used but electrical measurements showed poor linearity in I-V characteristic, due to probable Au diffusion into ε-Ga_2O_3 layers after annealing treatments. Successively, ITO/Pt contact was tested, but non-linear I-V characteristics were obtained, probably related to the formation of PtO_x into the ITO structure, which rises the surface work function of the ITO layer, and then increases the contact barrier of ITO/Ga_2O_3.

SnO_x /ITO stacked layers seems to be a viable method to achieve ohmic contact on the ε-Ga_2O_3 layers. It is important to highlight that the SnO_x deposition process was carried out applying the same procedure, except the sample heating, used to obtain n-type doping of ε-Ga_2O_3 films by Sn diffusion, described in depth in the previous section.

In the following, the experimental results obtained by using SnO_x /ITO system are resented.

Highly resistive ε - Ga_2O_3 epilayers were grown by Metal Organic Chemical Vapour Deposition (MOCVD) on 2’’ c-oriented Al_2O_3 substrates. The 2’’ slices were cut in pieces of area (1 × 0.5) cm^2 and then, in order to eliminate surface contaminants, were cleaned with a solution of HF (50%) and HNO_3 (50%) and then by organic solvents (acetone, isopropanol).

Planar electrodes were fabricated through a stencil metal mask by sputter deposition of SnO_x+ITO bilayers (100 nm and 1000 nm thick, respectively) on top of ε-Ga_2O_3 layers. The contacts are spaced by increasing distances of L_1= 0.2 mm, L_1= 0.4 mm, L_1= 0.8 mm, L_1= 1.6 mm, as shown in Fig.3.10.

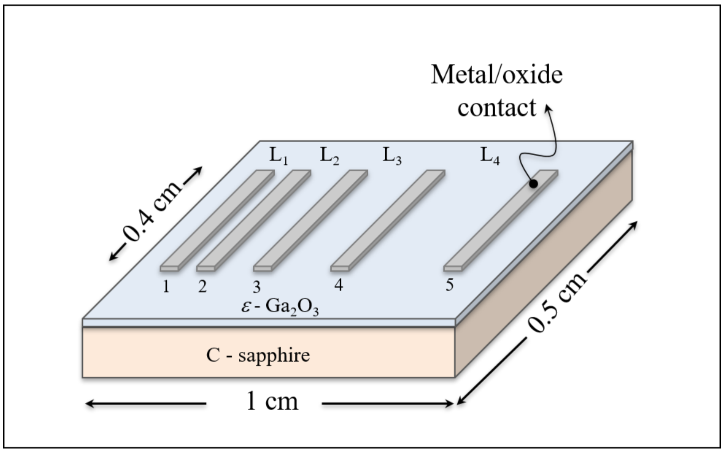

Fig.3.10 Schematic illustration of a test structure used for Current-Voltage (I-V) measurements [21].

The current-voltage (I-V) characteristics were acquired at RT and in dark condition applying voltages in the range (0÷200 V) by using a Keithley Source-Meter Mod.2400.

The first I-V measurements performed in sequence on the 2-3, 3-4, and 4-5 pairs shows good linearity, as reported in Fig.3.11. However, the slope of each curve, which is related to the resistance of the material, do not match to the distance between the contact pairs. Such a behaviour could be associated to space charge effects at the contact region. In particular, being an highly resistive material the flowing current is very low, therefore the adjustment of spatial charge at the contact region is very slow. In this condition, each I-V measurement is affected by the previous one, e.g. the first I-V measurement on contact 2-3 affects the 3-4 measurement, since contact 3 acts as a shared electrode. In other words, the system did not reach the steady-state condition.

Such an effect can be avoided by performing singular I-V measurements on three different pieces of the same ε-Ga_2O_3 film (422Ud a, b, c), as shown in Fig.3.11b. In “422Ud a” the 2-3 pair is connected, while in “422Ud b” and “422Ud c” the 3-4 and 4-5 pairs are connected, respectively. The stationary condition is reached by applying for a few minutes a bias of 200 V to the contact pairs before starting the voltage cycles (0 ± 200 V).

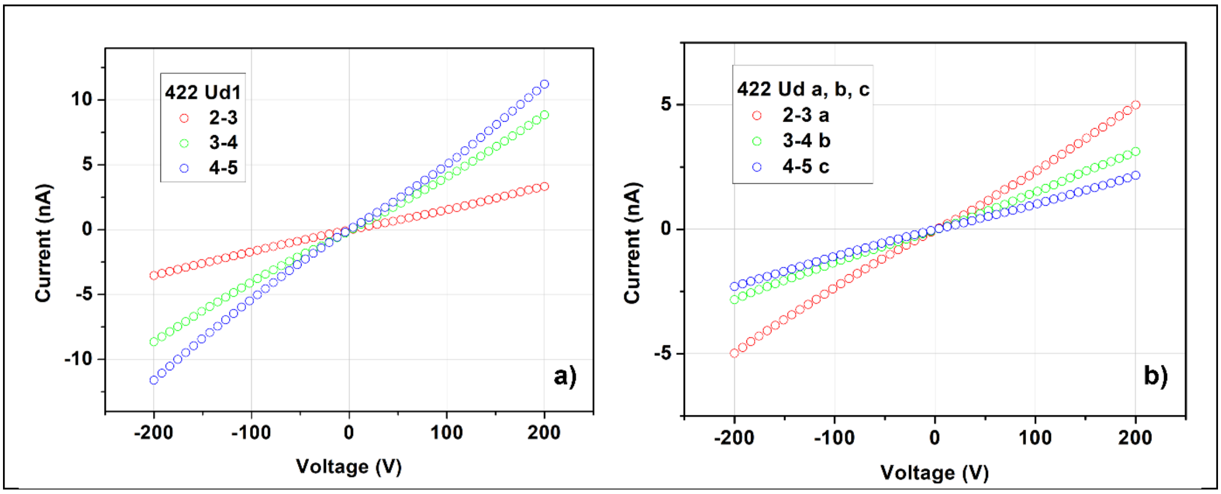

Fig.3.11 I-V characteristics related to the 2-3, 3-4, 4-5 contact pairs. (a) I-V characteristics performed on sample #422Ud1 in non-stationary conditions. (b) I-V profiles related to three pieces of the same film (#422Ud1): in “422Ud a” the 2-3 pair is connected, while in “422Ud b” and “422Ud c” the 3-4 and 4-5 pairs are connected, respectively [21].

However, non-linear behaviour was observed in the I-V characteristic of the 1-2 pair measured in stationary condition (Fig.3.12). Linear trend is found by plotting (Log I vs $V^{1/2}$), suggesting that the conduction mechanism is ruled by a Schottky or thermionic emission:

$$I \propto T^2 \cdot \exp\left(a \frac{\sqrt{V}}{k_B T} - q \frac{\Phi_B}{k_B T}\right) \tag{3. 10}$$

where, T is the absolute temperature, V is the applied voltage, Φ_B the barrier height, k_B the Boltzmann constant and a is a constant which depends on the relative permittivity of the material and on the layer thickness.

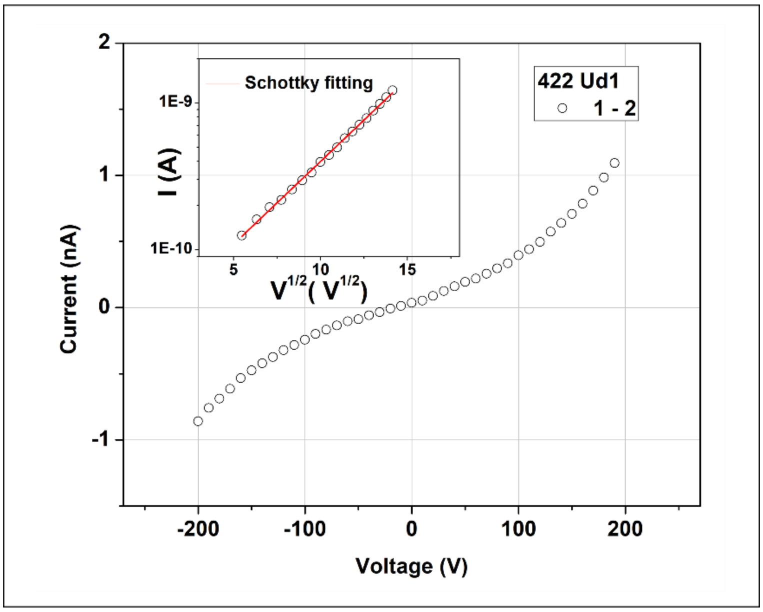

Fig.3.12 I-V curve recorded between the contact pair 1-2 in stationary conditions (sample #422Ud1). The inset reports the Schottky fitting by plotting (Log I vs $V^{1/2}$) in a range from 10 V to 200 V. Current values lower than 0.1 nA are below the sensibility of the Keithley Source-Meter. [21].

Non-linear behaviour of the 1-2 pair with respect to the other pairs could be explained taking into account the following considerations: *(i)* the voltage drop distribution between contact couples and *(ii)* the formation of Sn-doped thin layer at the SnO_x / ε-Ga_2O_3 interface, acting as a contact barrier. A schematic illustration is reported in Fig.3.13. Such Sn-doped interfacial layer, promoted by the SnO_x sputtering deposition, was confirmed by RBS investigations as described in the previous section.

The total voltage drop V applied to one contact pair can be defined as $V = V_{Ci} + V_S + V_{Cj}$, where V_{Ci} and V_{Cj} are the drops on the contact i and j, respectively, and V_S is the voltage drop on the semiconductor. As well known, the voltage drop corresponds to a total resistance, defined as $R = R_{Ci} + R_{SEM} + R_{Cj}$. Considering the 1-2 pair, most of the voltage drops on the metal/semiconductor contact and just a low voltage falls on semiconductor resistance R_{SEM}, i.e. $R_{Ci}, R_{Cj} \gg R_{SEM}$, which means that the role of the contacts is dominant. In such a condition, electrons, limited by the high resistance of the semiconductor, tend to accumulate at the SnO_x / ε-Ga_2O_3 interface and may contribute to the conduction across the contact barrier, describing a Schottky-thermionic emission.

Conversely, for more spaced contact pairs (2-3, 3-4, 4-5) the following condition is soon reached: $R_{SEM} \gg R_{Ci}, R_{Cj}$, which suggests that the contribution of contact resistances is not dominant over the semiconductor resistance. In this situation, electrons may cross the contact barrier by a direct tunneling mechanism, corresponding to an ohmic behavior (Fig.3.11).

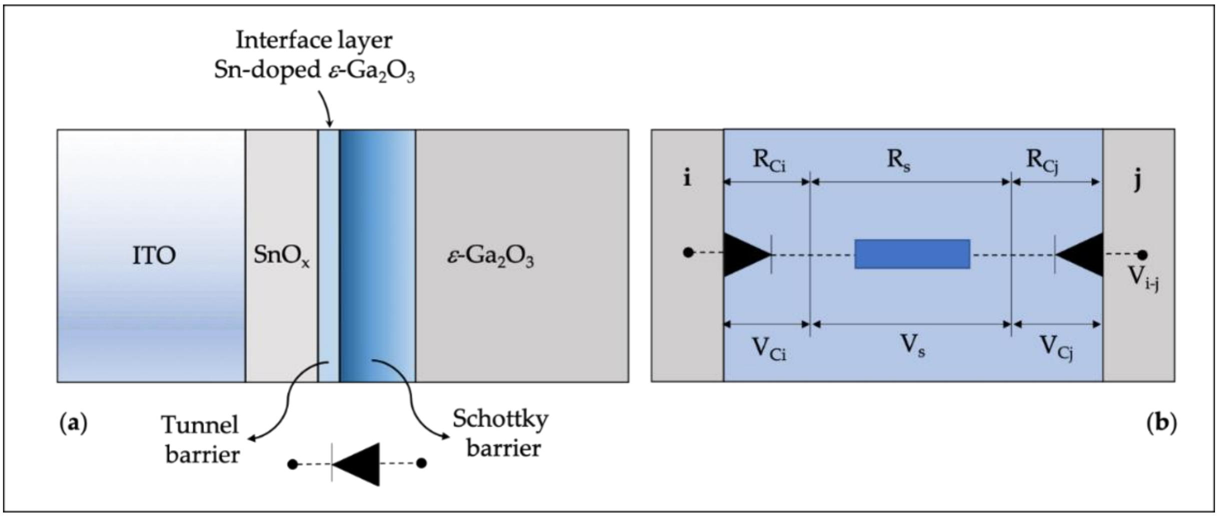

Fig.3.13 (a) Schematic illustration of the ITO/SnO_x stacked layers on top of ε-Ga_2O_3 and the formation of the contact barrier at the SnO_x / ε-Ga_2O_3 interface. (b) Schematic diagram of voltage drop distribution between one contact pair i-j [21]

Tab.3.2 Main parameters of the investigated Ga_2O_3 samples. RT resistance is calculated from the slope of the I-V curve performed on 4-5 pair. Resistivity is calculated from the resistance taking into account the geometrical factors [21].

Sample	Ga_2O_3 thickness (nm)	Contact layers	RT resistance (4-5 pair) (Ω)	RT resistivity (Ω·cm)	Conduction model (1-2 pair)
#422 Ud1	290	SnO_x + ITO	4×10^{10}	10^7	Schottky barrier
#475 Ud1	670	SnO_x + ITO	5×10^9	10^6	P-F
#483 Ud1	930	SnO_x + ITO	4×10^{11}	10^8	TF-SCLC

Moreover, I-V profiles related to the 1-2 pair of other undoped ε-Ga_2O_3 samples, grown in different conditions, show different trends compared to the Schottky emission. In particular, in some cases, the I-V curves show a trend consistent with space-charge limited current (SCLC) or Pool-Frenkel (P-F) models [22, 23].

The basic physical properties and related conduction models of the investigated samples (1-2 pair) are reported in Tab.3.2.

SCLC mechanism occurs in semiconductors with low mobility when the injected charge density is higher than the intrinsic carrier concentration of the semiconductor. The I-V characteristic follows a power law behaviour $I \propto V^m$ with $m \geq 2$. By plotting Log I v.s Log V, it is possible to obtain the exponent m, which corresponds to different transport mechanisms. For $m = 2$ a trap free regime (TF-SCLC) occurs, while in the case of $m > 2$ exponentially distributed traps regime (EDT-SCLC) takes place. For the sample #483 Ud1 $m = 2.04$ was obtained, confirming TF-SCLC mechanism (Fig.3.14a).

On the other hand, in P-F emission electrons trapped in localized states can move in the conduction band thanks to thermal fluctuations, increased by electric field. Such a model can be described by:

$$I \propto V \cdot exp(\frac{\beta\sqrt{V}-\phi}{K_B T}) \tag{3. 11}$$

where, ϕ is the barrier height of the trap and β is a coefficient related to the relative permittivity ε_r. The experimental data of the sample #475 Ud1, plotted in Log (I/V) v.s Log $V^{1/2}$ scale, show a good agreement with the P-F model, as reported in the inset of Fig.3.14b.

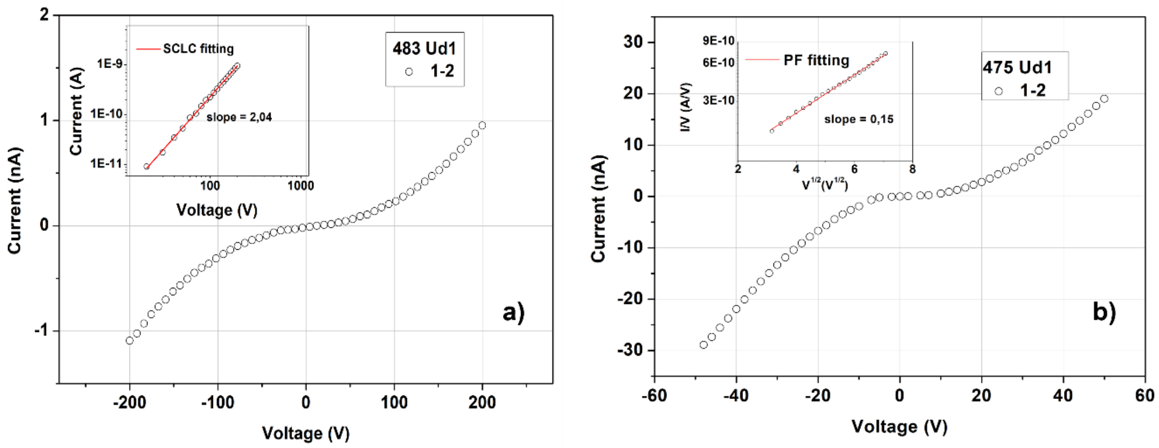

Fig.3.14 I-V profiles recorded between contact pair 1-2 in stationary conditions. (a) sample #483 Ud1. In the inset the experimental data (10 V - 200 V) reported in Log I v.s Log V scale show a SCLC conduction. (b) sample #475Ud1. In the inset, the experimental data (10 V - 50 V) show a trend consistent with Pool-Frenkel model [21].

To summarize, three different conduction models could be justified the non-linear behaviour of I-V characteristics related to the 1-2 pair: the Schottky-thermionic and the TF-SCLC regimes where trapping effects are excluded, and the P-F model characterized by a trap-assisted electron transport. These different conduction mechanisms observed in our samples could probably related to defects and/or surface states at the Ga_2O_3 /SnO_x interface due to the different growth conditions of the Ga_2O_3 layers. However, the physical reason behind these conduction processes is still unknown and requires further investigations in order to be correctly interpreted.

3.2.2 Ohmic contacts for n-type doped ε-Ga_2O_3 layers

Electrical characterization of ε-Ga_2O_3 samples doped with Sn and Si has been performed using Transfer Length Method (TLM) method. Such a technique permits to determine the specific contact resistance (ρ_c) associated to the metal-semiconductor contact, which is a useful quantity used to define the quality of Ohmic contact. The method requires the preparation of a series of metal-semiconductor contacts separated by increasing distance. Probes are applied to pairs of adjacent contacts and the resistance between them is measured by applying a voltage across the contacts and measuring the resulting current. Linear and symmetric I-V characteristics for all the contact pairs are strictly required for this method. Other details about the TLM method are reported in Chapter 2.

For this investigation SnO_x /ITO and Ti/Au stacked layers are used as electrical contacts.

Non-linearity of the I-V characteristics and/or non-equivalent contact resistances limited the reliable applicability of the method in nominally undoped ε - Ga_2O_3 samples. They could be due to interface charges trapping or to a sample charge effect during the measurement and need more investigation in order to be correctly interpreted.

For this reason, this method has been applied only for conductive ε-Ga_2O_3 layers. The I-V measurements and the R-L profiles relative to the Sn-doped sample (#483 Sn5) and Si-doped sample (#564.3 Si) are reported in Figs.3.15, 3.16.

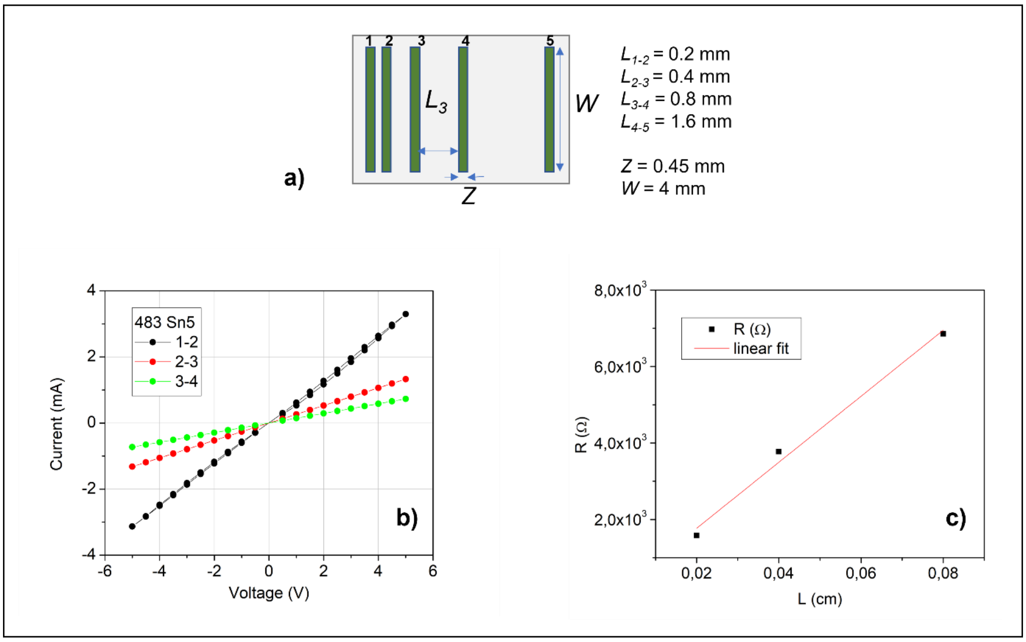

Fig.3.15 (a) Linear TLM contact pattern, (b) I-V characteristics measured on 1-2, 2-3, 3-4 contact pairs, and (c) R-L profile for Sn-doped ε - Ga_2O_3 sample (SnO_x/ITO contacts).

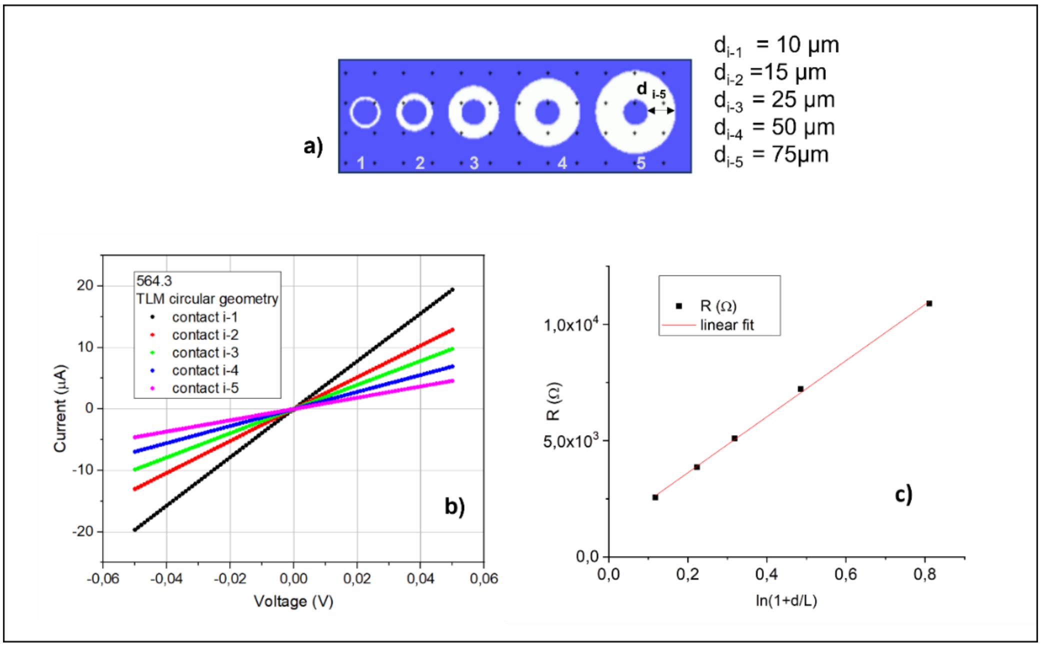

Fig.3.16 (a) Circular TLM pattern, (b) I-V characteristics measured on i-1, i-2, i-3, i-4, i-5 contact pairs and (c) R-L profile for Si-doped ε - Ga_2O_3 sample (Ti/Au contacts).

TLM analysis of the samples leads to the values of the specific contact resistance $\rho_c = (2 \div 3) \cdot 10^{-3}\ \Omega cm^2$. These values can be considered as the state of the art for the ε-polymorph. The specific contact resistance results still high with respect to the value reported by literature referred to the β-phase ($\rho_c = 10^{-4} - 10^{-6}\ \Omega cm^2$) [24]. However, it is important to highlight that good ohmic contacts with the β-phase were obtained only after annealing treatment at high temperature [25]. Conversely, each of our structures were made without any thermal treatment, that is a strong requirement for electronic devices based on the metastable ε-Ga_2O_3 polymorph.

References

[1] J. B. Varley, J. R. Weber, A. Janotti and C. G. Van de Walle, “Oxygen vacancies and donor impurities in β-Ga2O3,” *Applied Physics Letters,* vol. 97, no. 14, p. 142106, 2010.

[2] S. Lany, “Defect phase diagram for doping of Ga2O3,” *APL Materials,* vol. 6, no. 4, p. 046103, 2018.

[3] N. T. Son, K. Goto, K. Nomura, Q. T. Thieu, R. Togashi, H. Murakami, Y. Kumagai, A. Kumarata, M. Higashiwaki, A. Koukito, S. Yamakoshi, B. Monemar e E. Janzén, «Electronic properties of the residual donor in unintentionally doped β-Ga2O3,» *Journal of Applied Physics,* vol. 120, n. 23, p. 235703, 2016.

[4] N. Ueda, H. Hosono, R. Waseda and H. Kawazoe, “Synthesis and control of conductivity of ultraviolet transmitting β-Ga 2 O 3 single crystals,” *Applied Physics Letters,* vol. 70, no. 26, pp. 3561-3563, 1997.

[5] M. Baldini, M. Albrecht, A. Fiedler, K. Irmscher, R. Schewski and G. Wagner, “Si-and Sn-doped homoepitaxial β-Ga2O3 layers grown by MOVPE on (010)-oriented substrates,” *ECS Journal of Solid State Science and Technology,* vol. 6, no. 2, p. Q3040, 2016.

[6] A. M. M. B. E. Kyrtsos, “On the feasibility of p-type Ga2O3,” *Applied Physics Letters,* vol. 112, no. 3, p. 032108, 2018.

[7] J. B. Varley, A. Janotti, C. Franchini and C. G. Van de Walle, “Role of self-trapping in luminescence and p-type conductivity of wide-band-gap oxides,” *Physical Review B,* vol. 85, no. 8, p. 081109, 2012.

[8] M. Mulazzi, F. Reichmann, A. Becker, W. M. Klesse, P. Alippi, V. Fiorentini and R. Fornari, “The electronic structure of ε-Ga2O3,” *APL Materials,* vol. 7, no. 2, p. 022522, 2019.

[9] J. Kim, D. Tahara, Y. Miura and B. G. Kim, “First-principle calculations of electronic structures and polar properties of (κ, ε)-Ga2O3,” *Applied Physics Express,* vol. 11, no. 6, p. 061101, 2018.

[10] A. Parisini, A. Bosio, V. Montedoro, A. Gorreri, A. Lamperti, M. Bosi, G. Garulli, S. Vantaggio and R. Fornari, “Si and Sn doping of ε-Ga2O3 layers,” *APL Materials,* vol. 7, no. 3, p. 031114, 2019.

[11] A. Bosio, A. Parisini, A. Lamperti, C. Borelli, L. Fornasini, M. Bosi, I. Cora, Z. Fogarassy, B. Pécz, Z. Zolnai, A. Németh, S. Vantaggio and R. Fornari, “n-Type doping of ε-Ga2O3 epilayers by high-temperature tin diffusion,” *Acta Materialia,* vol. 210, p. 116848, 2021.

[12] A. Lamperti, E. Cianci, O. Salicio, L. Lamagna, S. Spiga and M. Fanciulli, “Thermal stability of high-κ oxides on SiO2/Si or SixNy/SiO2/Si for charge-trapping nonvolatile memories,” *Surface and interface analysis,* vol. 45, no. 1, pp. 390-393, 2013.

[13] M. Mayer, “Improved physics in SIMNRA 7,” *Nuclear Instruments and Methods in Physics Research Section B: Beam Interactions with Materials and Atoms,* vol. 332, pp. 176-180, 2014.

[14] B. I. Shklovskii and A. L. Efros, Electronic properties of doped semiconductors, vol. 45, Springer Science & Business Media., 2013.

[15] A. Parisini, A. Parisini and R. Nipoti, “Size effect on high temperature variable range hopping in Al+ implanted 4H-SiC,” *Journal of Physics: Condensed Matter,* vol. 29, no. 3, p. 035703, 2016.

[16] Y. U. Peter and M. Cardona, Fundamentals of semiconductors: physics and materials properties, Springer Science & Business Media, 2010.

[17] F. Roccaforte, F. La Via and V. Raineri, “Ohmic contacts to SiC,” *International journal of high speed electronics and systems,* vol. 15, no. 04, pp. 781-820, 2005.

[18] F. C. Chiu, “A review on conduction mechanisms in dielectric films,” *Advances in Materials Science and Engineering,* 2014.

[19] S. J. Pearton, J. Yang, P. H. Cary IV, F. Ren, J. Kim, M. J. Tadjer and M. A. Mastro, “A review of Ga2O3 materials, processing, and devices,” *Applied Physics Reviews,* vol. 5, no. 1, p. 011301, 2018.

[20] M. H. Lee and R. L. Peterson, “Interfacial reactions of titanium/gold ohmic contacts with Sn-doped β-Ga2O3,” *APL Materials,* vol. 7, no. 2, p. 022524, 2019.

[21] A. Bosio, C. Borelli, A. Parisini, M. Pavesi, S. Vantaggio and R. Fornari, “A Metal-Oxide Contact to ε-Ga2O3 Epitaxial Films and Relevant Conduction Mechanism,” *ECS Journal of Solid State Science and Technology,* vol. 9, no. 5, p. 055002, 2020.

[22] D. Joung, A. Chunder and L. K. S. I. Zhai, “Space charge limited conduction with exponential trap distribution in reduced graphene oxide sheets,” *Applied Physics Letters,* vol. 97, no. 9, p. 093105, 2010.

[23] M. Choueib, A. Ayari, P. Vincent, S. Perisanu and S. T. Purcell, “Evidence for Poole - Frenkel conduction in individual SiC nanowires by field emission transport measurements,” *Journal of Applied Physics,* vol. 109, no. 7, p. 073709, 2011.

[24] M. H. Wong, Y. Nakata, A. Kuramata, S. Yamakoshi and M. Higashiwaki, “Enhancement-mode Ga2O3 MOSFETs with Si-ion-implanted source and drain,” *Applied Physics Express,* vol. 10, no. 4, p. 041101, 2017.

[25] M. H. Lee and R. L. Peterson, “Interfacial reactions of titanium/gold ohmic contacts with Sn-doped β-Ga2O3,” *APL Materials,* vol. 7, no. 2, p. 022524, 2019.

Chapter 4 – UV-C solar-blind photodetectors based on ε-Ga_2O_3

In this chapter, electrical and optical investigations of UV-C photodetectors based on nominally undoped ε-Ga_2O_3 epilayers are presented. Remarkable results such as high responsivity, solar-blind rejection ratio ($R_{UV\text{-}SUN}$) greater than 10^4 and good ON-OFF photoresponse make the epsilon phase of gallium oxide as an excellent material for UV-C detection. Test structures showed a remarkable photo-gain, which is attributed to the excess of collected majority carriers (electrons) Δn, possibly related to holes trapping/self-trapping effects in the conductive channel.

4.1 Introduction

Solar-blind UV-C photodetectors have attracted significant interest in recent years due to their potential applications in civil, industrial and military fields [1, 2]. The ultraviolet (UV) radiation covers the spectral wavelength range (400÷10) nm, typically divided into four wavebands: UVA (315 nm < λ < 400 nm), UVB (280 nm < λ < 315 nm), UV-C (100 nm < λ < 280 nm) and extreme ultraviolet EUV (10 nm < λ < 120 nm) [3]. Among the solar UV radiation, the UV-C photons are absorbed by atmospheric diatomic oxygen and by ozone layer, while almost all of UV-A and a small fraction of UV-B radiation reaches the Earth surface (Fig.4.1). Detectors that are sensitive to radiation below 280 nm are called solar-blind photodetectors, meaning they can detect UV-C light even in daylight conditions.

Wide-bandgap semiconductors such as SiC [4], GaN [5], and ZnO [6] have been used to fabricate UV photodetectors, but to meet the criteria of a solar-blind photodetector the use of external optical filters is required to cut the contribution of the visible radiation. In addition, ternary semiconductor alloys such as $Al_xGa_{1-x}N$ [7] and $Mg_xZn_{1-x}O$ [8] are promising candidates for solar blind applications. However, these ternary alloys suffer from phase segregation [9, 10], leading to the generation of defects and dislocations around discrete domains reducing the performance of the detector.

Recently, ε-Ga_2O_3 is emerging as a promising material for UV-C solar-blind photodetector fabrication thanks to its unique properties such as intrinsic spectral selectivity in the UV-C spectral region, availability of good-quality epitaxial layers, good matching on foreign substrates, and cost-effective growth methods.

ε-Ga_2O_3-based UV-C photodetector could be integrated in solar-blind UV cameras for the detection of the corona discharge, a phenomenon that occurs just before the breakdown of the ceramic insulators in high voltage electrical systems. Moreover, it can be used as flame detector, for early detection of forest fires, as well as for anti-fire surveillance in industries involved in storing or transportation of flammable materials.

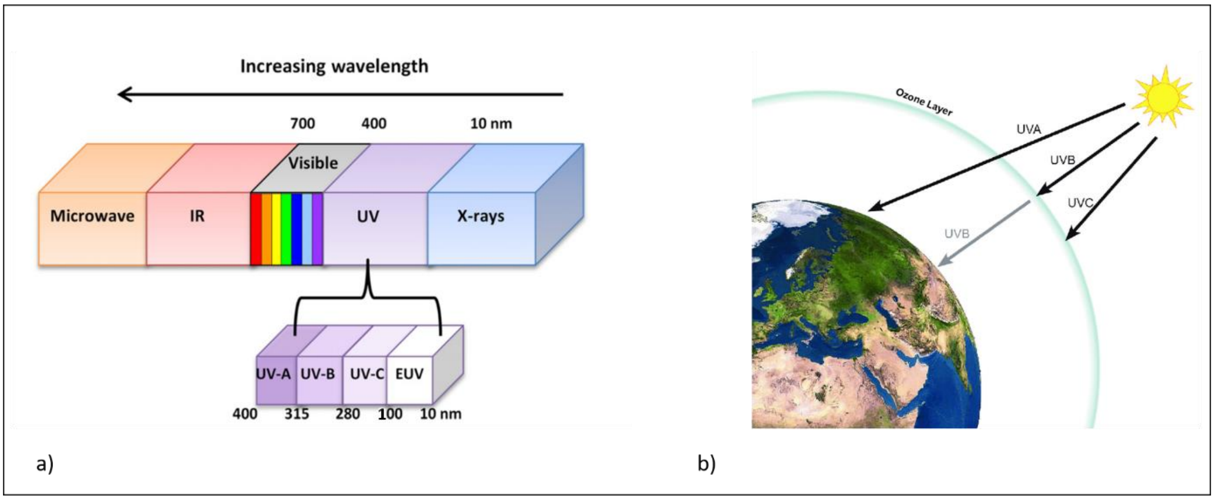

Fig.4.1 (a) Electromagnetic spectrum with magnification of the UV region. (b) Schematic illustration of solar UV radiation that reaches the Earth surface.

4.2 Electrical and optical characterization

Test devices were made on highly resistive ε-Ga_2O_3 layers ($\rho \sim 10^8$ Ωcm) grown by MOCVD on c-oriented Al_2O_3 substrates. Planar electrodes were fabricated on top of ε-Ga_2O_3 layers through a stencil metal mask by sputter deposition of SnO_x+ITO+Au layers, as shown in Fig.4.2. Such a contacts deposition is the same as that used to fabricate reliable ohmic contacts on ε - Ga_2O_3 films, as described in the Chapter 3.

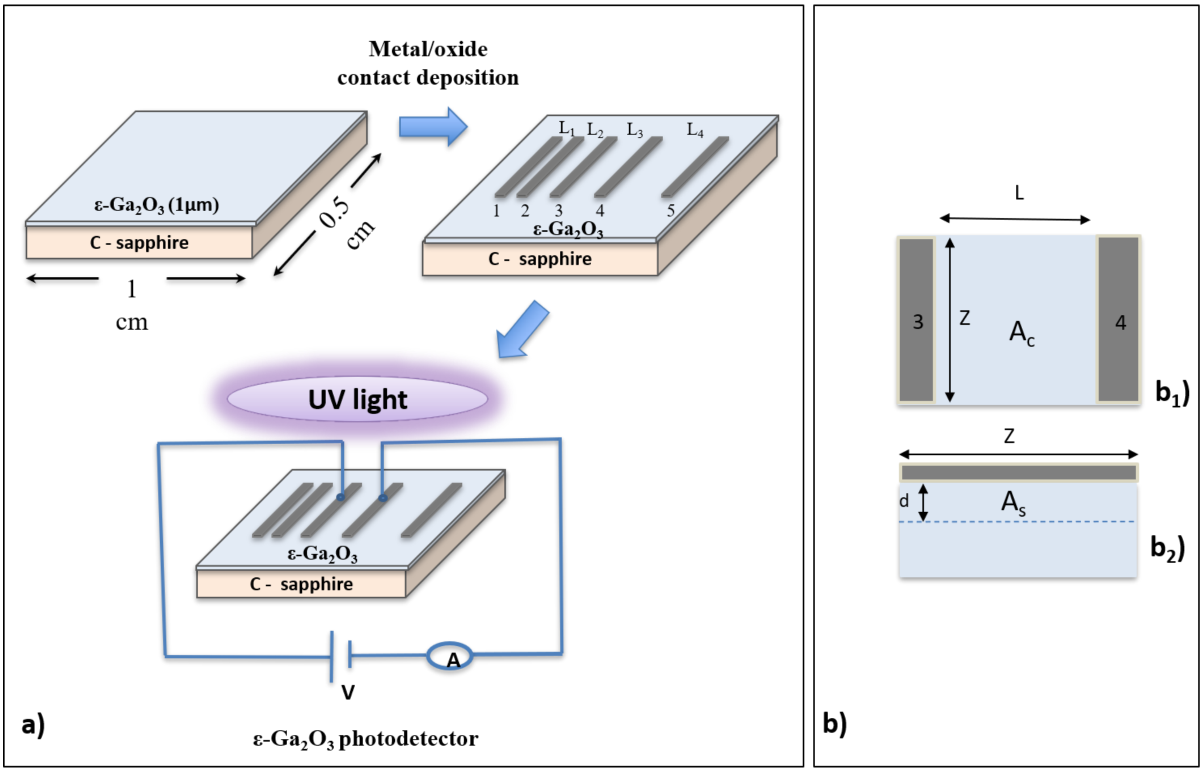

Fig.4.2 (a) Schematic representation of the fabrication of MSM Ga_2O_3-based UV photodetector. Panel (b) shows the top view of the illuminated area $A_c = Z \cdot L$ (b_1) and the cross-sectional area of the detector $A_s = Z \cdot d$ (b_2).

To check the photoresponse of the detector at UV-C radiation, current-voltage (I-V) characteristics in dark condition and under UV-C illumination (λ = 250 nm) were recorded. Fig.4.3a shows the I-V curves on semi-log scale, measured between the contacts 3-4. In dark condition a current signal lower than 1 nA at 50 V is observed, conversely a significant photocurrent of about 1 µA at 50 V is detected as the photodetector is exposed at 250 nm light. The spectral responsivity $R(\lambda)$ is a basic physical quantity used to evaluate the sensitivity of a photodetector at a specific wavelength and it is defined as follows:

$$R(\lambda) = \frac{I_{meas}}{P_{inc}(\lambda)} \tag{4. 1}$$

where, I_{meas} is the measured photocurrent at a certain voltage and $P_{inc}(\lambda)$ is the optical power at a specific wavelength that strikes the sample. The typical responsivity of our ε-Ga_2O_3 based detectors in the wavelength range (650 – 250) nm is shown in Fig.4.3b.

The UV-to-VIS rejection ratio (R_{UV-VIS}) is one of the important figures of merit of UV photodetectors. R_{UV-VIS} is used to evaluate the spectral selectivity of the detector in UV solar-blind region with respect to visible region and is defined as:

$$R_{UV-VIS} = \frac{R_{250}}{R_{500}} \tag{4. 2}$$

where, R_{250} and R_{500} are the responsivity values at $\lambda = 250\,nm$ and $\lambda = 500\,nm$, respectively. A value of $R_{UV-VIS} > 10^4$ indicates a negligible photoresponse to visible excitation, which is a strict requirement for UV solar-blind detection [11].

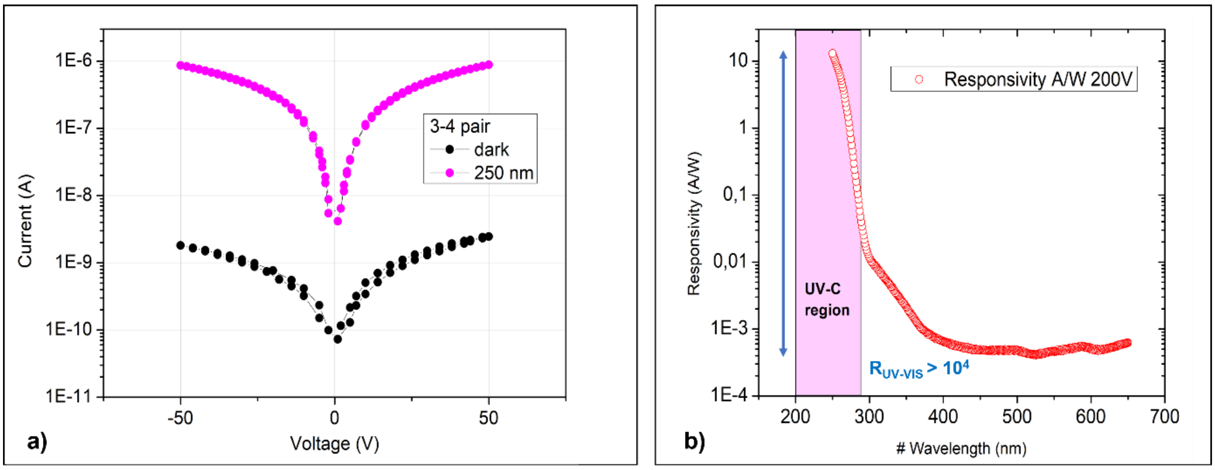

Fig.4.3 I-V curves with semi-log scale in dark and under 250 nm UV-C light illumination, measured on the 3-4 contact pair. (b) Responsivity spectrum in the UV-visible region applying a bias of 200 V.

4.2.1 Photo-gain mechanism

The photo-gain G is defined as the number of photogenerated charge carriers collected by electrodes (N_{el}) divided by the number of absorbed photons ($N_{ph,abs}$). It thus quantifies the capability of the photodetector to collect photogenerated carriers at the electrodes relatively to the density of absorbed photons [12].

$$G(\lambda) = \frac{N_{el}}{N_{ph,abs}(\lambda)} = \frac{J_{ph}A_s/e}{P_{abs}/\hbar\omega} \tag{4. 3}$$

where J_{ph} is the photocurrent density, e the electron charge, $P_{abs}/\hbar\omega$ is the total number of photons absorbed, and $A_s = Z \cdot d$ is the cross-sectional area of the layer, with Z the contact length and d the thickness in which photons are totally absorbed (see Fig.4.2b).

From Eq (4.1) and Eq (4.3) the responsivity can be expressed in terms of photo-gain as follows:

$$R(\lambda) = \frac{I_{meas}}{P_{inc}(\lambda)} = \frac{eN_{el}}{\frac{hc}{\lambda}N_{ph,inc}(\lambda)} \cdot \frac{N_{ph,abs}(\lambda)}{N_{ph,abs}(\lambda)} = \frac{\lambda e}{hc} A(\lambda) \cdot G(\lambda) = R_{ideal}(\lambda) \cdot EQE(\lambda) \tag{4. 4}$$

where λ is the wavelength of the incident radiation, h is the Planck constant, c is the speed of light in vacuum, e is the electron charge, $N_{ph,inc}(\lambda)$ is the number of incident photons, $A(\lambda)$ is the absorbance, and the product $A(\lambda) \cdot G(\lambda)$ is the external quantum efficiency EQE. In the ideal case, when all photogenerated carriers are collected at the electrodes $EQE = 1$ and the responsivity at $\lambda = 250\ nm$ will be $R_{ideal} = 0{,}21\ A/W$.

Responsivity spectra performed at different voltages under UV-C illumination in the wavelength range (250÷300) nm are shown in Fig.4.4a. Photo-gain values as a function of the applied voltage are reported in Fig.4.4b, obtained by normalizing the spectral responsivity at $\lambda = 250\ nm$ to the ideal responsivity $R_{ideal} = 0.21\ A/W$. As it is clearly visible in Fig.4.4b, photo-gain reaches a value of about 50 with a bias of 200 V, overcoming its theoretical value $G = 1$.

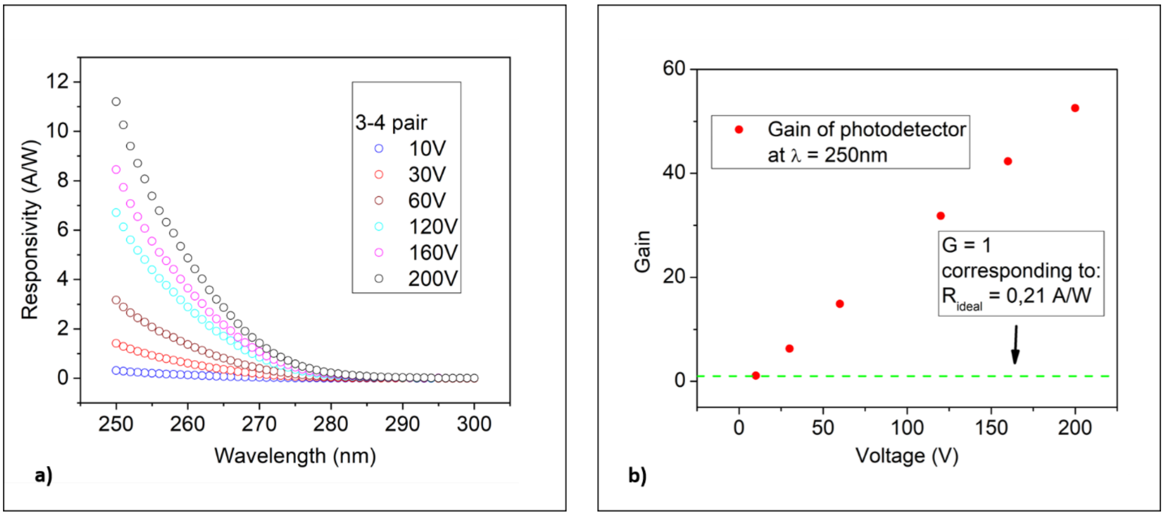

Fig.4.4 (a) Responsivity spectra in the wavelength range (250÷300) nm recorded by applying an increasing voltage to the 3-4 contact pair. (b) Photo-gain (G) as a function of the applied voltage at λ = 250 nm. The dashed green line represents the ideal value of photo-gain G = 1 at λ = 250 nm, corresponding to R_{ideal} = 0.21 A/W [13].

In order to explain such a photo-gain effect, an analysis of photoconduction mechanisms related to the transport properties of gallium oxide is required.

The photo-gain G can be rewritten in terms of the carrier generation rate g, defined as the number of photocarriers generated per absorbed photon in the unit volume.

$$g = \frac{P_{abs}}{V\hbar\omega} \tag{4. 5}$$

where V is the volume layer given by $V = A_c d = ZLd$, with A_c the illuminated area and L the distance between the contacts. By substituting Eq (4.5) into Eq (4.3) the expression for G becomes:

$$G = \frac{J_{ph}}{geL} \tag{4. 6}$$

The photocurrent density J_{ph} may also be expressed as a function of the density of photogenerated carriers Δn and Δp, mobility μ_n and μ_p and electric field E:

$$J_{ph} = e(\mu_n \Delta n + \mu_p \Delta p) \cdot E \tag{4. 7}$$

Considering an ideal n-type photodetector under constant illumination and low-injection conditions, that is $\Delta n \ll n_o$, where n_o is the equilibrium carrier concentration, the excess of photogenerated carriers (electrons and holes) are equal and uniformly distributed in space. In these conditions the electrical transport is ruled by minority carriers, then:

$$\Delta n = \Delta p = g\tau_p \tag{4. 8}$$

where, τ_p is the mean lifetime of the holes.

Replacing Eqs (4.7, 4.8) into Eq (4.6) the expression of *G* will be:

$$G = \frac{\tau_p \mu_p E}{L}\left(1 + \frac{\mu_n}{\mu_p}\right) = \frac{\tau_p}{\tau_t}\left(1 + \frac{\mu_n}{\mu_p}\right) \tag{4. 9}$$

where μ_n and μ_p are the electron and hole mobilities, $\tau_t = L/(\mu_p \cdot E)$ represents the transit time for holes (assuming a uniform electric field and without any trapping phenomenon), with L the distance between a contact pair. This is the classic gain expression in an ideal n-type photodetector, providing a linear increase of gain with the applied bias.

High values of *G* (up to 10^5) observed in Ga_2O_3 MSM photodetectors [14] cannot be explained neither by the classical gain theory, nor as result of avalanche phenomena, which occur at very high electric fields ($10^6 \div 10^7$) V/cm.

In order to clarify this aspect, it is important to point out that the classical gain expression is obtained taking into account the following assumptions:

1. Low injection conditions are assumed to be valid ($\Delta n \ll n_o$), so that the electrical conductivity is ruled by minority carriers.
2. The expression $\Delta n = \Delta p = g\tau_p$ is true only if the photogenerated carriers are uniformly distributed in space and in time.
3. The electric field is assumed to be uniform and carrier trapping phenomena are not considered.

These assumptions make questionable the applicability of Eq. (4.9) in a purely resistive photoconductor for the following aspects:

1. In high-injection optical conditions the photogenerated carrier density exceeds its equilibrium carrier density ($\Delta n \gg n_o$). This condition is easily obtained in highly resistive photodetectors based on nominally undoped ε-Ga_2O_3.

2. In highly resistive MSM photodetectors the distribution of charge carriers is always nonuniform close to the electrodes, since the illuminated area of detector is adjacent to the region not affected by the radiation, that is the region underneath the metal contacts (see Fig.4.5). This effect increases upon electric field increases, as suggested by the continuity equation for minority carriers [15], and it affects the whole photoconductive channel.
3. In a real semiconductor the photo-gain could be related to carrier trapping phenomena inside the material [15], making questionable the assumption $\Delta n = \Delta p$. As well known, photons absorbed by a semiconductor generate electron-hole pairs, which are evenly collected at the electrodes by applying an electric field. However, when carrier trapping effects occur, the photocarriers can be collected at the electrodes with different rates, therefore, in these conditions $\Delta n \neq \Delta p$.

   In particular, hole trapping/self-trapping phenomena observed in Ga_2O_3 polymorphs [16] supports the hypothesis $\Delta n > \Delta p$ while $\mu_n > \mu_p$ due to the very different effective masses of free carriers. For this reason, to justify the high experimental values of *G* measured in ε-Ga_2O_3 photodetector (Fig.4.4b), one has to modify Eq. (4.9) considering the actual ratio of the photocarriers density $\gamma = \Delta n/\Delta p$, with $\gamma \gg 1$:

$$G = \frac{\tau_p}{\tau_t}\left(1 + \gamma \cdot \frac{\mu_n}{\mu_p}\right) \tag{4.10}$$

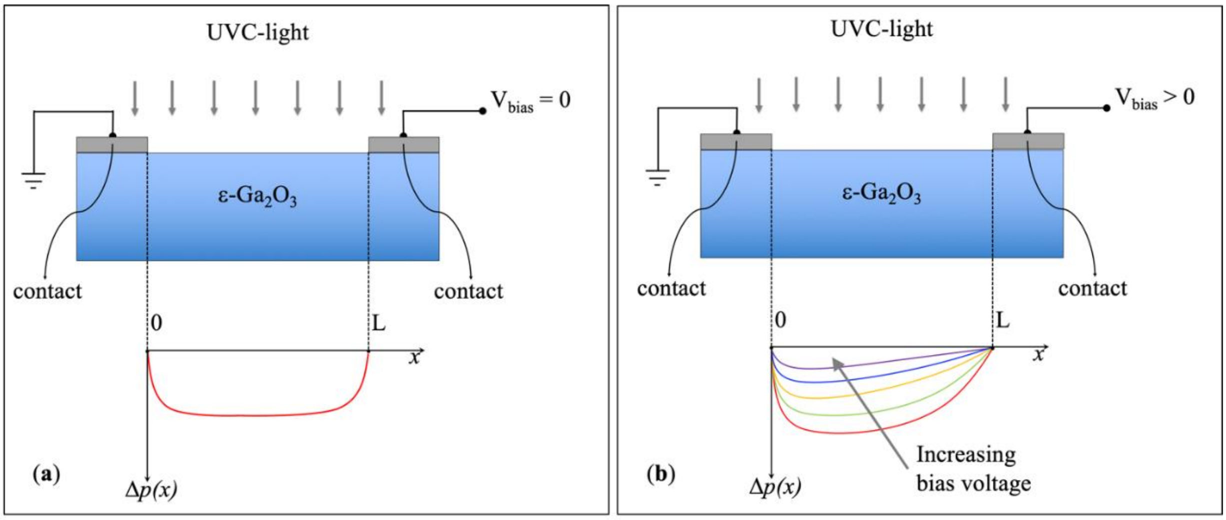

Fig.4.5 Schematic illustration of distribution of photogenerated holes $\Delta p(x)$ vs. the distance between the electrodes under uniform UV-C light: no bias applied (a) and with bias applied (b) [13].

The Eq. (4.10), however, is not valid if the distribution of photogenerated carriers Δn and Δp are nonuniform into the photoconductive channel, as it occurs in our system.

For these reasons, it is more appropriate to introduce in low electric field limit the average excess carrier concentration $\Delta p(x) = \Delta p_{avg}$ and $\Delta n(x) = \Delta n_{avg}$, which replace Δn and Δp, respectively. In this case, $\Delta p_{avg} = g\tau_{p,eff}$, with τ_{peff} is the effective mean lifetime for holes, and $\Delta p(x) \neq \Delta n(x)$.

Eq. (4.10) then can be rewritten as:

$$G = \frac{\tau_{peff}}{\tau_t}\left(1 + \gamma \cdot \frac{\mu_n}{\mu_p}\right) \tag{4.11}$$

which is consistent with a linear behaviour of the gain on the applied voltage and substitutes the classical gain expression of Eq. (4.9).

A simple interpretation of how hole trapping effects can generate high gain in a photoconductor is the following: under uniform illumination, a constant density of photogenerated holes N_h is trapped and equal density of free photoelectrons $N_e = N_h$ must be preserved in the photoconductive channel to ensure the local charge neutrality in time. After that, light will continue to generate free electrons and free holes in equal quantities, $g\tau_{p,eff}$. By applying an electric field, free holes and free electrons are collected at the electrodes with different densities, on average $\Delta p = g\tau_{p,eff}$ for free holes and $\Delta n = g\tau_{p,eff} + N_e$ for free electrons. This mechanism supports the condition $\Delta n > \Delta p$, and as a consequence, a γ value much higher than unity is obtained.

In conclusion, high values of photo-gain in our photodetectors can be attributed to the excess of collected majority carriers (electrons), with respect to the minority carriers (holes), possibly related to hole trapping/self-trapping processes in the photoconductive channel.

4.2.2 Time-dependent photoresponse

The stability and the performance of the detector was evaluated by ON-OFF photoresponse measurements. Fig.4.6a shows the time-dependent photocurrent signal measured at λ=250 nm applying a bias of 200 V. ON-OFF switching cycles were repeated for three times and the photocurrent profile remained practically the same, demonstrating the good stability and reproducibility over time of the photodetector.

The rise and decay time of the photocurrent (PC) signal at λ=250 nm was also analyzed (Fig.4.6b).

Generally, in a photodetector the rise time is defined as the time required for the photocurrent to increase from 10% to 90% of its maximum value in the on-transient(τ_{ON}), while the decay time is defined as the time required for the photocurrent to decrease from 90% of the highest value to 10% in the off-transient (τ_{OFF}) [17].

In our case, both up and down PC transients at λ=250 nm may be well described by the following equation:

$$I(t) = I_0 + A\, exp\left(-\frac{t}{\tau_1}\right) + B\, exp\left(-\frac{t}{\tau_2}\right) \tag{4.12}$$

where I_0 is the dark current contribution, A and B are costants, τ_1 and τ_2 represent the fast and slow time constants, respectively. The fast-time component is the most important parameter to evaluate the performance of a photodetector in terms of response speed and it is related to the band-to-band transition, while the slow-time component is attributed to charge carrier trapping/de-trapping through deep levels within the bandgap of Ga_2O_3 [18].

In our case, $\tau_{1\,ON}$ and $\tau_{1\,OFF}$ were found to be around 0.7 s and 0.3 s, respectively, which are comparable to those reported in literature for different UV photodetectors based on Ga_2O_3 (see Tab.4.1).

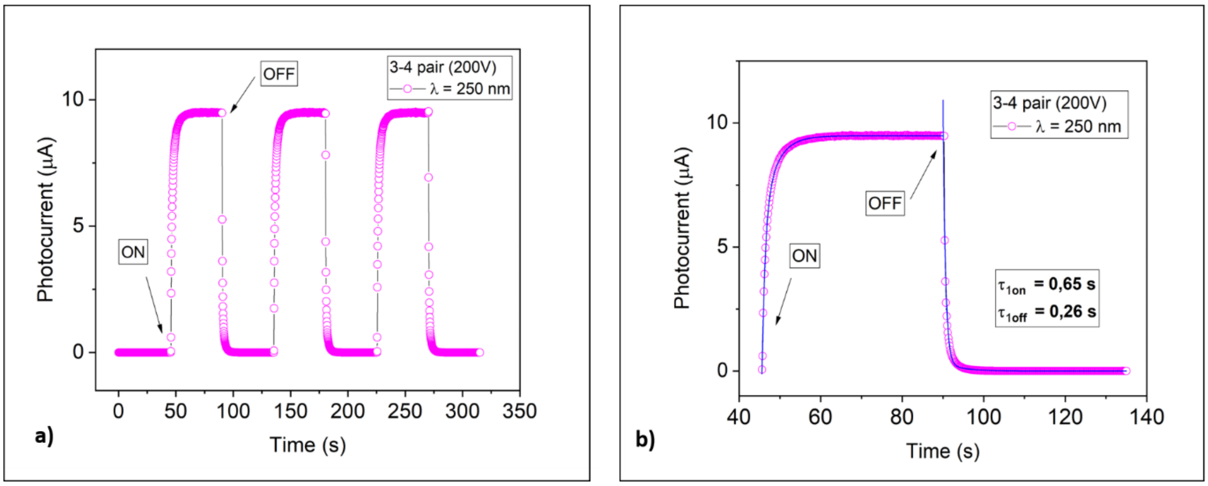

Fig.4.6 (a) Time-resolved photoresponse under 250 nm light (I = 16 μW/cm^2), measured on the 3-4 contact pair applying a bias of 200 V. (b) Experimental (circles) and fitted (line) curves of the current rise and decay process at 250 nm illumination [13].

Tab.4.1 Collection of the optical parameters related to MSM Ga_2O_3-based UV photodetectors [13].

Ga_2O_3	Structure	Responsivity [A/W]	Rejection Ratio	τ_{rise} (s)	τ_{decay} (s)	Reference
ε	Ohmic MSM (SnO_x+ITO+Au)	**11 (at 200V)**	**> 10^4**	**0.7**	**0.3**	**This thesis**
ε	Schottky MSM (Au)	0.52 (at 5V)	1.82×10^4	-	0.33	[19]
β	Ohmic MSM (Ti/Au)	-	-	0.86	1.02	[18]
β	Ohmic MSM (Ti/Au)	259 (at 20V)	1×10^2	0.1	2.1	[20]
β	Ohmic MSM (Ti/Au)	8.41 (at 10V)	3.2×10^3	2.97	0.41	[21]
β	Ohmic MSM (Ti/Al)	54.9 (at 20V)	3.2×10^3	2	0.56	[22]
β	Schottky MSM (Ni/Au)	0.9 (at 5V)	7.8×10^4	< 1	< 3	[23]

To emphasize solar-blind photoresponse of the detector, additional characterization using a solar simulator was performed. The aim of this study was to point out the solar-blind performance of the detector, taking into account the radiation actually impinging on the device. In particular, using a sunlight irradiance (I = 80mW/cm^2), that is over three order of magnitude higher than applied UV-C illumination (I=16µW/cm^2) on the photodetector, the UV-C photoresponse is much stronger than the one from sunlight signal, as showed in Fig.4.7.

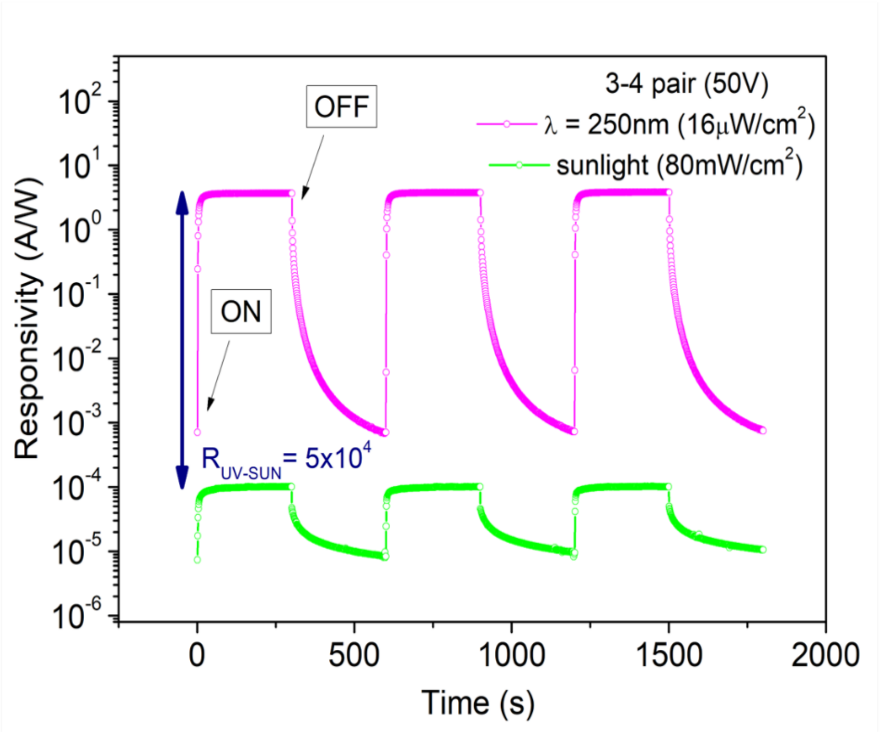

Fig.4.7 Photocurrent transients in Log scale in sunlight condition (green line) and under λ=250 nm illumination (violet line) with 50 V applied bias [13].

The sunlight contribution R_S can be determined by:

$$R_S = \frac{\int_{400}^{700} f(\lambda)R(\lambda)d\lambda}{\int_{280}^{4000} f(\lambda)d\lambda} \tag{4.13}$$

where, $R(\lambda)$, measured in $[\frac{A}{W}]$, is the spectral responsivity of the detector, and $f(\lambda)$, measured in $\frac{W}{cm^2 * nm}$, is the spectral irradiance of the solar simulator.

Considering the responsivity at 250 nm $(R_{UV} = 3.5\frac{A}{W})$ and the sunlight contribution $(R_S = 0.7 \times 10^{-4}\frac{A}{W})$, an UV-to-sunlight rejection ratio R_{UV-SUN} of 5×10^4 was obtained, which confirms the excellent solar-blind performance of the photodetector.

The sensitivity of the detector to the UV-C radiation was confirmed by photoresponse measurements under different 250 nm light intensity (Fig.4.8a). The photocurrent signal can be expressed by a power law of the form $I = AP^{\alpha}$, where I is the photocurrent, A is a constant, P is the irradiance, and α determines the photocurrent response to light intensity. The photocurrent data in the Log-Log scale (Fig.4.8b) show a linear trend in the range 0.37 ÷ 30.2 µW/cm^2, which confirms the capability of the device to detect a wide range of UV-C radiation.

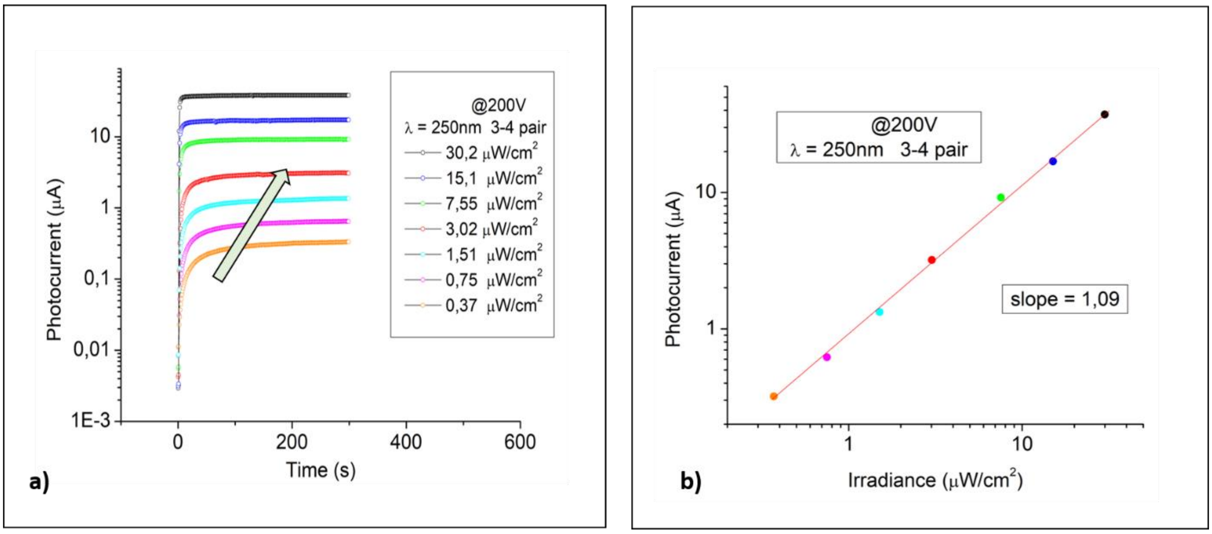

Fig.4.8 (a) Time-dependent photoresponse at different UV-C light intensity. (b) Photocurrent signals (full circles) taken at t_{on}=300 s as a function of irradiance in Log-Log scale (at 200V applied bias). Red solid line represents the fit of the power law $I = AP^{\alpha}$ with α = 1.09.

References

[1] H. Chen, K. Liu, L. Hu, A. A. Al-Ghamdi and X. Fang, "New concept ultraviolet photodetectors," *Materials Today,* vol. 18, no. 9, pp. 493-502, 2015.

[2] C. Xie, X. T. Lu, X. W. Tong, Z. X. Zhang, F. X. Liang, L. Liang, L. Luo e Y. C. Wu, «Recent progress in solar-blind deep-ultraviolet photodetectors based on inorganic ultrawide bandgap semiconductors,» *Advanced Functional Materials,* vol. 29, n. 9, p. 18060, 2019.

[3] Space Environment (Natural and Artificial) - Process for determining solar irradiances - ISO 21348, 2007.

[4] X. Chen, H. Zhu, J. Cai and Z. & Wu, "High-performance 4H-SiC-based ultraviolet p-i-n photodetector," *Journal of Applied Physics,* vol. 102, no. 2, p. 024505, 2007.

[5] K. Osamura, K. Nakajima, Y. Murakami, P. H. Shingu and A. Ohtsuki, "Fundamental absorption edge in GaN, InN and their alloys," *Solid State Communications,* vol. 11, no. 5, pp. 617-621, 1072.

[6] J. D. Ye, S. L. Gu, S. M. Zhu, S. M. Liu, Y. D. Zheng, R. Zhang, Y. Shi, H. Yu and Y. D. Ye, "Gallium doping dependence of single-crystal n-type ZnO grown by metal organic chemical vapor deposition," *Journal of crystal growth,* vol. 283, no. 3-4, pp. 279-285, 2005.

[7] Z. G. Shao, D. J. Chen, H. Lu, R. Zhang, W. J. Luo, Y. D. Zheng, D. Cao, Y. Luo, D. Zheng, L. Li and Z. H. Li, "High-gain AlGaN solar-blind avalanche photodiodes," *IEEE Electron Device Letters,* vol. 35, no. 3, pp. 372-374, 2014.

[8] J. Yu, C. X. Shan, J. S. Liu, X. W. Zhang, B. H. Li and D. Z. Shen, "MgZnO avalanche photodetectors realized in Schottky structures," *physica status solidi (RRL)–Rapid Research Letters,* vol. 7, no. 6, pp. 425-428, 2013.

[9] W. Yang, S. S. Hullavarad, B. Nagaraj, I. Takeuchi, R. P. Sharma, T. Venkatesan, R. D. Vispute and H. Shen, "Compositionally-tuned epitaxial cubic Mg x Zn 1− x O on Si (100) for deep ultraviolet photodetectors," *Applied Physics Letters,* vol. 82, no. 20, pp. 3424-3426, 2003.

[10] A. Cremades, M. Albrecht, J. Krinke, R. Dimitrov, M. Stutzmann and H. P. Strunk, "Effects of phase separation and decomposition on the minority carrier diffusion length in Al x Ga 1− x N films," *Journal of Applied Physics,* vol. 87, no. 5, pp. 2357-2362, 2000.

[11] X. Chen, F. Ren, S. Gu and J. Ye, "Review of gallium-oxide-based solar-blind ultraviolet photodetectors," *Photonics Research,* vol. 7, no. 4, pp. 381-415, 2019.

[12] R. H. Bube, Photoconductivity of solids, Wiley & Sons, Inc, 1960.

[13] C. Borelli, A. Bosio, A. Parisini, M. Pavesi, S. Vantaggio and R. Fornari, "Electronic properties and photo-gain of UV-C photodetectors fabribated from high-resistivity Ga2O3 epilayers," *Materials Science & Engineering B (submitted).*

[14] K. Arora, N. Goel, M. Kumar and M. Kumar, "Ultrahigh performance of self-powered β-Ga2O3 thin film solar-blind photodetector grown on cost-effective Si substrate using high-temperature seed layer," *Acs Photonics,* vol. 5, no. 6, pp. 2391-2401, 2018.

[15] Y. Dan, X. Zhao, K. Chen and A. Mesli, "A photoconductor intrinsically has no gain," *Acs Photonics,* vol. 5, no. 10, pp. 4111-4116, 2018.

[16] J. L. Lyons, "Electronic properties of Ga2O3 polymorphs," *ECS Journal of Solid State Science and Technology,* vol. 8, no. 7, p. Q3226, 2019.

[17] Y. J. Lu, C. N. Lin and C. X. Shan, "Optoelectronic diamond: growth, properties, and photodetection applications," *Advanced Optical Materials,* vol. 6, no. 20, p. 1800359, 2018.

[18] D. Guo, Z. Wu, P. Li, Y. An, H. Liu, X. Guo, H. Yan, G. Wang, C. Sun, L. Li and W. Tang, "Fabrication of β- Ga2O3 thin films and solar-blind photodetectors by laser MBE technology," *Optical Materials Express,* vol. 4, pp. 1067-1076, 2014.

[19] Z. Liu, Y. Huang, C. Zhang, J. Wang, H. Li, Z. Wu, P. Li and W. Tang, "Fabrication of epsilon-Ga2O3 solar-blind photodetector with symmetric interdigital Schottky contacts responding to low intensity light signal," *Journal of Physics D: Applied Physics,* vol. 53, no. 29, 2020.

[20] X. Liu, P. Guo, T. Sheng, L. Qian, W. Zhang and Y. Li, "β-Ga2O3 thin films on sapphire pre-seeded by homo-self-templated buffer layer for solar-blind UV photodetector," *Optical Materials,* vol. 51, pp. 203-207, 2016.

[21] L. X. Qian, H. Y. Liu, H. F. Zhang, Z. H. Wu and W. L. Zhang, "Simultaneously improved sensitivity and response speed of beta-Ga2O3 solar-blind photodetector via localized tuning of oxygen deficiency," *Applied Physics Letters,* vol. 114, p. 113506, 2019.

[22] L.-X. Qian, H.-F. Zhang, P. T. Lai, Z.-H. Wu and X.-Z. Liu, "High-sensitivity β-Ga2O3 solar-blind photodetector on high-temperature pretreated c-plane sapphire substrate," *Optical Materials Express,* vol. 7, pp. 3643-3653, 2017.

[23] F. P. Yu, S. L. Ou and D. S. Wuu, "Pulsed laser deposition of gallium oxide films for high performance solar-blind photodetectors," *Optical Materials Express,* vol. 5, pp. 1240-1249, 2015.

Chapter 5 – Plasma processing of ε-Ga_2O_3 thin films

This chapter will mainly focus on the investigation of Ar-plasma treatments on nominally undoped and extrinsically Si-doped ε-Ga_2O_3 epilayers grown on c-oriented sapphire substrates, which represents the main topic carried out during the research period at the Paul Drude Institute of Berlin. ε-Ga_2O_3 samples have been electrically investigated before and after plasma exposures. It has been found that the Ar-plasma treatment induced a remarkable change in the conductivity of the layer (for both doped and undoped layers), possibly related to a partial amorphization of the Ga_2O_3 layer in the vicinity of the surface.

5.1 Introduction

The plasma treatment is a surface processing technique in which the layer surface is bombarded by partially ionized species. It can be employed as a dry etching for removing impurities and contaminants present on the surface of the material before any further manufacturing process. Such a process could induce – depending on the material and the treated surface – physical and/or chemical changes which could in turn result in a detectable variation of the surface conductivity [1, 2].

Recently, a significant increase of conductivity has been observed after Ar-plasma treatments in nominally undoped and Sn-doped β-Ga_2O_3 heteroepitaxial layers grown by MBE on c-oriented sapphire substrates [3]. It has been found that the Ar-plasma treatments induce a considerable change in the sheet conductivity of the β-layers with respect to the untreated ones, irrespectively to the presence of an extrinsic dopant (i.e. Sn-doped as well as in undoped layers). Further investigation of this phenomenon evidenced such sheet conductivity disappears after thermal treatments at T > 200 °C in oxygen (O_2) or forming gas (N_2/H_2).

A similar phenomenology can be expected also in ε-Ga_2O_3 samples. As undoped ε-Ga_2O_3 grown by MOVPE exhibits a very high intrinsic resistivity, therefore, a plasma surface treatment may represent a new approach to modulate its surface electrical properties. Moreover, a spatially selective plasma treatment is expected to favour in the areas exposed to plasma the formation of ohmic contacts of lower resistivity, with similar effects to those of local ion implantation.

The results on the β-polymorph are considered as the starting point for the present work, which consists on the investigation of the Ar-plasma treatments on ε-Ga_2O_3 and β-Ga_2O_3 epilayers grown by MOCVD and MBE, respectively.

The Ar-plasma treatment was performed in an ICP-RIE (inductively coupled plasma - reactive ion etching) reactor by using an argon plasma flux of 10 sccm at 100 Pa, 50 W (RIE power), and room temperature. In such a system the Ar-plasma is generated by an RF electric field, as a consequence of collisions of electrons with Ar atoms. The plasma density is controlled by the ICP power supply and the ion energy is controlled by the RIE power supply. The schematic of the ICP-RIE system is shown in Fig.5.1.

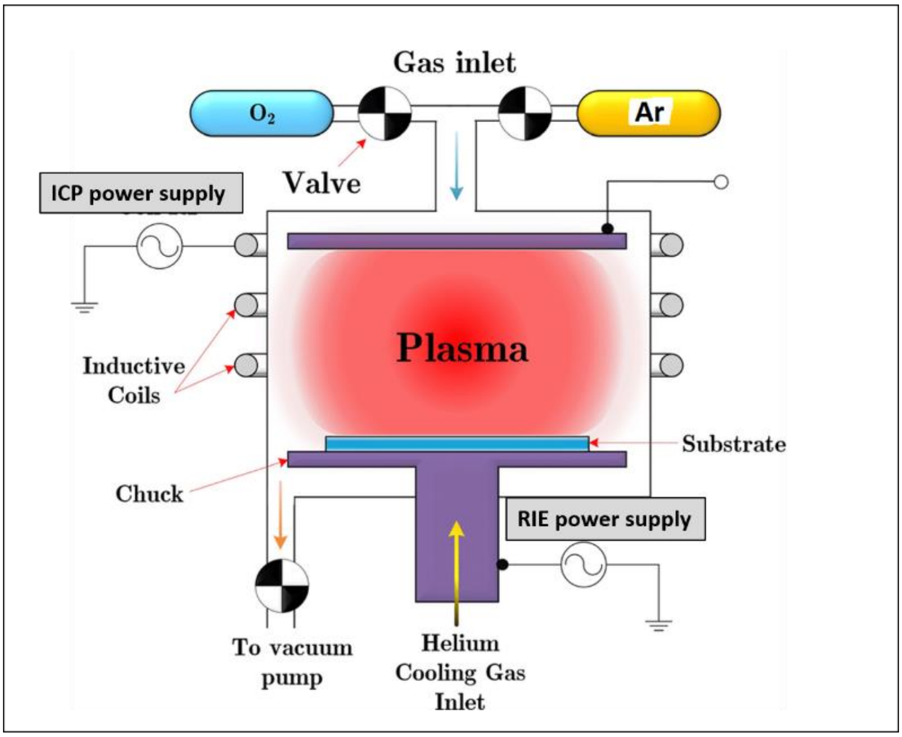

Fig.5.1 Schematic illustration of a typical ICP-RIE system.

5.2. Electrical investigation of Ar-plasma treated samples

5.2.1 Hall measurements

The investigated samples were ε-Ga_2O_3 and β-Ga_2O_3 heteroepitaxial layers grown on c-plane sapphire substrates by MOCVD and MBE, respectively. Ti (20 nm)/Pt (20 nm)/Au (100 nm) electrical contacts were deposited on top of ε-Ga_2O_3 layers in the van der Pauw configuration. Nominally undoped and extrinsically Si-doped ε-Ga_2O_3 layers have been electrically characterized by Hall measurements before and after the plasma exposures. It has been found that, for both doped and undoped layers, the Ar-plasma treatment improves the ohmic contacts and the sheet conductivity of the layer (see Tab.5.1). In particular, the nominally undoped ε-Ga_2O_3 layers (underlined in green colour) after the Ar-plasma treatment show a sheet resistance (R_{sh}) of about $10^3\Omega/sq$ (i.e much lower with respect to untreated layers, $R_{sh} > 10^{12}\Omega/sq$) and significant sheet Hall carrier concentration ($n_{sh}^H \sim 10^{14}cm^{-2}$) and mobility ($\mu = 20 - 30cm^2/Vs$). In the case of Si-doped ε-Ga_2O_3 layers (underlined in brown colour), n_{sh}^H remains almost constant after the Ar-plasma treatment, while $R_{sh}$and μ change respectively about one order of magnitude, with respect to untreated layers.

Nominally undoped β-Ga_2O_3 (-201) heteroepitaxial layers deposited on c-plane sapphire substrates were investigated. Interestingly, the effect of the plasma treatment was qualitatively the same as for the previously discussed ε-Ga_2O_3 layers, i.e. resulting in a decrease in the R_{sh} with respect to untreated layers. However, β-Ga_2O_3 layers show a higher sheet resistance ($R_{sh} \sim 10^6\Omega/sq$) compared to the ε-$Ga_2O_3$ samples ($R_{sh} \sim 10^3\Omega/sq$), despite having comparable layer thicknesses.

These data are in line to the previous investigation of Lapsanska *et al.* [3]. The different R_{sh} recorded for β and ε layers could be connected to the different structural defects in the two structures. In fact, this effect could be related to the presence of electrically charged twin domains in β-Ga_2O_3 (-201) layers [4, 5].

Different investigations have been performed in order to estimate the thickness of the Ar plasma-modified sheet and understand the physical reason behind the conductivity change induced in the Ga_2O_3 layers.

ε-Ga_2O_3 films of different thicknesses (in the range of 1200-100 nm) have been Ar-plasma treated and then electrically investigated. No significant thickness dependence was observed in terms of electrical properties (see Tab. 5.1), suggesting that the conductivity changes take place only close to surface of the layer.

The basic parameters of the most representative Ga_2O_3 samples are collected in Tab.5.1.

Tab.5.1 Electrical properties of the investigated Ga_2O_3 samples.

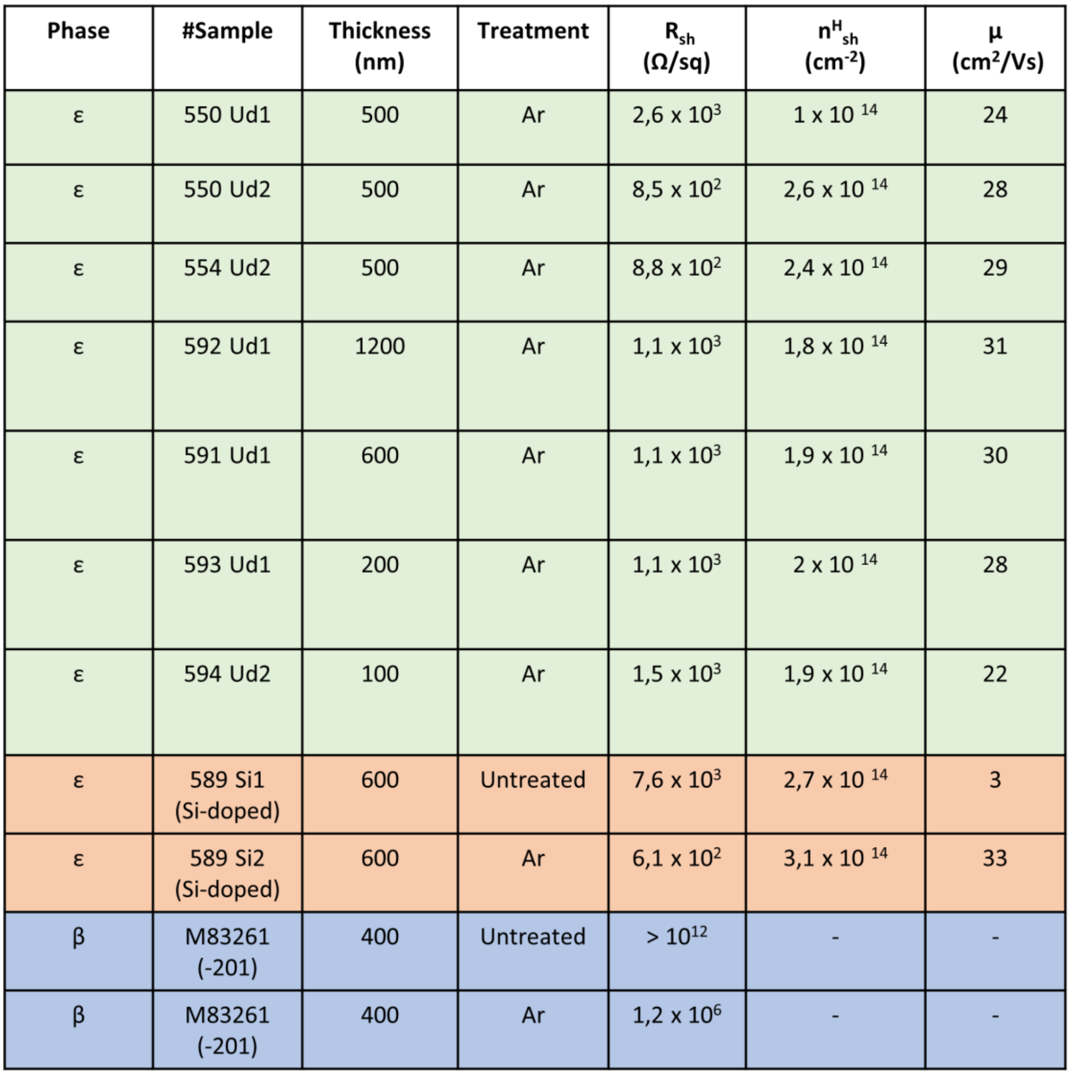

Phase	#Sample	Thickness (nm)	Treatment	R_{sh} (Ω/sq)	n^H_{sh} (cm^{-2})	μ (cm^2/Vs)
ε	550 Ud1	500	Ar	$2{,}6 \times 10^3$	1×10^{14}	24
ε	550 Ud2	500	Ar	$8{,}5 \times 10^2$	$2{,}6 \times 10^{14}$	28
ε	554 Ud2	500	Ar	$8{,}8 \times 10^2$	$2{,}4 \times 10^{14}$	29
ε	592 Ud1	1200	Ar	$1{,}1 \times 10^3$	$1{,}8 \times 10^{14}$	31
ε	591 Ud1	600	Ar	$1{,}1 \times 10^3$	$1{,}9 \times 10^{14}$	30
ε	593 Ud1	200	Ar	$1{,}1 \times 10^3$	2×10^{14}	28
ε	594 Ud2	100	Ar	$1{,}5 \times 10^3$	$1{,}9 \times 10^{14}$	22
ε	589 Si1 (Si-doped)	600	Untreated	$7{,}6 \times 10^3$	$2{,}7 \times 10^{14}$	3
ε	589 Si2 (Si-doped)	600	Ar	$6{,}1 \times 10^2$	$3{,}1 \times 10^{14}$	33
β	M83261 (-201)	400	Untreated	$> 10^{12}$	-	-
β	M83261 (-201)	400	Ar	$1{,}2 \times 10^6$	-	-

5.2.2 C-V measurements

The conductivity (σ) of a n-type semiconductor can be expressed as:

$$\sigma = en\mu \tag{5. 1}$$

where e is the electronic charge, n and μ are respectively the 3d carrier concentration and the mobility of electrons. Typically, the 3d carrier concentration (n) is determined by Hall effect measurements, considering the entire thickness of the sample, assuming that the carriers are uniformly distributed across the whole film thickness. However, this assumption is not valid in plasma treated samples, where the conductivity modification is limited to a slice thinner than the epilayer itself as demonstrated by the similar data collected on the series of different layer thicknesses.

A direct measurement of the 3d carrier concentration can be achieved by capacitance-voltage (C-V) measurements. C-V profiling were carried out on several Ar-plasma treated samples using a mercury-probe setup. In such a system mercury is brought into contact with the Ga_2O_3 layer forming two electrical contacts of different area, one acting as a Schottky gate electrode and the other operating as an ohmic contact.

The depletion width W of the Hg/Ga_2O_3 Schottky contact is related to the 3d carrier concentration *n* as follows:

$$W = \sqrt{\frac{2\varepsilon_0\varepsilon(V_R + V_{bi})}{en}} = \frac{\varepsilon_0\varepsilon A}{C} \tag{5. 2}$$

where ε_0 is the vacuum permittivity, ε is the relative dielectric constant, V_R is the reverse bias, V_{bi} is the built-in potential, e is the elementary charge, C is the Schottky barrier's capacitance and A is the area of the Schottky contact (7.3×10^{-8} m^2).

More information on the experimental setup and the C-V data analysis are reported in Chapter 2.

In the example of Fig.5.2a a carrier concentration of $1.2 \times 10^{20} cm^{-3}$ is obtained from the slope of the curve ($1/C^2$ vs V). Such high concentration values are typical in plasma-treated Ga_2O_3 samples and relevant profile across the surface layer is pretty uniform (Fig.5.2b).

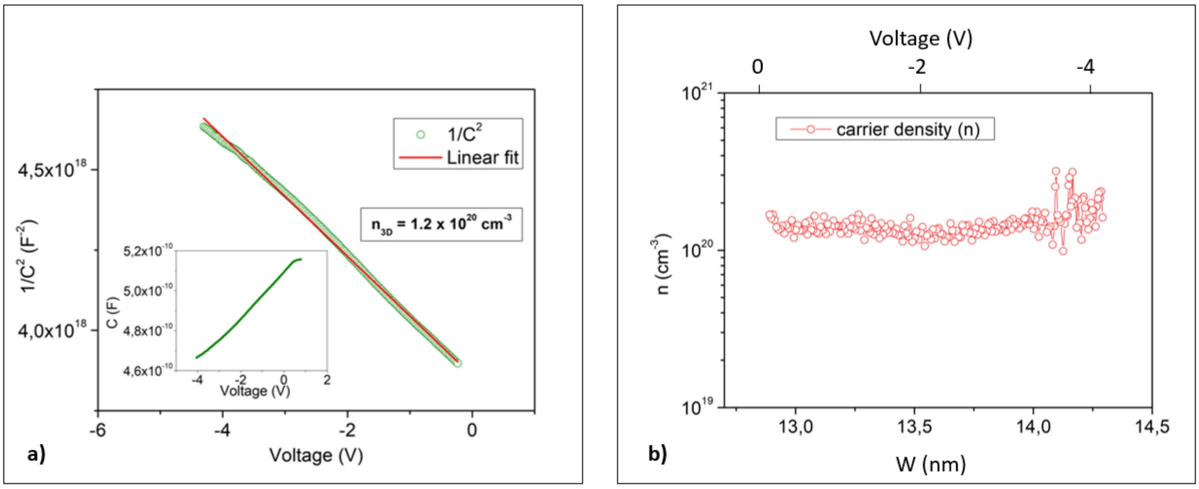

Fig.5.2 (a) Plot of $1/C^2$ vs. V and C-V curve (inset) for Ar-plasma treated sample (550 Ud2). (b) Carrier density profile as a function of extension of bias-dependent depletion width W into the semiconductor layer.

Basically, the thickness of the plasma-related conductive layer (d_c) can be defined as follows:

$$d_C = \frac{n_{sh}^{H}}{n_{3d}} \tag{5. 3}$$

where n_{sh}^{H} is the sheet carrier concentration measured by Hall measurements and n_{3d} is the 3d carrier concentration from the C-V measurements.

Considering a volume concentration of $1{,}2 \times 10^{20} cm^{-3}$ and a sheet carrier concentration of $2{,}6 \times 10^{14} cm^{-2}$ for Ar-plasma treated sample (550 Ud2), a thickness of about 20 nm is obtained for the plasma-modified layer, as reported in Tab.5.3.

A drawback of the C-V method is that it is limited to measuring the 3d carrier density near the surface region, without the possibility to investigate the carrier profile in the entire conductive layer. For example, in Ar-plasma treated samples the extension of depletion width is typically confined to 1-2 nm near the surface region, as shown in Fig.5.2b.

Additional information on the carrier concentration n can be collected via Seebeck coefficient measurements, as it will be described in the next section.

Moreover, the C-V measurements do not fully agree with the Eq. (5.2). In fact, considering $\varepsilon = 10$, $n = 1{,}2 \times 10^{20} cm^{-3}$, and a reasonable built-in voltage $V_{bi} = 1$ V, a depletion width W of about 3 nm at $V_R = 0\ V$ is obtained. Such a value is not consistent with respect to the experimental one (W ~ 13 nm) shown in Fig.5.2b. Alternatively, it can be observed that an unphysical value of V_{bi} justify a depletion of 13 nm at zero bias, supposing uniform the net doping density in the layer and equal to $n = 1{,}2 \times 10^{20} cm^{-3}$. This could be due to the formation of an additional HgO_x layer between the Hg contact and the Ga_2O_3 surface, which acts as a capacitance in series to that inside the Ga_2O_3, increasing the effective depletion region. However, this effect seems not affect the n value, which is instead in line with the Seebeck measurements (see sample 550Ud in Tab. 5.3).

5.2.3 Seebeck coefficient measurements

The Seebeck coefficient *S* is a relevant thermoelectric parameter, which provides significant information about a semiconductor material: the sign of *S* determines the type of the majority carriers ($S < 0$ for electrons, $S > 0$ for holes), while its magnitude is a function of the scattering mechanisms and the Fermi level, which in turn depends on the carrier effective mass m* and the 3d carrier concentration *n*.

In order to correlate the measured Seebeck coefficients of ε-Ga_2O_3 samples to the 3d electron concentration, the numerical model based on the Boltzmann transport equation (BTE) for In_2O_3 is used (Fig.5.3), which can be considered here as a model material for *S* vs. *n* behavior [6]. This qualitative approach is possible taking into account the similar physical properties of both In_2O_3 and ε-Ga_2O_3 materials, such as a similar effective electron mass m_n^* , and a comparable relative dielectric constant ε_r, which in turn involve similar scattering mechanisms within the material (see Tab.5.2).

Tab.5.2 Effective electron mass (m_n^*) with m_0 the standard rest electron mass and relative permittivity (ε_r) values for Ga_2O_3 and In_2O_3.

Material	m_n^* (m_0)	ε_r	Ref.
Ga_2O_3	(0.30 ± 0.02)	9.9 - 10.2	[7, 8]
In_2O_3	(0.30 ± 0.03)	9.0	[6, 9]

The blue line with open triangles reported in Fig.5.3 corresponds to the numerical solution of Boltzmann transport equation (BTE) for In_2O_3.

The following steps were performed in order to estimate the 3d carrier density and the related plasma-induced conductive layer for ε-Ga_2O_3 samples. First, the Seebeck coefficient (S) of an as-deposited Si-doped ε-Ga_2O_3 sample, represented by a green star in the graph, was acquired. In this case, being the film conduction related to intentional doping supposed to be homogeneous throughout the entire layer thickness, the 3d carrier concentration (n_{3D}^H) was determined by Hall measurements, i.e. “bulk” conduction. As it is clearly visible in Fig.5.3 a good correlation with the In_2O_3 curve is obtained.

Successively, the Seebeck coefficients of Ar-plasma treated samples (red stars) were determined and plotted along the In_2O_3 calibration curve in order to estimate the 3d charge carrier density.

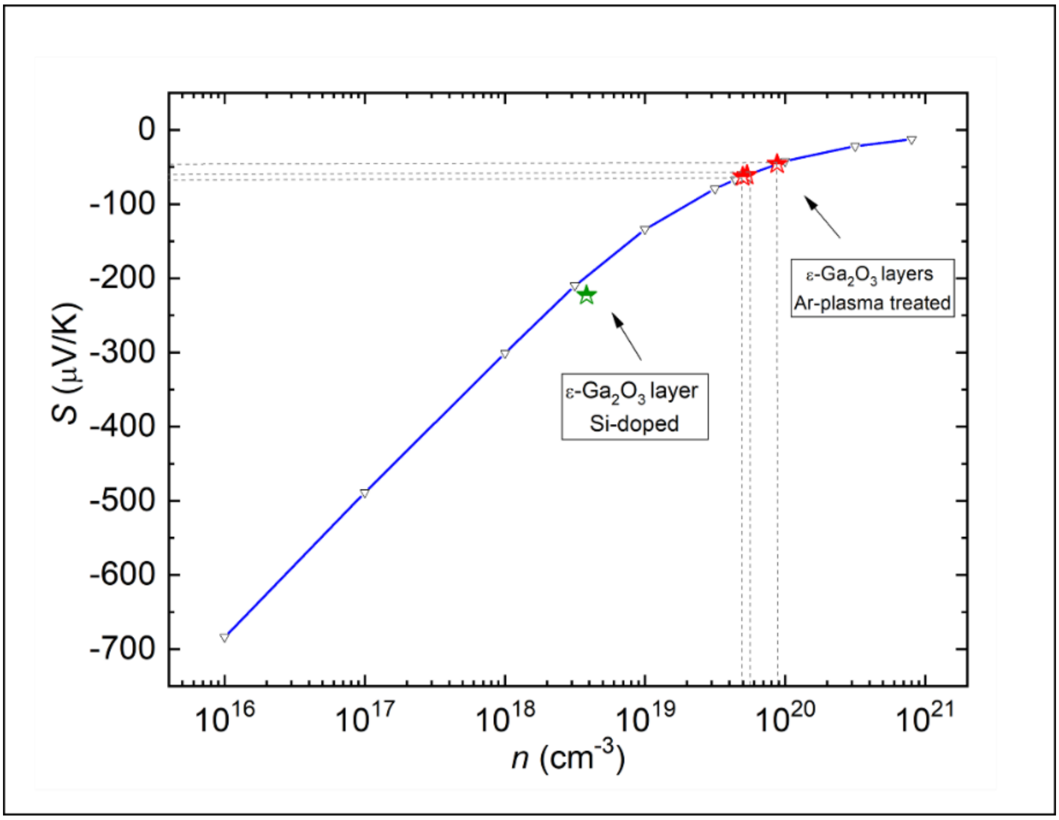

Fig.5.3 Seebeck coefficient (S) as a function of 3d carrier concentration (n). Green star represents the experimental value refers to the Si-doped layer, while red stars represent Seebeck coefficients of Ar-plasma treated ε-Ga_2O_3 layers. The blue line with open triangles corresponds to the numerical solution of BTE equation for In_2O_3 [6].

By using Eq. (5.3) and considering the 3d carrier concentrations from the Seebeck measurements of Ar-plasma treated layers, a thickness of the plasma-modified surface layer d_c in the 20-30 nm range is obtained (see Tab. 3), which is in line with preliminary C-V measurements.

Tab.5.3 Electrical properties of the investigated ε-Ga_2O_3 samples. n_{sh}^{H} is measured by the van der Pauw method and n_{3d}^{H} is the corresponding 3d carrier concentration assuming homogeneous carrier distribution in the entire thickness of the layer. S is the experimental Seebeck coefficient, n_{3d}^{S} is the volume carrier density derived from S using In_2O_3 calibration curve (Fig.5.3), and d_C is the thickness of the conductive layer calculated by using Eq. (5.3). For comparison the 3d carrier concentration calculated by C-V measurement (n_{3d}^{CV}) is reported with the related conductive layer thickness (sample 550 Ud2).

#Sample	Treatment	S $(\mu W/K)$	n_{sh}^{H} (cm^{-2})	n_{3d}^{H} (cm^{-3})	$n_{3d}^{S}(n_{3d}^{CV})$ (cm^{-3})	d_C (nm)
565 Si	Untreated	- 223	2.4×10^{14}	3.6×10^{18}	-	-
550 Ud1	Ar	-63	1.0×10^{14}	-	4.9×10^{19}	20
550 Ud2	Ar	-46	2.6×10^{14}	-	8.7×10^{19} (1.2×10^{20})	29 (21)
550 A1	Ar	-61	1.3×10^{14}	-	5.3×10^{19}	24

5.3 Time stability of the plasma-induced conductivity

Time stability of the Ar plasma-induced conductivity was monitored in selected ε-Ga_2O_3 samples by monitoring R_{sh}, n_{sh}, and μ on a time scale of about 4 months (see Fig.5.4). Over this period the electrical parameters remained approximately the same, suggesting that the Ar-plasma treatment induces a permanent conductivity enhancement in the layer.

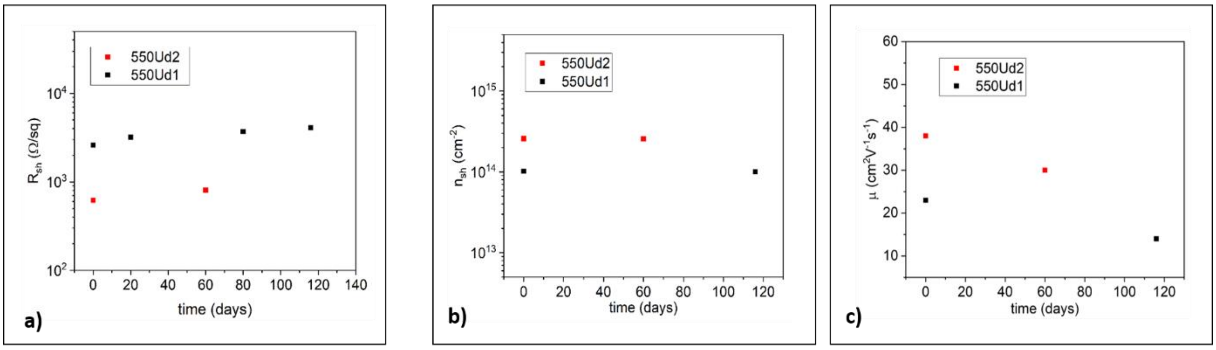

Fig.5.4 R_{sh} (a), n_{sh} (b) and μ (c) of Ar-plasma treated ε-Ga_2O_3 samples repeatedly measured during four months.

5.4 Effect of temperature on the plasma-induced conductivity

Rapid thermal annealing (RTA) processes in controlled atmosphere were performed in order to investigate the effect of thermal treatment on the Ar-plasma treated samples. In particular, ε-Ga_2O_3 samples were subsequently annealed at 100 °C, 200 °C, and 300 °C in different atmospheres i.e., oxygen (O_2) and forming gas (N_2/H_2 – 20% hydrogen). Hall measurements were carried out before and after each treatment. It was observed that the thermal treatment at 100 °C for 10 minutes has very limited effect on the electrical properties of the layer, while an additional thermal annealing at 200 °C for 10 minutes is effective in decreasing the conductivity, the carrier concentration and the mobility (see Fig.5.5). A further annealing treatment at 300°C for 1 minute makes the film insulating, i.e. not measurable R_{sh}. The thermal effect is comparable in O_2 and N_2/H_2 atmosphere. This suggests that (i) the conducting layer induced by the plasma treatment is stable just in a narrow temperature window ($T < 200$ °C) and (ii) the background atmosphere (oxidizing or reducing, i.e. O_2 or forming gas respectively) is not remarkably affecting this thermally activated process.

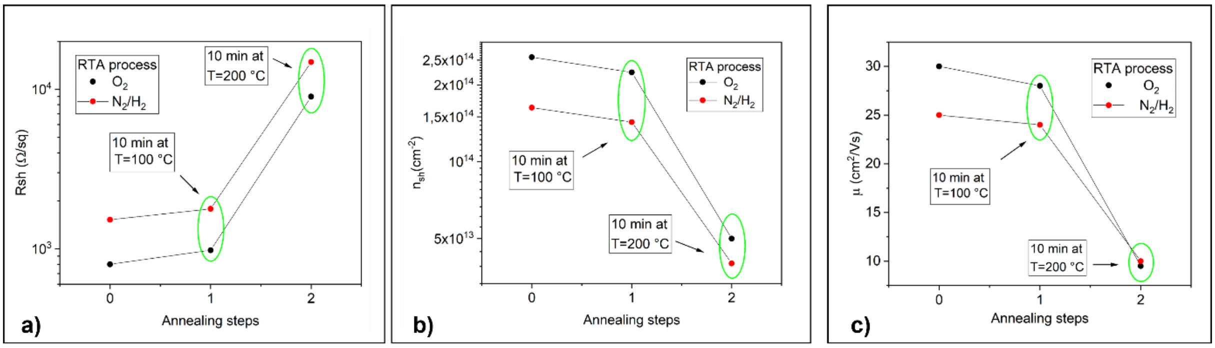

Fig.5.5 R_{sh} (a), n_{sh} (b) and μ (c) of Ar-plasma treated ε-Ga_2O_3 samples vs. thermal annealing processes in different atmosphere (O_2 and N_2/H_2). In the horizontal axis: “0” indicates no-annealing treatment, “1” corresponds to the annealing treatment for 10 minutes at 100 °C and “2” indicates a subsequent annealing for 10 minutes at 200 °C.

5.5 Surface morphology effect of the plasma treatment

The surface morphology of ε-Ga_2O_3 layers was investigated by means of Atomic Force Microscopy (AFM) before and after the plasma exposures. The heteroepitaxial layers show a mean surface roughness (R_{ms}) of about 2 nm and no significant differences were observed before and after treatment (Fig.5.6).

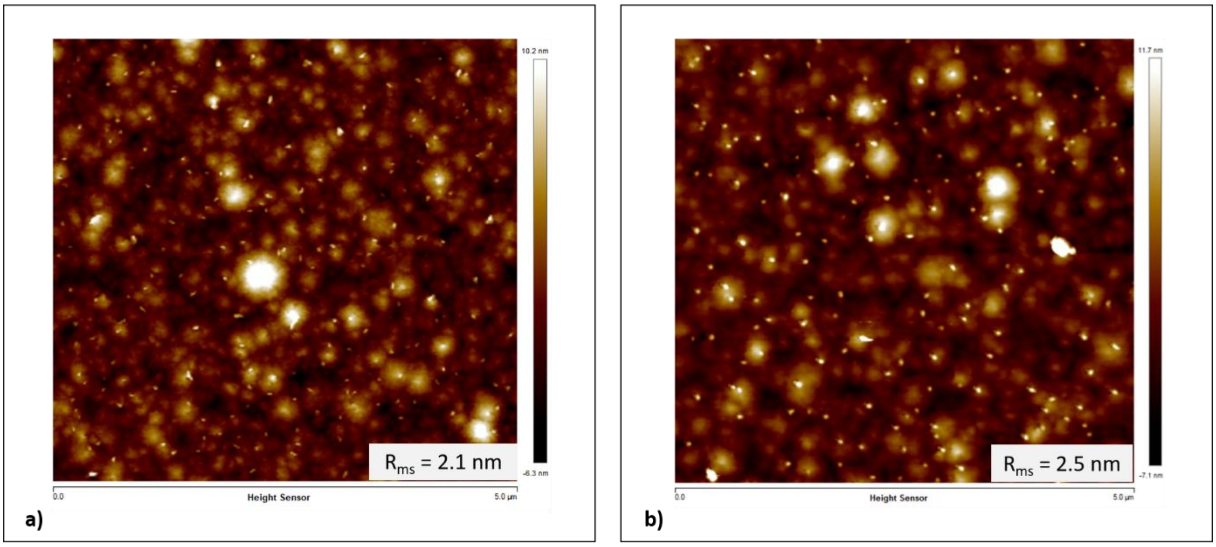

Fig.5.6 AFM images of ε-Ga_2O_3 sample before (a) and after (b) the plasma exposure. R_{ms} indicates the root mean square roughness of the surface.

5.6 Possible role of persistent photoconductivity (PPC)

In order to exclude a possible persistent photoconductivity (PPC) effect induced by the UV components generated by the plasma, a ε-Ga_2O_3 film was overgrown with a SiO_x wide bandgap layer (80 nm thick). In principle, SiO_x should act as a protective mask for the ε-Ga_2O_3 surface, hence preventing the direct plasma exposure. However, a significant part of the UV plasma light can still reach the ε-Ga_2O_3 surface, thanks to the optical transparency of the SiO_x in this range (band gap $E_G \sim 7\ eV$). After the plasma treatment the ε-Ga_2O_3 layer was electrically investigated and no significant change in conductivity was detected, which excludes any PPC effects and implies that the surface conductivity conversion is strictly related to plasma exposure.

5.7 Conclusive remarks and outlooks

While it is clear and confirmed that the Ar-plasma treatment induces a remarkable sheet conductivity, the physical mechanism behind such drastic conductivity change is not understood. We suspect that the higher conductivity could be related to a partial amorphization of a thin Ga_2O_3 layer in the vicinity of the surface.

The full explanation of the physical mechanism induced by the plasma treatment requires further experimental investigations such as X-Ray Photoelectron Spectroscopy (XPS) and transmission electron microscopy (TEM), already planned to be performed in order to investigate the physical/chemical composition and the crystal structure of the conductive layer.

References

[1] H. Akazawa, “Argon plasma treatment of transparent conductive ZnO films.,” *Applied Physics Express*, vol. 2, no. 8, p. 081601, 2009.

[2] O. Bierwagen, J. S. Speck, T. Nagata, T. Chikyow, Y. Yamashita, H. Yoshikawa and K. Kobayashi, “Depletion of the In2O3 (001) and (111) surface electron accumulation by an oxygen plasma surface treatment,” *Applied Physics Letters*, vol. 98, no. 17, p. 172, 2011.

[3] I. Lapsanska, “Plasma-induced conductivity in MBE-grown thin films of gallium oxide,” *Master thesis, University of Strathclyde - Paul Drude Institute.*

[4] A. Fiedler, R. Schewski, M. Baldini, Z. Galazka, G. Wagner, M. Albrecht and K. Irmscher, “Influence of incoherent twin boundaries on the electrical properties of β-Ga2O3 layers homoepitaxially grown by metal-organic vapor phase epitaxy,” *Journal of Applied Physics* , vol. 122, no. 16, p. 165701, 2017.

[5] R. Schewski, G. Wagner, M. Baldini, D. Gogova, Z. Galazka, Schulz, T. Remmele, T. Markut, H. von Wenckstern, M. Grundmann, O. Bierwagen, P. Vogt and M. Albrecht, “Epitaxial stabilization of pseudomorphic α-Ga2O3 on sapphire (0001),” *Applied Physics Express,* vol. 8, no. 1, p. 011101, 2014.

[6] N. Preissler, O. Bierwagen, A. T. Ramu and J. S. Speck, “Electrical transport, electrothermal transport, and effective electron mass in single-crystalline In2O3 films,” *Physical Review B,* vol. 88, no. 8, p. 085305, 2013.

[7] H. J. Von Bardeleben, J. L. Cantin, A. Parisini, A. Bosio and R. Fornari, “Conduction mechanism and shallow donor properties in silicon-doped ε-Ga2O3 thin films: An electron paramagnetic resonance study.,” *Physical Review Materials,* vol. 3, no. 8, p. 0846, 2019.

[8] M. Passlack, E. F. Schubert, W. S. H. M. Hobson, N. Moriya, S. N. G. Chu, K. Konstadinis, J. Mannaerts, M. Shnoes e G. J. Zydzik, «Ga2O3 films for electronic and optoelectronic applications,» *Journal of applied physics,* vol. 77, n. 2, pp. 686-693, 1995.

[9] I. Hamberg and C. G. Granqvist, “ Evaporated Sn-doped In2O3 films: Basic optical properties and applications to energy-efficient windows,” *Journal of Applied Physics,* vol. 60, no. 11, pp. R123-R160, 1986.

Conclusions

This PhD thesis was directed to investigate and clarify some open questions concerning the physical properties of gallium oxide (Ga_2O_3) epilayers. This material has indeed gained increasing interest for applications in high-power electronics and solar-blind deep-UV photodetectors, because of its exceptional physical properties such as wide bandgap, high breakdown field and good optical transparency. There are however many open questions which deserve to be investigated more in depth, in particular, regarding electrical and photoelectrical properties of the metastable ε-Ga_2O_3 polymorph.

The first part of the experimental activity concerned the fabrication of reliable electrical contacts and the achievement of n-type doping of ε-Ga_2O_3 layers by Sn thermal diffusion. Another important task concerned the development of UV-C solar-blind photodetectors based on ε-Ga_2O_3. The last experimental task accomplished during this PhD thesis dealt with the investigation of the effects of plasma treatments on ε-Ga_2O_3 epilayers.

The main achieved results can be summarized as follows:

A method for n-type doping of ε-Ga_2O_3 epilayers via Sn thermal diffusion was developed. It includes the deposition of a tin rich SnO_x film (50 nm thick) on top of ε-Ga_2O_3 layer and the subsequent annealing at 600°C for 4 hours in vacuum to allow Sn diffusion in the underlying ε-Ga_2O_3 layer. The stoichiometry of the SnO_x plays a key role for the Sn diffusion into the ε-Ga_2O_3 layer. It was indeed observed that only by depositing a tin-rich film $SnO_{(2-x)}$ with $x<<1$ it was possible to obtain an effective diffusion of Sn atoms into the ε-Ga_2O_3 layer, and consequently an effective n-type doping. The Sn-diffusion into the ε-Ga_2O_3 has been confirmed by different characterization techniques, such as ToF-SIMS, Raman and RBS.

SnO_x deposition process used to obtain n-type doping of ε-Ga_2O_3 films by Sn diffusion has then been exploited as an effective method to fabricate good Ohmic contacts on ε-Ga_2O_3 layers, which is a remarkable technological achievement. Ohmic contacts were obtained by depositing SnO_x/ITO bilayers on top of undoped and Sn-doped ε-Ga_2O_3 layers. Electrical characterization has then been performed using TLM method, which permits to determine the specific contact resistance (ρ_c), a crucial parameter to define the performance of Ohmic contact. TLM analysis carried out on Sn-doped ε-Ga_2O_3 samples shows that the specific contact resistance is about $\rho_c = (2 \div 3) \cdot 10^{-3}\ \Omega cm^2$, which can be considered as the state of the art for the ε-polymorph.

Hall measurements as a function of temperature, in vacuum and dark conditions, have been performed on the Sn-doped ε-Ga_2O_3 layers to investigate their electrical properties. The electrical characterization shows that the electronic transport takes place via hopping conduction, according to the Mott law. For the first time, RT resistivity of the order of 1 Ωcm and a donor concentration above 10^{18} cm^{-3} were successfully achieved by Sn diffusion.

Another important part of the PhD activity includes the fabrication of UV-C solar-blind photodetector (PD). This was made in order to exploit the unique properties of ε-Ga_2O_3 films, such as intrinsic spectral selectivity in the UV-C spectral region.

PD test structures consisted of highly resistive intrinsic ε-Ga_2O_3 films ($\rho \approx 10^8$ Ωcm) grown by MOCVD on c-oriented Al_2O_3 substrates, with a pattern of electrodes (SnO_x+ITO bilayers) fabricated by sputtering deposition.

Test devices showed promising results such as high responsivity, solar-blind rejection ratio (R_{UV-SUN}) greater than 10^4 and good ON-OFF photoresponse, which makes the epsilon phase of gallium oxide an excellent material for UV-C detection.

While studying the photodetectors' performance, it appeared that they exhibit high values of photo-gain. This phenomenon was carefully investigated and finally ascribed to the excess of collected majority carriers (electrons), with respect to the minority carriers (holes), possibly related to hole trapping/self-trapping processes in the photoconductive channel.

The ε-Ga_2O_3 films for light detection must be very resistive, therefore the macroscopic distance between the contacts becomes a critical parameter as it requires high applied voltages between electrodes. Therefore, the implementation of interdigitated contacts (with the distance between the contacts < 0,05 mm) is an interesting perspective. This type of contacts was just implemented at the end of the thesis period and is expected to bring some advantages: (i) an increase of the photocurrent signal due to the optimization of the photogenerated carrier collection, (ii) a faster ON-OFF photoresponse, with the possibility to operate at lower voltages.

The last experimental activity dealt with the investigation of plasma treatments on ε-Ga_2O_3 and β-Ga_2O_3 epilayers grown on c-oriented sapphire substrates by MOCVD and MBE, respectively. Such a process induced – depending on the material and the treated surface – physical and/or chemical changes which in turn resulted in a detectable variation of the surface conductivity. Undoped ε-Ga_2O_3 grown by MOVPE, exhibits a very high intrinsic resistivity, and with the present work it was demonstrated that the plasma treatment represents a new approach to modulate its surface electrical properties.

The ε-Ga_2O_3 layers have been electrically investigated by Hall measurements before and after plasma exposures. It has been found that the Ar-plasma treatment induced a considerable increase of the conductivity of the layer (for both doped and undoped layers), with respect to the untreated ones. In particular, the nominally undoped ε-Ga_2O_3 layers after the Ar-plasma treatment showed a sheet resistance (R_{sh}) of about $10^3 \Omega/sq$ (i.e much lower than in as-grown epilayers, $R_{sh} > 10^{12} \Omega/sq$) and sheet Hall carrier concentration ($n_{sh}^H \sim 10^{14} cm^{-2}$) and mobility ($\mu = 20 - 30 cm^2/Vs$).

This investigation was also performed on nominally undoped β-Ga_2O_3 (-201) heteroepitaxial layers deposited by MBE on c-plane sapphire substrates. Interestingly, the effect of the plasma treatment was qualitatively the same as for the ε-Ga_2O_3 layers, i.e. resulting in a decrease in the R_{sh} with respect to untreated layers. However, β-Ga_2O_3 layers showed a higher sheet resistance ($R_{sh} \sim 10^6 \Omega/sq$) compared to the ε-$Ga_2O_3$ samples ($R_{sh} \sim 10^3 \Omega/sq$), although with comparable layer thicknesses. The different R_{sh} of β and e epilayers could be related to the different structural defects in the two structures, for example to the presence of electrically charged twin domains in β-Ga_2O_3 (-201) layers.

In order to estimate the thickness of the Ar plasma-modified sheet and understand the physical reason behind the conductivity change induced in the ε-Ga_2O_3 layers, ε-Ga_2O_3 films of different thicknesses (in the range of 1200-100 nm) have been Ar-plasma treated and then electrically investigated. No significant thickness dependence of electrical properties was observed in terms, suggesting that the conductivity changes take place only in the uppermost part of the layer. An about 20-30 nm thick conductive layer was estimated by a combination of the Seebeck coefficient and Hall effect measurements.

The Ar-plasma induced conductivity was monitored in selected ε-Ga_2O_3 samples over the time. After about 4 months the electrical parameters (R_{sh}, n_{sh}, μ) remained approximately the same, suggesting that the Ar-plasma treatment induces a permanent conductivity enhancement in the layer. However, it was observed that such sheet conductivity disappears with thermal treatments at $T > 200$ °C in different atmospheres i.e., oxygen (O_2) and forming gas (N_2/H_2).

While it is clear and confirmed that the Ar-plasma treatment induces a remarkable sheet conductivity, the physical mechanism behind such drastic conductivity change is not understood. We suspect that the higher conductivity could be related to a partial amorphization of the Ga_2O_3 layer in the vicinity of the surface.

The full explanation of the physical mechanism induced by the plasma treatment requires further experimental investigations such as X-Ray Photoelectron Spectroscopy (XPS) and transmission electron microscopy (TEM). These measurements are already planned and should be performed at the earliest in order to get structural and physico-chemical insights from the conductive surface layer.

Appendix A – Publications

- Bosio, A., Borelli C., Parisini A., Pavesi M., Vantaggio, S., Fornari, R.,
  “A Metal-Oxide Contact to ε-Ga_2O_3 Epitaxial Films and Relevant Conduction Mechanism” ECS Journal of Solid StateScience and Technology, vol. 9, p. 055002, 2020.

- Bosio, A., Parisini, A., Lamperti, A., Borelli, C., Fornasini, L., Bosi, M., Cora, I., Fogarassy, Z., Pécz, B., Zolnai, Z; Németh A., Vantaggio, S., Fornari, R.,
  “n-Type doping of ε-Ga_2O_3 epilayers by high-temperature tin diffusion” Acta Materialia, vol. 210, p. 116848, 2021.

- Borelli, C., Bosio, A., Parisini, A., Pavesi, M., Vantaggio, S., Fornari, R.,
  “Electronic properties and photo-gain of UV-C photodetectors fabricated from high-resistivity Ga_2O_3 epilayers” (submitted).

Appendix B – Conference contributions and awards

- ICCPMS 2019 – International Conference on Chemical Physics and Material Science *"Shallow and deep energy levels in ε-Ga_2O_3 epilayers grown on (0001) sapphire",* A. Parisini, M.Bosi, A. Bosio, H.J von Bardeleben, M. Mulazzi, V. Fiorentini, M. Pavesi, A.Baraldi, V. Montedoro, C. Borelli, S. Vantaggio and R. Fornari, Istanbul, Turkey. (Poster)

- ICCGE 2019 - International Conference on Crystal Growth and Epitaxy - *"Silicon and Tin doping of ε-Ga_2O_3 epilayers grown by MOVPE",* R. Fornari, A. Bosio, M. Bosi, A. Parisini, Z. Zolnai, A. Lamperti, V. Montedoro, C. Borelli, M. Pavesi - Keystone, Colorado, United States. (Poster)

- ICOP 2020 - Italian Conference on Optics and Photonics - *"Reliability of UV solar-blind photodetectors based on ε-Ga_2O_3",* C. Borelli, A. Baraldi, M. Bosi, V. Montedoro, A. Parisini, M. Pavesi, L. Seravalli, S. Vantaggio and R. Fornari, virtual conference. (Poster)

- CSW 2021 - Compound Semiconductor Week - *"High quality ε-Ga_2O_3 thin films for UV solar-blind detection",* C. Borelli, A. Baraldi, M. Bosi, V. Montedoro, A. Parisini, M. Pavesi, L. Seravalli, S. Vantaggio, A. Torres, S. Dadgostar, J. Jimenez and R. Fornari, virtual conference. (Oral presentation)

- June 2020 - Winner of S3 PhD video contest promoted by ART-ER (Consortium company for the sustainable growth and attractiveness of Emilia-Romagna).
  The aim of the contest was to enhance and disseminate the research work of the PhD students carried out in the Universities of Emilia-Romagna.
  Topic: “Solar-blind UV-C photodetectors based on ε -Ga_2O_3 epilayers”.

- September 2021 - Winner of German Academic Exchange Service (DAAD) scholarship for a two-month research period abroad as a guest PhD student at the Paul Drude Institute of Berlin (PDI).

Acknowledgements

First of all I would like to express my sincere gratitude to my supervisor Prof. Roberto Fornari for his invaluable advice and continuous support during my PhD study.

I would like to offer my special thanks to Prof. Antonella Parisini and Prof. Alessio Bosio for their continuous support throughout the last three years.

I wish to extend my special thanks to the other members of the research group: Prof. Maura Pavesi, Prof. Andrea Baraldi, and Sig. Salvatore Vantaggio for the constructive discussions on the electrical and optical characterization of the investigated Ga_2O_3 *samples.*

Many thanks to Dr. Matteo Bosi and Dr. Luca Seravalli of IMEM-CNR Institute for providing the Ga_2O_3 *samples utilized in this work.*

My sincere thanks go to Dr. Oliver Bierwagen and Dr. Piero Mazzolini who provided me an opportunity to join their team as a guest PhD student at the Paul-Drude Institute of Berlin. This research period represented an important chance to extend my knowledge in the field of semiconductor physics and technology.

I wish to thank the coordinator of PhD course, Prof. Stefano Carretta, for his support and constant availability.

Last but not the least, I would like to give special thanks to my family and friends for their support and for believing in me during all this period.

Thank you so much!

Carmine